Karlsruhe Institute of Technology

Doppler Lidar Volume Flux Observations in a Broad Alpine Valley

Master's Thesis by

Sarah Paratoni

At the KIT Department of Physics
Institute for Meteorology and Climate Research
Troposphere Research (IMKTRO)

Advisor:	Prof. Dr. Peter Knippertz
Co-advisor:	Assoc. Prof. Dr. Alexander Gohm (University of Innsbruck)
Supervisor:	Dr. Philipp Gasch

January – December 2025

Karlsruhe Institute of Technology
Department of Physics
76131 Karlsruhe
Germany

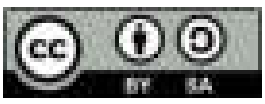

Doppler Lidar Volume Flux Observations in a Broad Alpine Valley (Master's Thesis)

Ich versichere wahrheitsgemäß, die Arbeit selbständig verfasst, alle benutzten Quellen und Hilfsmittel vollständig und genau angegeben und alles kenntlich gemacht zu haben, was aus Arbeiten anderer unverändert oder mit Abänderungen entnommen wurde sowie die Satzung des KIT zur Sicherung guter wissenschaftlicher Praxis in der jeweils gültigen Fassung beachtet zu haben.

Karlsruhe, December 2025

. . . . . .

(Sarah Paratoni)

Abstract

Understanding valley flows and transport processes in Alpine valleys is essential to characterizing thermally driven circulations. However, direct observations of these processes remain difficult. The establishment of a valley volume flux (VVF) budget can provide a direct measurement of the horizontal transport through a valley section and an indirect measurement of the vertical movement through the upper boundary of the section. This thesis evaluates the feasibility of deriving the VVF in the broad Inn Valley using Doppler wind lidar (DWL) measurements. A six-week ground-based DWL deployment in September and October 2024 was combined with targeted airborne DWL transects and large-eddy simulations (LESs) to test, refine, and validate existing VVF estimation approaches originally developed for narrower valleys.

When estimating VVF from a single wind profile, a weighting factor is needed. A central challenge is the determination of an appropriate value that accounts for the non-homogeneity of the along-valley wind component in cross-valley direction. Previous methods, which assume maximum wind speeds at the valley center, proved unsuitable for the curved and heterogeneous Inn Valley. This study introduces a simplified and more flexible weighting factor estimation based on shallow plane position indicator (PPI) sector scans, enabling application to asymmetric cross-sections and allowing the use of all sub-daily scans to capture temporal variability. The VVF is calculated for three cross-sections along the valley and interpreted within a control-volume framework. Four case-study days are analyzed in detail, representing valley-wind conditions influenced initially by easterly flow and later by foehn. While nighttime down-valley flow regularly exhibits VVF divergence, likely driven by tributary outflow and foehn effects, no systematic daytime VVF divergence is found during up-valley flow, consistent with theoretical expectations.

Four airborne DWL transects provide direct cross-sections of along-valley flow and closely match the ground-based VVF estimates, agreeing within 2–16%. Numerical simulations with the ICOsahedral Nonhydrostatic (ICON) model in LES mode reproduce key structural and temporal characteristics of valley winds but overestimate up-valley wind strength and thus VVF magnitude. Limitations of the analysis arise from assumptions regarding tributary fluxes, and the use of a single, time-invariant weighting factor. The presence of synoptic disturbances during the case study period makes interpreting the observed phenomena more challenging. However, the analysis shows that weak valley winds still develop close to the surface, even under suboptimal conditions.

This work prepared VVF retrieval methodologies to be applied to data from the TEAMx observational campaign (TOC) that took place in the summer of 2025. The methods and insights developed here informed the measurement strategy for the TOC, including improved lidar alignment and scanning protocols. Overall, this thesis demonstrates that a refined DWL-based VVF estimation is feasible in a broad and complex valley and highlights path-

ways for further improvement, particularly through time- and space-dependent weighting factors.

Zusammenfassung

Das Verständnis von Talströmungen und Transportprozessen in alpinen Tälern ist entscheidend für die Charakterisierung thermisch angetriebener Zirkulationen. Direkte Beobachtungen dieser Prozesse bleiben jedoch schwierig. Die Erstellung eines Talvolumenflussbudgets kann eine direkte Messung des horizontalen Transports durch einen Talbaschnitt sowie eine indirekte Messung der vertikalen Bewegung durch die obere Begrenzung des Abschnitts liefern. Diese Arbeit bewertet die Machbarkeit der Ableitung des Talvolumenflusses im breiten Inntal mithilfe von Doppler-Wind-Lidar-Messungen. Eine sechswöchige bodengebundene Doppler-Wind-Lidar-Messkampagne im September und Oktober 2024 wurde mit gezielten luftgestützten Doppler-Wind-Lidar-Querprofilen und Large-Eddy Simulationen kombiniert, um bestehende Ansätze zur Schätzung des Talvolumenflusses, die ursprünglich für schmalere Täler entwickelt wurden, zu testen, zu verfeinern und zu validieren.

Bei der Schätzung des Talvolumenflusses aus einem einzelnen Windprofil ist ein Gewichtungsfaktor erforderlich. Eine zentrale Herausforderung besteht in der Bestimmung eines geeigneten Wertes, der die Inhomogenität der talachsparallelen Windkomponente in Querrichtung des Tals berücksichtigt. Frühere Methoden, die maximale Windgeschwindigkeiten im Talzentrum annehmen, erwiesen sich für das gekrümmte und heterogene Inntal als ungeeignet. Diese Studie führt eine vereinfachte und flexiblere Bestimmung des Gewichtungsfaktors auf der Grundlage flacher planparalleler Sektorscans ein, die eine Anwendung auf asymmetrische Querschnitte ermöglicht und die Nutzung aller untertägigen Scans erlaubt, um zeitliche Variabilität zu erfassen. Der Talvolumenfluss wird für drei Talquerschnitte berechnet und im Rahmen eines Kontrollvolumenansatzes interpretiert. Vier Fallstudientage werden detailliert analysiert und repräsentieren Talwindbedingungen, die zunächst durch östliche Strömung und später durch Föhneinfluss geprägt sind. Während der nächtliche talauswärts gerichtete Wind regelmäßig eine Divergenz des Talvolumenflusses zeigt, vermutlich verursacht durch Zufluss aus Seitentälern und Föhneffekte, wird während der tagsüber auftretenden taleinwärts gerichteten Strömung keine systematische Divergenz des Talvolumenflusses gefunden, was mit theoretischen Erwartungen übereinstimmt.

Vier luftgestützte Doppler-Wind-Lidar-Querprofile liefern direkte Querschnitte der talachsparallelen Strömung und stimmen eng mit den bodengebundenen Schätzungen des Talvolumenflusses überein, mit Abweichungen von 2 bis 16 Prozent. Numerische Simulationen mit dem ICON-Modell im Large-Eddy-Modus reproduzieren wesentliche strukturelle und zeitliche Eigenschaften der Talwinde, überschätzen jedoch die Stärke der taleinwärts gerichteten Strömung und damit die Größe des Talvolumenflusses. Einschränkungen der Analyse ergeben sich aus Annahmen zu Flüssen aus Seitentälern sowie aus der Verwendung eines einzelnen, zeitlich invarianten Gewichtungsfaktors. Das Auftreten synoptischer Störungen während des Zeitraums der Fallstudien erschwert zudem die Interpretation der beobachteten Phänomene. Dennoch zeigt die Analyse, dass sich auch unter suboptimalen Bedingungen schwache Talwinde bodennah entwickeln.

Diese Arbeit bereitete Methoden zur Ableitung des Talvolumenflusses vor, die auf Daten der im Sommer 2025 durchgeführten TEAMx-Messkampagne angewendet werden sollen. Die hier entwickelten Methoden und Erkenntnisse flossen in die Messstrategie dieser Kampagne ein, einschließlich verbesserter Ausrichtung der Lidarsysteme und optimierter Scanprotokolle. Insgesamt zeigt diese Arbeit, dass eine verfeinerte, auf Doppler-Wind-Lidar basierende Schätzung des Talvolumenflusses in einem breiten und komplexen Tal möglich ist, und hebt Ansatzpunkte für weitere Verbesserungen hervor, insbesondere durch zeit- und ortsabhängige Gewichtungsfaktoren.

Contents

Abbreviations

ABL	atmospheric boundary layer
AGL	above ground level
AIRflows	**AIR**borne **f**ixed-beam **l**idar f**o**r **w**ind measurement**s**
ASL	above sea level
AtmoProKIT	Atmospheric Profile Processing toolKIT
AVF	above valley floor
CNR	carrier-to-noise ratio
DWL	Doppler wind lidar
ECMWF	European Centre for Medium-Range Weather Forecasts
ERA-interim	ECMWF Reanalysis - Interim
ERA5	ECMWF Reanalysis v5
FFT	fast-fourier transform
i-Box	Innsbruck Box
ICON	ICOsahedral Nonhydrostatic
IOP	intense observation period
LES	large-eddy simulation
LIVAVERT(EX)^2	**Li**nking **va**lley flow and **vert**ical **ex**change in compl**ex** terrain
MoBL	mountain boundary layer
PPI	plane position indicator
RHI	range height indicator
TEAMx	Multi-scale **t**ransport and **e**xchange processes in the **a**tmosphere over **m**ountains – programme and e**x**periment
TOC	TEAMx observational campaign
VVF	valley volume flux

1. Introduction

1.1. Motivation

The atmospheric boundary layer (ABL) in mountainous terrain, also known as mountain boundary layer (MoBL; Lehner and Rotach, 2018), presents a high degree of complexity compared to flat terrain due to the interplay between the orography and the atmosphere. Unlike over flat terrain, where ABL dynamics can often be approximated as horizontally homogeneous, mountainous regions feature steep slopes and heterogeneous land-surface characteristics that, through differential heating and cooling over the diurnal cycle, drive pronounced thermally induced circulations (e.g., Whiteman, 2000; Zardi and Whiteman, 2013). Valley winds are a characteristic feature of mountainous areas, arising from differential heating and cooling between both the valley and the adjacent planes and the valley floor and the surrounding slopes. During the day, stronger heating within the valley drives up-valley flows, and stronger heating of the slopes drives up-slope flow, while nocturnal cooling causes down-valley and down-slope flows (Whiteman, 2000). The superposition of dynamically driven processes (mountain waves, foehn winds) and thermally driven processes (slope and valley winds) creates the spatio-temporal variability observed in MoBLs. This variability manifests at scales ranging from individual slope flows to valley wind systems and regional mountain-plain circulations, all interacting simultaneously.

Vertical exchange processes play a crucial role in the MoBL; up-slope winds, valley winds, and turbulent transport govern the exchange of momentum, heat, moisture, and trace gases between the valley atmosphere and the free troposphere due to convective mixing and dynamical forcing (Rotach et al., 2015; Serafin et al., 2018). Understanding vertical exchange is therefore essential for improving numerical weather prediction and for accurately representing atmospheric processes in mountainous regions. A method to characterize and quantify vertical exchange is through the estimation of a flux budget derived from valley volume fluxes (VVFes). The VVF method quantifies the inflow and outflow of air volumes (masses) through a cross-section. When performed at multiple locations along the valley, a flux budget can be established. A control volume is defined and the VVF is computed at the edges of the volume. One can compute the difference between the along-valley inflow into the control volume and the outflow from the control volume. Assuming the absence of inflows or outflows from tributaries, it can be deduced that the observed difference is the result of vertical motion in the valley segment. This approach offers valuable insights into how the exchange between the valley atmosphere and the free troposphere evolves throughout the diurnal cycle.

The computation of the VVF requires wind measurements representative over the valley cross-section. Single vertical profiles are not representative for the entire valley cross-section since horizontal homogeneity can not be assumed. In the absence of adjustments to

single wind profiles, substantial overestimates of the VVF are expected (King, 1989). An empirical weighting factor has been demonstrated to account for the cross-valley variation of the along-valley wind speed (Freytag, 1987; Clements et al., 1989; Rucker et al., 2008).

Previous studies have proven the potential of the VVF method for investigating thermally driven flows and associated exchange processes. These studies have implemented the VVF method using wind measurement data from pilot balloon ascents (Freytag, 1987), aircrafts (Henne et al., 2004), and ground-based Doppler wind lidars (DWLs) (Clements et al., 1989; Rucker et al., 2008). Freytag (1987) computed the mass budget of the Austrian Inn Valley during mountain and valley wind periods using data from the March 1982 MERKUR experiment. Their mass budget analysis enabled the determination of compensating vertical motions in the valley atmosphere, including subsidence associated with daytime up-slope flows and subsidence compensating for valley wind divergence and flow into the tributaries. Henne et al. (2004) quantified topographic venting using airborne measurements in the Swiss Leventina and Mesolcina valleys during the VOTALP and CHAPOP field campaigns in the summers of 1996, 1998, and 2000 through a mass-budget analysis. Their results indicate that daytime thermally driven circulations enable an efficient vertical export of boundary-layer air. Under fair-weather summer conditions, this process can produce up to three complete exchanges of the up-valley wind-layer air mass per diurnal cycle, thereby contributing substantially to the coupling between the MoBL and the free troposphere. Similarly, Weigel et al. (2007) applied high-resolution large-eddy simulations (LESs) in the Swiss Riviera Valley to calculate vertical mass and moisture fluxes, showing that mechanisms such as valley narrowing and interactions of cross-valley circulations can dominate over turbulent fluxes.

Clements et al. (1989) quantified the mass flux of the nocturnal drainage flow in the deep Brush Creek Valley in the United States using a DWL. Rucker et al. (2008) used a similar method to quantify the VVF along the Wipp Valley in Austria, a major tributary of the Inn Valley. They found a VVF divergence during daytime up-valley flow, which would imply compensating subsidence above the valley, if no import through side valleys occurs. VVF divergence during daytime up-valley flow has previously also been found in the Inn Valley in measurements and simulations (Vergeiner, 1983; Freytag, 1988; Zängl, 2004). Similarly, in the Kali Gandaki Valley an acceleration of the along-valley wind component was found in a widening section of the valley (Egger et al., 2000; Zängl et al., 2001). Possible explanations for up-valley VVF divergence include valley-scale subsidence compensating for up-valley flow into the tributaries (Freytag, 1987), a pressure-gradient within the valley caused by differential heating (Rucker et al., 2008), and gravity waves causing supercritical flow (Zängl et al., 2001). However, it is challenging to obtain observational proof for these explanations. Previously developed VVF estimation methods that included DWL data were only tested for narrow valleys, such as the Brush Creek Valley and the Wipp Valley. The methods have yet to be tested in a broad valley, such as the Inn Valley or Adige Valley (German: Etschtal). Previous examinations in the Inn Valley relied on pilot balloon ascents (Freytag, 1987), which have a lower spatial and temporal resolution, as well as lower accuracy than modern DWL measurements.

The present thesis focuses on developing and testing novel methods for estimating VVFes using DWL observations in a broad valley. Specifically, it aims to identify optimal scanning strategies and reveal potential challenges in VVF computation, serving as a pioneering

effort to prepare for broader observational campaigns. This work represents the first comprehensive testbed that applies the VVF method in a broad alpine valley, combining ground-based and airborne lidar measurements. Its findings provide critical insights into atmospheric flow in complex terrain, advancing methodologies that can be directly applied to larger-scale initiatives.

The thesis is embedded within the preparatory efforts for the TEAMx observational campaign (TOC). Multi-scale **t**ransport and **e**xchange processes in the **a**tmosphere over **m**ountains – programme and e**x**periment (TEAMx) is an international research initiative aiming to improve the understanding and parameterization of exchange processes over mountainous terrain. It integrates coordinated observations, modeling, and theoretical work to bridge scales from turbulence to regional circulations (Serafin et al., 2020). As part of the TOC, in the context of the **Li**nking **va**lley flow and **vert**ical **ex**change in compl**ex** terrain (LIVAVERT(EX)^2) project, seven ground-based DWLs were deployed during summer 2025 in the Italian Province South Tyrol, which is part of the TEAMx Alpine Crest Target Area. The goal of the project is to advance understanding of atmospheric flow and vertical exchange in complex terrain by applying the VVF method to the extensive DWL network. Validation of the method is possible due to several flights during intense observation periods (IOPs) with the novel airborne DWL system **AIR**borne **f**ixed-beam **l**idar f**o**r **w**ind measurement**s** (AIRflows) in the vicinity of the ground-based measurement locations. In preparation for the TOC deployment, a small pre-campaign was conducted in the Austrian Inn Valley, a broad Alpine valley (see Figure 1.1), in September and October 2024. This pre-campaign should not be confused with the TEAMx pre-campaign in summer 2022 (TEAMx-PC22; Pfister et al. 2024). During the pre-campaign in 2024, a DWL was operated on the valley floor for 40 days, and the novel airborne lidar system was successfully tested over two flight days. The present study is based on the 2024 pre-campaign data.

1.2. Research goals

The present thesis provides essential groundwork for the analysis of the observations collected during the TOC by testing, validating, and extending methods to estimate VVF from the pre-campaign observations in the Inn Valley. The specific objectives of the thesis are:

- To identify and address potential challenges in computing VVFes from DWL data in a broad valley.
- To test and validate the VVF method using both ground-based and airborne DWL observations.
- To provide a methodological framework and recommendations for the analysis of the TOC measurements.
- To determine whether the daytime up-valley divergences observed in previous studies (Freytag, 1987; Rucker et al., 2008) can also be found in the present dataset of the Inn Valley.

Figure 1.1.: View of the Inn Valley looking northeastward during a measurement flight. The yellow arrow indicates the location of the ground-based Doppler wind lidar in Kolsass. Photo by Philipp Gasch, edited by the author.

- To tentatively evaluate whether a LES can reproduce the observed diurnal cycle of the VVF on the basis of two days.

Importantly, the methodological developments and preliminary results from this work already informed and guided the deployment and scanning strategies for the TOC.

The thesis is organized as follows: Chapter 2 introduces the fundamentals of the MoBL and diurnal mountain winds. Chapter 3 presents the instrumentation, the study area, and the model setup. Chapter 4 includes a detailed description of existing methods to calculate the VVF, as well as adaptations performed to apply these methods in the broad Inn Valley. Chapter 6 presents the VVF calculated from ground-based DWL data and compares it with the airborne-derived VVF. Chapter 7 presents a comparison of the valley flow across the entire valley cross-section between the model and the airborne measurements, as well as a comparison of the modeled VVF with observations. It also presents a method to use LES to gather information on cross-valley variability of along-valley flow. The thesis ends with the conclusions and an outlook with recommendations for the analysis of the TOC dataset in chapter 8.

2. Theoretical background

2.1. The mountain boundary layer

The ABL is described by Stull (1988) as "the part of the troposphere that is directly influenced by the presence of the Earth's surface forcings with a time scale of about an hour or less". A sketch of a typical diurnal cycle of the ABL is shown in Figure 2.1.

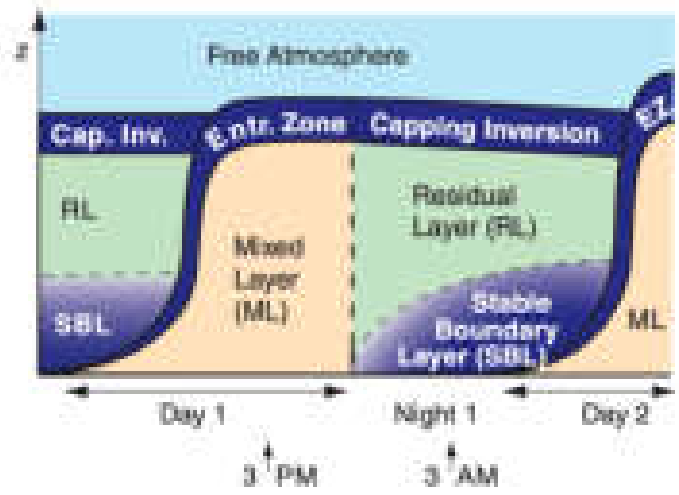

Figure 2.1.: Diurnal cycle of the atmospheric boundary layer over flat land during fair weather conditions. "Entr. Zone" and "EZ" stand for "Entrainment Zone". Reprinted from Stull (2017). Licensed under CC BY-NC-SA 4.0

This classical definition, and much of the foundational theory in boundary layer meteorology, was developed primarily for flat and horizontally homogeneous terrain. However, in mountainous regions the governing processes such as turbulent exchange, surface heat exchange, and radiative transfer become significantly more complex due to the multi-scale interactions. Exchange processes in the MoBL include, e.g., orographic gravity waves, thermally-driven circulations, moist convection, and turbulent motions (Lehner and Rotach, 2018). In addition to a local diurnal cycle of potential temperature, the diurnal cycles of thermally driven winds dominate the MoBL. A sketch of the diurnal cycle of stability and valley winds is shown in Figure 2.2.

The ABL height is used as a metric to determine up to which height the flow is turbulent, or up to which height atmospheric variables are determined by turbulent mixing (Lehner and Rotach, 2018). In mountainous terrain, the definition of a single, well-defined ABL height is often insufficient to capture the spatial and temporal variability observed in complex terrain. In idealized simulations, Wagner et al. (2015) defined the height of the ABL in

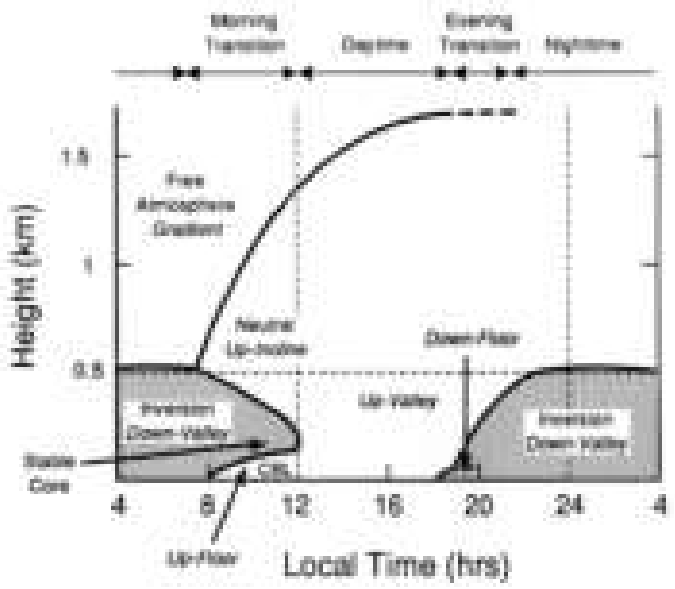

Figure 2.2.: Diurnal cycle of the stability (roman) and thermal circulation (italics) in a 500 m deep valley. "CBL" stands for "convective boundary layer". Reprinted from Whiteman (1990). Used with permission.

mountainous terrain as the height with the strongest potential temperature gradient. This definition may be sufficient in some cases and insufficient in others, but nevertheless the definition of the MoBL height remains one of the challenges in MoBL research. To overcome obstacles in transferring the ABL concept to complex terrain, research has sought to extend and adapt ABL theory to what is now referred to as the MoBL. Lehner and Rotach (2018) define the MoBL as "the lowest part of the troposphere that is directly influenced by the mountainous terrain, responds to surface and terrain forcings with time scales of about one to a few hours, and is responsible for the exchange of energy, mass, and momentum between the mountainous terrain and the free troposphere". The exchange of energy, mass, and momentum is determined by synoptic-scale dynamics, thermally driven circulations, and turbulent transport. Unlike homogeneous flat terrain, where there is a clear spectral gap between turbulence and mean flows, mountains generate spatially and temporally heterogeneous conditions that enhance the spectrum of relevant scales of motion (Babić et al., 2017) and thereby modify the efficiency of vertical exchange (Rotach et al., 2015). As shown in the comparison sketch of the various exchange processes in Figure 2.3, exchange processes over mountainous terrain are more complex and multi-scale than those over flat, homogeneous terrain.

2.2. Diurnal mountain wind systems

A characteristic feature of the MoBL is the presence of diurnal wind systems. These systems strongly contribute to vertical exchange and MoBL complexity. Thermally driven circulations define and are constrained by the MoBL structure.

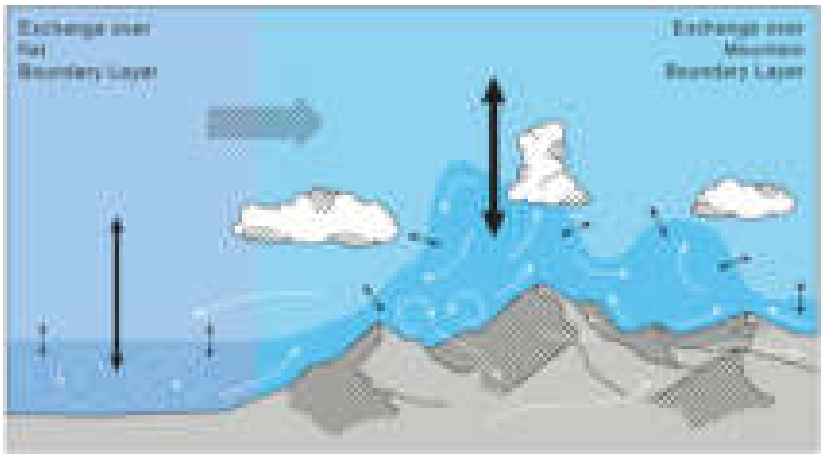

Figure 2.3.: Sketch of exchange processes of energy, mass and momentum in the atmospheric boundary layer over flat and mountainous terrain. Reprinted from Serafin et al. (2020). Licensed under CC BY-NC.

Diurnal mountain winds develop in valleys as a result of differential heating and cooling within the valley and between the valley and its surroundings. The resulting temperature and pressure contrasts depend on the spatial scale considered: slope versus valley center, valley versus plain, or mountain range versus foothills. Mountain wind circulations are most pronounced and strongest during synoptically undisturbed conditions but may also develop and interact with synoptic-scale winds and during disturbed conditions. The mountain wind system consists of four interacting wind systems: the mountain-plain wind system, the along-valley wind system, the slope wind system, and the cross-valley wind system (Whiteman, 2000). The four components do not operate independently but form an integrated, multi-scale thermal circulation system where each component influences and is influenced by the others through complex spatial, temporal, and dynamical coupling mechanisms. At times, these circulations are superimposed, resulting in wind speeds stronger than those produced by any single component alone. Other times, they weaken when, for example, synoptic winds oppose the direction of the valley wind. A sketch of the different circulations is shown in Figure 2.4.

2.2.1. Mountain-plain wind

The largest scale component of the diurnal mountain wind system is the mountain-plain wind system. It develops under calm and clear weather conditions in response to the temperature contrasts between the atmosphere above a mountainous area and the atmosphere above the adjacent plain. The temperature contrast leads to a pressure gradient that is balanced by the mountain-plain wind system. During daytime, the air over a mountainous region heats up faster than over the adjacent plain. In response, a low-level plain-to-mountain wind develops with a weak return flow aloft (upper panel of Figure 2.4). During nighttime, the air over the mountainous region cools faster than over the plain, and a mountain-to-plain wind develops with a weak return flow aloft (lower panel of Figure 2.4). The reversal is

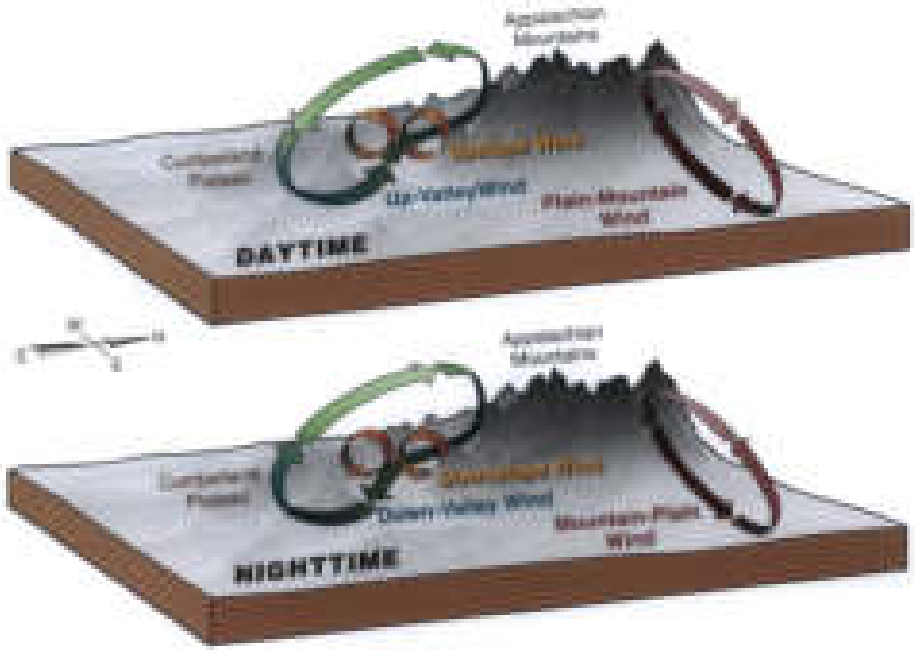

Figure 2.4.: Sketch of the diurnal mountain wind system at the example of the Appalachian Mountains for the daytime and nighttime situation. The mountain-plain wind system is in dark red, the slope wind system is in yellow/orange, and the along-valley wind system is in blue/green. The cross-valley wind system is not shown explicitly but can be seen as an extension of the slope wind system. Reprinted from Whiteman (2000). Used with permission.

delayed compared to other mountain wind systems due to the large air mass that needs to be heated or cooled (Whiteman, 2000; Zardi and Whiteman, 2013).

An example of the mountain-plain wind circulation is the horizontal transport from the Alpine foreland to the Alps on clear summer days and vice versa during the night. Here, the regional-scale mountain-plain wind system is superimposed on local slope and valley wind systems. This thermal system also has a vertical component, which enhances the exchange between the ABL and the free troposphere. The circulation is known as “Alpine pumping” (Lugauer and Winkler, 2005) and is strongest on days with weak upper-level flow and high incoming solar radiation. The inflow layer can reach up to 100 km north of the Alps (Lugauer and Winkler, 2005; Graf et al., 2016). The daytime inflow layer has been found to be more than 1000 m deep in observations and numerical simulations (Weissmann et al., 2005; Graf et al., 2016), while the nighttime outflow layer can be up to a few hundred meters deep (Graf et al., 2016). The mountain-plain wind circulation between the Alpine foreland and the Alps can interact with overlying synoptic flows, enabling penetration into the Inn Valley and producing localized down-slope winds, which in turn generate cross-valley temperature gradients and enhance turbulent mixing even under weak synoptic forcing (Fritz, 2023). In a related way, the northerly plain-to-mountain wind may intensify the afternoon flow in the Achen Valley (a major northern tributary of the Inn Valley), promote subsidence into the Inn Valley, and modify the up-valley wind structure by shifting its core toward tributary entrances (Deidda, 2023). Similar mountain-plain wind systems have also been found in the

Rocky Mountains (Zardi and Whiteman, 2013), Japan (Kurita et al., 1990), the Southern Alps of New Zealand (Sturman and Wanner, 2001), and the North China Plain (Hu et al., 2022).

2.2.2. Along-valley wind

The along-valley wind system is a thermally driven circulation that develops due to horizontal temperature differences between air columns within a valley and those over the adjacent plains at the same altitude or further down-valley. During daytime, the valley atmosphere warms more rapidly than the surrounding plains, producing a relative low-pressure zone that drives up-valley winds (upper panel in Figure 2.5). In contrast, during nighttime, radiative cooling results in a higher pressure within the valley, leading to down-valley winds (lower panel in Figure 2.5; Zardi and Whiteman, 2013).

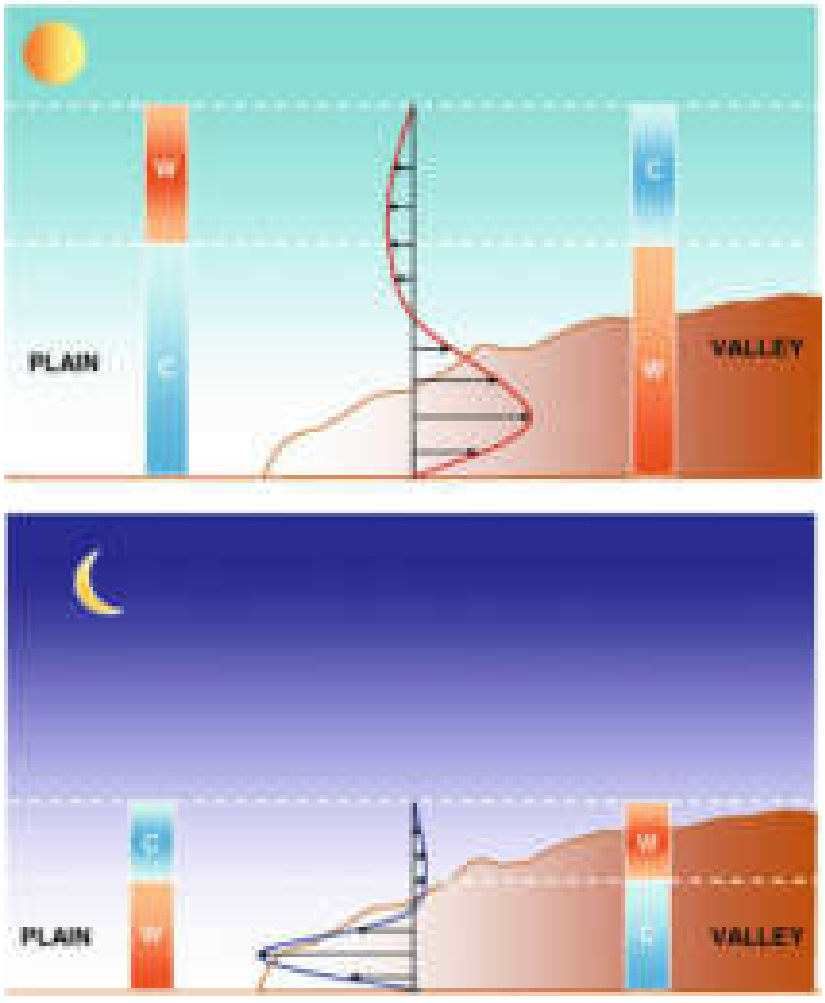

Figure 2.5.: Idealized visualization of the formation of along-valley winds during daytime (upper panel) and nighttime (lower panel) between a valley and an adjacent plain without a sloped floor. The red and blue colors in the columns represent relatively warmer (W) and colder (C) potential temperatures, respectively. Originally from Whiteman (2000) and modified by Zardi and Whiteman (2013). Used with permission.

The strength and variability of along-valley winds are largely influenced by along-valley temperature gradients, spatial variability in radiative fluxes arising from changes in albedo or emissivity, and variations in surface energy partitioning between sensible and latent heat fluxes (Whiteman, 2000). A key control on these temperature gradients is the valley volume effect determined by the cross-sectional shape. Idealized simulations by Wagner et al. (2015) show that reductions in valley volume, whether through an inclined valley floor or narrowing cross sections, substantially enhance up-valley winds. In their experiments, smaller valley volumes associated with a 0.86° valley floor incline increased up-valley winds by nearly a factor of two, while narrowing the valley cross-section amplified winds even more strongly. These topographic modifications also intensified vertical mass fluxes out of the valley and strengthened the inflow of air parcels from the foreland, underscoring the central role of valley volume and geometry in shaping thermally driven along-valley circulations.

Wagner (1932) first suggested that the valley air would heat and cool faster than the air above the plain, because of the smaller volume of the former. Originally, calculations were made for U-shaped valleys. Taking into account more convex sidewalls, which have a large influence due to the resulting smaller volume, produced better theoretical calculations of valley winds (Steinacker, 1984). The valley volume effect or "topographic amplification factor" provides an explanation for along-valley wind systems in valleys with weak valley floor slopes, such as the Inn Valley (Whiteman, 1990). In idealized simulations, Schmidli and Rotunno (2010) confirmed the importance of the valley volume effect for the formation of along-valley winds, while emphasizing that the assumption of negligible heat exchange with the free troposphere rarely holds. They also showed that the subsidence resulting from along-valley flow divergence plays an important role in the heating of the valley atmosphere during nighttime and the morning hours. In simulations of the Riviera Valley accompanying the MAP field campaign, Weigel et al. (2006) found that on two out of three simulated days the temperature gradient between the valley and the plain could not be explained by the topographic amplification factor alone. They found that subsidence of warm air from the free troposphere was the only major heating source on these two days.

LES studies have become a powerful tool for studying thermally-driven along-valley wind systems. Schmidli et al. (2011) led a major intercomparison study of mesoscale model simulations of the daytime valley wind system for an idealized valley-plain configuration. Special emphasize was placed on comparing the evolution of the along-valley wind. They found that the evolution of the mean along-valley wind was similar across models, except for time shifts of up to 2 hours between individual models. Wagner et al. (2015) investigated how valley geometry impacts thermally driven flows in an idealized valley. They found that a narrowing valley cross-section, as well as a sloping valley floor both lead to an increase in the along-valley wind speed. Recent work has also highlighted the role of valley-floor inclination. Using idealized WRF simulations, Mikkola et al. (2025) showed that daytime up-valley winds generally strengthen and penetrate deeper as the valley slope increases, up to a critical inclination beyond which they weaken. At night, flat valleys produce the strongest overall down-valley winds, although surface-based down-valley flow is more pronounced in inclined valleys. Valley inclination also enhances vertical tracer transport, making steeper valleys more efficient at ventilating pollutants to higher altitudes.

Up-valley winds typically have a depth of up to 1.5–2 km above valley floor (AVF) (Zängl and Vogt, 2006; Schmid et al., 2020). A low-level jet with a wind speed maximum of up to 8–10 m s^{-1} can develop in deep valleys (Schmid et al., 2020). In very deep valleys the maximum can exceed 15 m s^{-1} (Egger et al., 2000). In broad valleys the maximum along-valley wind speeds are generally lower (Wagner et al., 2015). The wind speed maximum is typically observed in the lowest few hundred meters (Zängl and Vogt, 2006; Schmid et al., 2020).

Down-valley winds are characterized by a jet-shaped wind speed profile, with peak speeds typically 3–10 m s^{-1} occurring at 30–60% of the inversion depth (Zardi and Whiteman, 2013). These jets often intensify near valley exits, where horizontal pressure gradients are strongest, reaching speeds of 13 m s^{-1} in the Inn Valley (Zängl, 2004). In addition to local thermal forcing, nocturnal valley jets can be strongly influenced by midlevel synoptic pressure gradients, with the superposition of these forcings producing either layered flow structures or unusually strong down-valley winds exceeding 15 m s^{-1} (Schmidli et al., 2009).

2.2.3. Slope wind

Slope winds are another component of the thermally driven mountain wind system. They are driven by buoyancy forces, which develop due to the warming and cooling of the layer adjacent to the slope, compared to the air at the same height in the center of the valley (e.g., Whiteman, 1990). They are primarily driven by the diurnal cycle of solar radiation. Typically, up-slope (anabatic) winds develop during daytime on sun-exposed slopes, and down-slope (katabatic) winds develop during nighttime. At night, cold and dense air descends from the slopes.

The buoyancy forces, as the drivers of the slope wind system, are strongest close to the surface. However, because of surface friction, peak wind speeds in slope winds occur at a certain height above the surface (Zardi and Whiteman, 2013). Up-slope winds can be a cause of subsidence in the valley center due to mass conservation (Brehm and Freytag, 1982). Up-slope winds during daytime and down-slope winds during nighttime were observed on most days during a summer campaign on a south-facing slope in the Italian Alps (Feigenwinter et al., 2010). Harnisch et al. (2009) found that up-slope winds also play an important role in aerosol redistribution during stable wintertime conditions, since aerosols were transported up-slope on the sun-exposed valley side, while the shaded side was not affected.

2.2.4. Cross-valley wind

The cross-valley wind system, oriented perpendicular to the valley axis, is most commonly a symmetric circulation. It can be seen as an extension of the slope-wind system (see “Upslope Wind” and “Downslope Wind” Figure 2.4). The symmetric cross-valley circulation consists of two stacked cells separated by the valley inversion. The lower cell involves the daytime up-slope winds and the compensating return flow from the slopes toward the valley center, while the upper cell is associated with strong thermals above the ridge (Schmidli, 2013). This type of circulation is the phenomenon most often associated with the term “cross-valley wind”.

In addition, asymmetric cross-valley winds can occur under specific conditions. They develop due to differential heating of opposing valley sidewalls, creating a horizontal

pressure gradient that drives flow from the cooler toward the warmer side of the valley (Gleeson, 1951; Bader and Whiteman, 1989). Asymmetric circulations may also arise from centrifugal acceleration of along-valley flow in a valley bend (Babić et al., 2021). Cross-valley vortices related to these processes have been observed during both the MAP-Riviera campaign (Weigel and Rotach, 2004) and the CROSSINN campaign (Babić et al., 2021), the latter conducted at the same site as the present study. These vortices primarily occur during periods of intense daytime up-valley flow (Babić et al., 2021).

2.2.5. The wind system of the Inn Valley

Along-valley winds in the Inn Valley have been examined in several field measurement campaigns (e.g., Dreiseitl et al., 1980; Müller et al., 1984; Freytag, 1987; Vergeiner and Dreiseitl, 1987) as well as in modeling studies (e.g., Zängl, 2004, 2009; Deidda, 2023; Fritz, 2023; Lezuo, 2023; Mancho Bacaicoa, 2024; Wibmer, 2024). Up-valley winds typically begin with a delay of 4–5 hours after sunrise due to the large volume of the valley (Vergeiner and Dreiseitl, 1987), and surface pressure differences of about 5 hPa can develop over a distance of 100 km (Vergeiner and Dreiseitl, 1987). Further up-valley, the onset of the up-valley flow occurs later and its duration is longer than at the valley exit (Müller et al., 1984). A typical wind field in the Inn Valley at 16 UTC under synoptically undisturbed conditions is shown in Figure 2.6. The maximum along-valley wind speeds are found west of Schwaz, near Kolsass, with a distinct minimum west of Innsbruck (Zängl, 2004). Up-valley winds generally reach higher peak speeds (8 m s^{-1}) than down-valley winds (5–6 m s^{-1} ; Müller et al., 1984). The height of the maximum wind speed is between 600 and 700 m above ground level (AGL) during the up-valley phase and between 200 and 700 m AGL during the down-valley phase (Müller et al., 1984). Near the valley exit, a low-level jet can develop around 200 m AGL with wind speeds up to 13 m s^{-1} (Zängl, 2004).

Tributaries also modulate the along-valley mass flux in the main valley. Qualitative analysis by Zängl (2004) suggests that northern tributaries from the Alpine foreland enhance the up-valley mass flux in the Inn Valley, whereas southern tributaries such as the Ziller Valley diminish it by extracting their up-valley flow from the main valley. Building on this, Deidda (2023) used high-resolution WRF simulations to examine how thermally driven winds in tributary valleys influence circulation in the Inn Valley. Their study considered four smaller and two larger tributaries. The quantitative results show that the smaller tributaries contribute mass fluxes at their mouths that are roughly one order of magnitude weaker than the main valley flow. Among the larger tributaries, the Ziller Valley exerts the strongest effect, reducing the main valley mass flux by about two-thirds during up-valley winds and enhancing it by roughly half during down-valley winds. In contrast, the Achen Valley typically exerts a much smaller and oppositely directed influence.

Additional insights into the Inn Valley wind system have recently been gained through the CROSSINN measurement campaign, which deployed an extensive network of in-situ instruments, remote-sensing systems, and aircraft observations near Innsbruck (Adler et al., 2021). A key feature of the campaign was the use of synchronized coplanar DWL scans, which enabled the detection of cross-valley circulation cells. Babić et al. (2021) further showed that the CROSSINN measurements revealed frequent cross-valley vortices in a curved section of the Inn Valley during strong up-valley flow, marked by a low-level up-

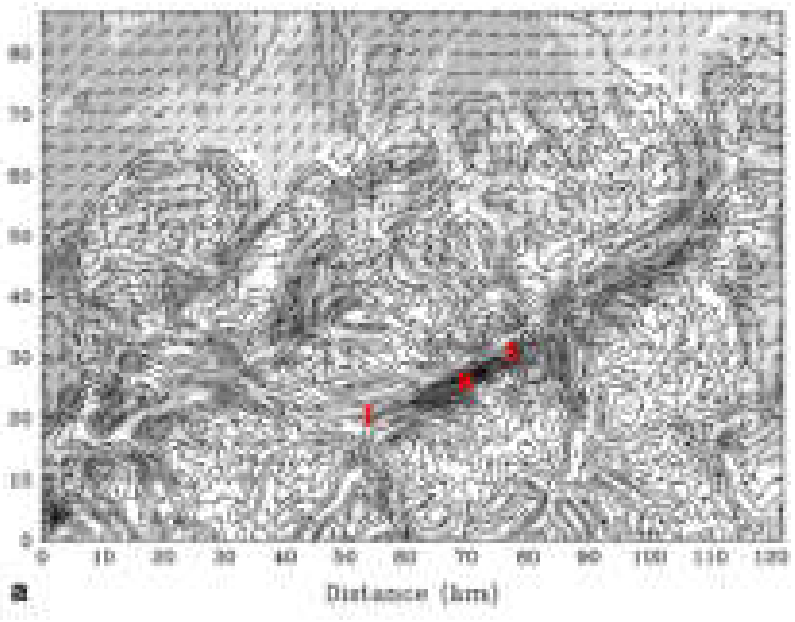

Figure 2.6.: Wind field during up-valley flow at 105 m AGL at 16 UTC under synoptically undisturbed conditions simulated with the MM5 model. Full wind barbs correspond to 5 m s^{-1}. The shading shows horizontal wind speed in 2 m s^{-1} increments. The solid contours show the model topography in 300 m increments. The locations of Innsbruck (I), Kolsass (K), and Schwaz (S) are marked with red letters. Adapted from Zängl (2004). Used with permission.

valley jet, clockwise turning with height, and flow cessation near ridge level. The occurrence and strength of these vortices were closely tied to the imbalance between centrifugal and pressure-gradient forces, with stronger up-valley winds producing faster vortex rotation.

Interactions of the Inn Valley wind system with large- and meso-scale flow

The interactions of valley winds with the large-scale flow are complex and poorly studied. Studies investigating the valley wind system are often idealized without synoptic forcing (e.g., Zängl, 2004; Schmidli and Rotunno, 2010, 2015) or on the basis of case studies for weak synoptic forcing (e.g., Goger et al., 2018; Adler et al., 2021; Babić et al., 2021). In the most extensive analysis of the influence of ambient flow on the valley wind in the Inn Valley to date, Zängl (2009) investigated how different wind directions of the large-scale flow influence the flow in the valley in simulations. The author found that if the synoptic wind blows in the same direction as the daytime up-valley wind (i.e., easterly in the Inn Valley), then the up-valley wind is intensified; if the synoptic winds are blowing in the opposite direction, then the the up-valley wind is weakened. Zängl (2009) also found that ambient flow with a southerly component leads to an intensification of the down-valley flow in the Inn Valley. Southerly flow can also excite gravity waves and lead to subsidence of warmer air in the Inn Valley and subsequently to a local pressure reduction (Zängl, 2003; Deidda, 2023).

Temperature differences between the air mass north and south of the main Alpine crest can lead to south foehn. The Wipp Valley is a north-south oriented tributary that is almost

perpendicular to the east-west oriented Inn Valley. The Wipp Valley is prone to foehn since it connects to the Brenner pass, the lowest pass of the Alps (1371 m above sea level (ASL)) (e.g., Gohm and Mayr, 2004). Foehn can break through into the Inn Valley, overcoming cold-air pools formed by nocturnal cooling (Haid et al., 2020). Before the foehn breakthrough, pre-foehn westerlies are commonly found in the cold-air pool with a wind speed maximum near Innsbruck (Zängl, 2003; Zängl and Gohm, 2006; Muschinski et al., 2021). These winds are the result of a local intensified along-valley pressure gradient. In addition, pre-foehn westerlies can enhance down-valley flow in the Inn Valley (Zängl, 2003; Umek et al., 2021). Foehn is mainly deflected eastward into the lower Inn Valley, where it then appears as a channeled westerly flow (Gohm and Mayr, 2004; Gohm et al., 2009). Stronger westerlies in the lower Inn Valley caused by foehn have the potential to modulate the VVF.

2.3. Observation-based studies on along-valley flow and volume (mass) budget estimations

Over the past 40 years, several observational studies have examined valley flows and computed volume (mass) budgets from wind observations. In the following analysis, air is assumed to be incompressible. This simplification is justified given that the analysis is limited to a small part of the lower troposphere (layer depth of about 1.5 km). The density difference between 500 m and 2000 m ASL is about 10%, so the resulting error is relatively small. This allows the air density to be treated as constant and mass fluxes to be expressed as volume fluxes. Volume flux budgets can be established from wind observations. A budget can be defined for a control volume with two cross-sectional interfaces and a lid. If the VVF is computed for both cross-sections, then it is known how much air volume (mass) is entering and leaving the control volume. If there are no other contributions, an indirect measurement of the area-averaged vertical exchange can be deduced. If tributaries are present, they can also contribute to the volume flux in the valley (Deidda, 2023). Other potential influences include mountain-plain circulation (Zängl, 2004; Fritz, 2023), synoptic flow (Zängl, 2009), and local effects (Laiti et al., 2014).

In one of the first studies to look at the VVF, Whiteman and Barr (1986) computed the nocturnal flux budget from data gathered with a tethered balloon. They find a volume flux divergence that is too large to be compensated for only by the down-slope flows or the inflow from the tributaries alone. Therefore, they hypothesize that subsidence is necessary to explain the observed divergence. Vergeiner and Dreiseitl (1987) performed an in depth analysis of the thermal winds in the Inn Valley and found a local increase in wind speed in a narrowing section between Jenbach and Schwaz. They explain this increase through mass continuity arguments. Freytag (1987) performed mass flux calculations from pilot balloon ascents during the MERKUR campaign in the Inn Valley. From the mass budget, they developed a concept of the thermal circulation during daytime and nighttime. They found an increase in the up-valley volume flux in up-valley direction. According to their calculations, subsidence above the valley is necessary to compensate for the up-slope winds and the flow into the tributaries during daytime. A field campaign in the very deep Kali Gandaki Valley revealed accelerations of the along-valley wind speed component in a wider

section of the valley (Egger et al., 2000). The authors hypothesize that this could be due to subsidence. These results were later also confirmed in model simulations (Zängl et al., 2001). During the VOTALP and CHAPOP field campaigns in the Leventina and Mesolcina valleys (Switzerland), mass budget estimates were calculated from airborne measurements to quantify atmospheric venting (Henne et al., 2004). They found a strong VVF convergence exporting up to three times the mass of the up-valley wind layer from the valley atmosphere to the free troposphere during undisturbed conditions in summer. Many of the mentioned studies estimated the volume/mass fluxes from single vertical wind profiles at the center of the valley. The error resulting from using an unrepresentative profile or neglecting cross-valley heterogeneity could then be greater than the resulting vertical flow estimated from the budget estimation (King, 1989).

Studies using Doppler wind lidars

In the past few decades, some studies have been published that examined the VVF using DWL. As part of the ASCOT program, several studies were conducted in the Brush Creek Valley (CO, USA). In one of these studies, Clements et al. (1989) examined the mean structure of the nocturnal drainage flow using a ground-based DWL. They used the obtained wind profiles to compute the VVF by reducing the measured wind speed at the center with a weighting factor to account for the non-homogeneity across the cross-section (see subsubsection 4.3.3.3). Similarly, Allwine (1993) used tracers, thetersondes and a DWL to determine the air volume flow rate during the nocturnal drainage flow and the morning transition. Moreover, volume scans with a DWL in the Grand Canyon were used to study the relationship between the flow within the canyon and above the rim under various ambient conditions (Banta et al., 1999). These studies demonstrated the potential of studying along-valley flow with DWLs early on.

During the MAP field campaign in 1999, a DWL was deployed in the Wipp Valley, a major tributary of the Inn Valley. In one of the most extensive VVF studies to date, Rucker et al. (2008) characterized the VVF using a method similar to that of Clements et al. (1989) (see subsubsection 4.3.3.1). In the Wipp Valley, a strong volume flux divergence was found during daytime up-valley flow (Rucker et al., 2008), similar to what had been previously observed in the Inn Valley (Vergeiner and Dreiseitl, 1987; Freytag, 1987) and in the Kali Gandaki Valley (Egger et al., 2000). The volume flux divergence in the Wipp Valley is shown in Figure 2.7, as the VVF increases in a section of about 3 km centered on the lidar, although the cross-sectional area is roughly constant.

Not only ground-based DWLs can be useful for flow studies in complex terrain, but also airborne DWLs have been used successfully to examine thermal circulations in complex terrain. De Wekker et al. (2012) used a scanning airborne DWL to observe the along-valley structure of the Salinas Valley (CA, USA). They observed an acceleration of the up-valley flow in up-valley direction due to a transitioning sea-breeze. They also found a cross-valley jet-like structure around ridge height and enhanced sinking motion. De Wekker et al. (2012) emphasize the potential of airborne DWL systems to investigate wind in complex terrain. In contrast to ground-based DWL systems, airborne DWLs provide spatially resolved flow measurements and can thereby resolve flow variation in along- and cross-valley direction.

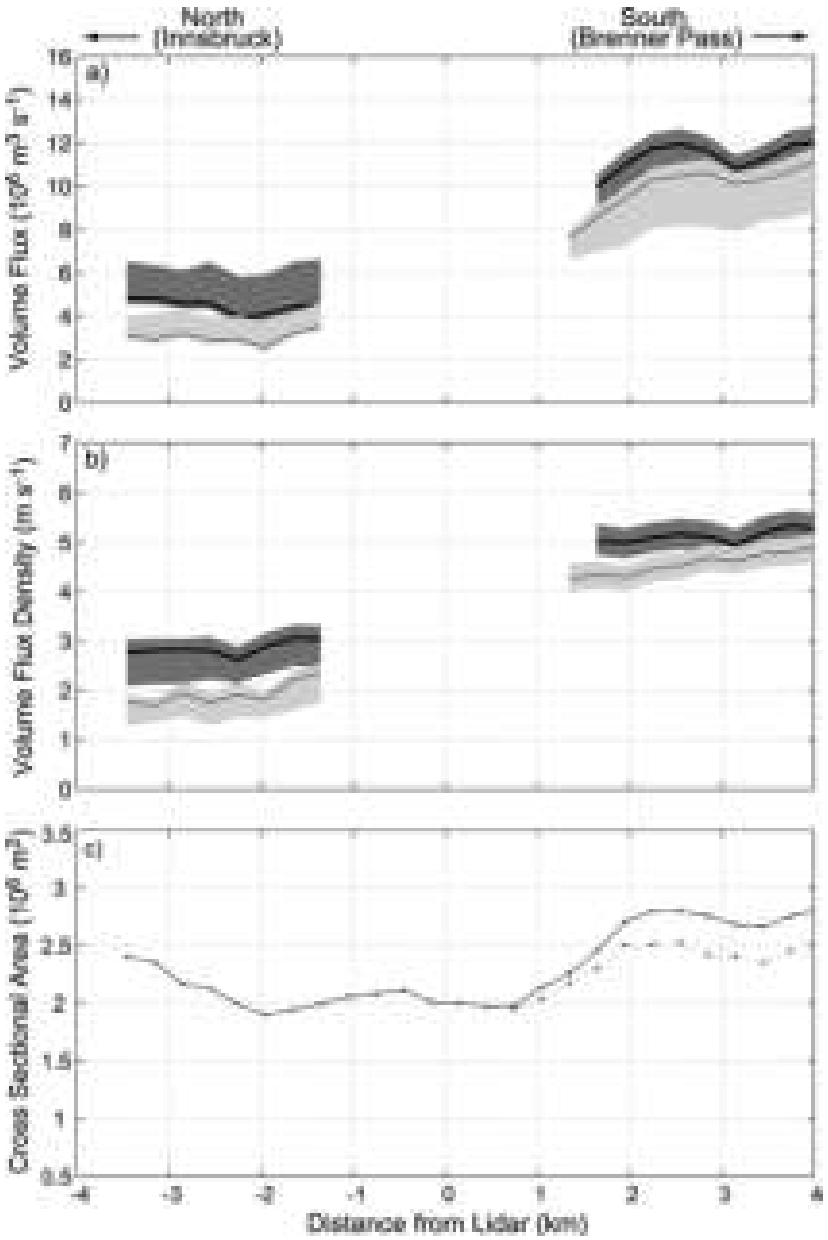

Figure 2.7.: a) Valley volume flux and b) volume flux density (~ average wind speed of the whole valley flow layer) as a function of along-valley distance in the Wipp Valley computed with data from a Doppler wind lidar for 17 Oct 1999 at 1353 UTC (heavy line) and 1425 UTC (thin line). The shaded areas show the uncertainty estimate. c) Cross-sectional area as a function of along-valley distance. The dotted line represents the cross-sectional areas for modified cross sections due to tributaries. Up-valley direction is to the right. Reprinted from Rucker et al. (2008). © American Meteorological Society. Used with permission.

3. Data

This study uses 38 days of DWL data obtained at the Kolsass measurement site during a test campaign in September and October 2024 in preparation for the TOC in summer 2025. In addition, measurement flights were conducted on two days during this period with the novel airborne DWL system AIRflows for validation. Furthermore, daytime LES runs with the ICOsahedral Nonhydrostatic (ICON) model are available for two days. This chapter is an introduction to the measurement location, the instruments, the model setup, and all the datasets used.

3.1. Location and period of observation

The measurement site is located in the municipality of Kolsass in the Inn Valley, Tyrol, Austria. The Inn Valley is a 517-kilometer-long valley that extends from the Swiss Engadin to the German pre-Alpine foreland. Kolsass, the measurement site, is located in the lower Inn Valley, approximately 18 km northeast of Innsbruck (see Figure 3.1). At Kolsass, the Inn Valley is approximately 2 km wide at the valley floor and approximately 15 km wide at ridge level. The valley is oriented ENE-WSW around Kolsass. The measurement site is located near the center of the valley floor, at 545 m ASL. The DWL data was collected using a Leosphere/Vaisala WLS200s system from 10 September to 20 October 2024 as part of a TEAMx pre-campaign. On 19 September, aircraft observations with the airborne DWL system AIRflows are also available. A total of four cross-valley transects were conducted over Kolsass and Vomp (5 km down-valley from Kolsass) during the morning hours between 0900 and 1000 UTC.

The orientation of the valley is visualized in Figure 3.2. The orientation (as seen from the lidar location) is 55° in down-valley direction towards Schwaz, 65° around Kolsass, and

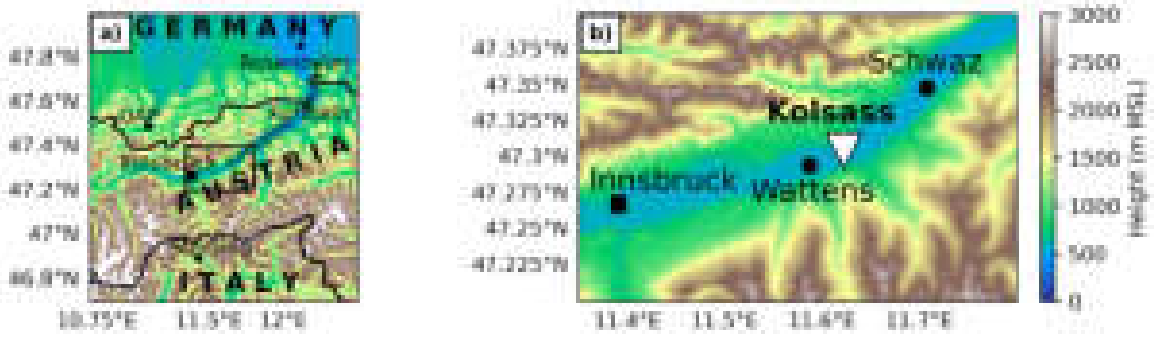

Figure 3.1.: Orographic map of a) the Eastern Alps and b) the investigation area in the lower Inn Valley. The white triangle marks the location of the ground-based Doppler wind lidar.

250° in up-valley direction towards Wattens. These azimuth angles were used to define the respective perpendicular cross-sections for the VVF analysis. The terrain data originates from a lidar-based Digital Terrain Model (Sonny, 2024).

The lidar operation was affected by a 6.75° azimuth direction offset due to improper alignment during installation. Corrections were applied (see section 4.2). In addition, the valley orientation was determined to be slightly different from the chosen along-valley scanning direction. Consequently, the along-valley wind speeds derived from the range height indicator (RHI) scans were projected into the true along-valley direction (see Equation 4.5).

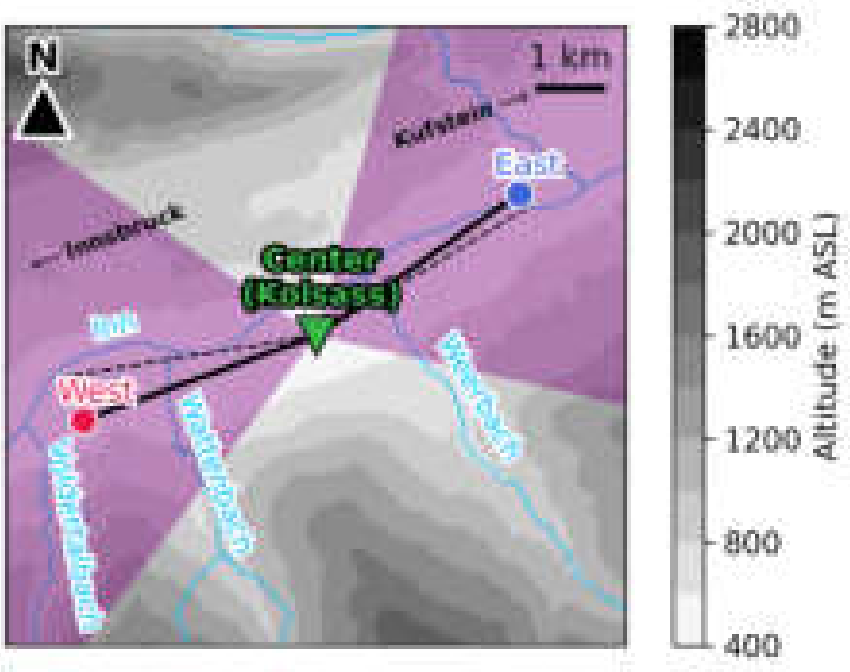

Figure 3.2.: Orographical map of the study area. Included are the angles (solid black lines) of the valley orientation, the actual angles at which the range height indicator (RHI) scans were conducted (dashed black lines), and the location of the lidar in Kolsass (green triangle) and the cross-sections at a distance of 4 km from Kolsass (colored dots). The purple shading shows the plane position indicator (PPI) sector scans. The main rivers and streams are in light blue.

3.2. Doppler wind lidar instrumentation

Heterodyne Doppler wind lidar (LIght Detection And Ranging) systems are active remote sensing instruments that are primarily used to measure the wind in the atmosphere from radiation scattered by aerosols. The principle of the DWL technique is described in more detail in Werner (2005). The wind speed is determined by taking advantage of the optical Doppler effect. In the case of a moving transmitter or receiver, light emitted at wavelength λ_0, has a frequency of $f_0 = \frac{c}{\lambda_0}$. The observed frequency with the velocity along the line of sight v is then

$$f = f_0 \left(1 + \frac{v}{c}\right), \tag{3.1}$$

where c is the speed of light. To measure the speed of moving aerosols, which by themselves do not emit light, they are illuminated by light from a laser. The frequency of the light scattered by the aerosols, which move with a certain speed, is detected at the receiver with a shift as

$$f = f_0 + \Delta f = f_0 \left(1 + \frac{2v}{c}\right). \tag{3.2}$$

The velocity of the particle along the line of sight (also called the radial velocity) is defined such that a positive shift results in movement away from the lidar and positive radial velocity. A negative shift translates into a negative radial velocity towards the lidar. A schematic of the frequency shift can be seen in Figure 3.3.

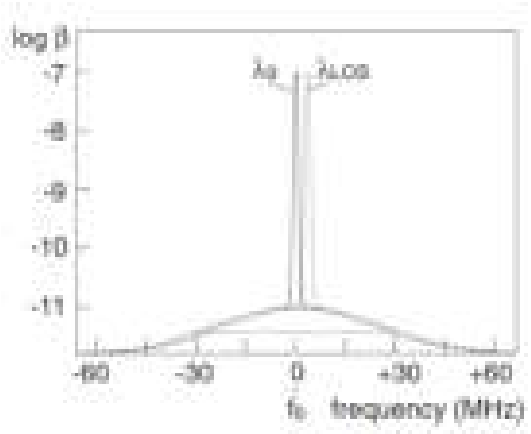

Figure 3.3.: Schematic illustration of the original (solid) and wind-shifted (dotted) frequency distributions due to the optical Doppler effect. Reprinted from Werner (2005). Used with permission.

The most common DWL instrument type for atmospheric science applications is the pulsed DWL with heterodyne detection. With this detection technique, the return signal is mixed with a stable local oscillator of known frequency. The resulting beat signal is then used to estimate the frequency shift. The distance from which the measurement originates is determined based on the signal propagation time, i.e. the time between laser pulse emission and detection. To determine the frequency shift of the beat signal, the acquired detection signal is analyzed using fast-fourier transforms (FFTs). The number of points included in the FFT determines the range gate size, which is usually chosen corresponding to the pulse length. The peak location of the FFT spectrum yields the radial velocity, the peak height the carrier-to-noise ratio (CNR).

The lidar beam is directed in different directions using a scanner, measuring the radial velocity along each beam. Since each beam provides only one-dimensional wind information, multiple scans in different directions must be combined to retrieve the three-dimensional wind field. For a 3D wind vector, at least three measurements of the radial velocity in different linearly independent directions are necessary. This retrieval assumes that the wind field is homogeneous within the scanned volume. Erroneous wind speed retrievals can result from non-homogeneous flow within the scanned volume, e.g., due to turbulence (Bingöl et al., 2009). The spatial variability of wind on different scales makes wind retrieval with a DWL especially challenging in complex terrain (Bingöl et al., 2009).

3.2.1. Ground-based Doppler wind lidar

In this study, a Windcube WLS200s manufactured by Leosphere/Vaisala was deployed in Kolsass (Figure 3.4 and 3.1); a two-axis scanning system equipped with a coherent pulsed laser and operating with heterodyne detection. The output laser is class 1M (eye-safe). The main hardware characteristics and chosen settings can be found in Table 3.1.

Figure 3.4.: Leosphere/Vaisala Windcube WLS200s at the observation site Kolsass. Photo: Andreas Wieser.

Table 3.1.: Technical sheet of the Windcube WLS200S. The settings used for this study are in bold.

Wavelength	1.54 μm
Maximum power	5 W
Pulse width	800/**400**/200/100 ns
Pulse repetition frequency	7/**10**/20/40 kHz
Physical range resolution	100/**75**/50/25 m
Accumulation time	0.5–10 s (**1** s)
Radial velocity range	−30–30 m s^{-1}

Scan pattern

The scan pattern consisted of up-valley and down-valley RHI scans, cross-valley RHI scans, and plane position indicator (PPI) sector scans at 3°, 8°, 13°, 18°, 23°, 28°, and 33° elevation. An overview of the scan pattern can be found in Table 3.2. This scan pattern had a duration of around 20 minutes. The pattern was intentionally experimental, as one of the goals of the present study was to evaluate which scans are most useful for VVF estimation and where, for example, reduced scan speeds might provide additional benefit. Insights gained here directly informed the scanning strategy adopted for the DWLs deployed during the TOC.

The up-valley and down-valley RHI scans are the main source for the VVF calculation because they provide the best vertical resolution and the most direct measurement of the along-valley wind. Information on the cross-valley structure of the along-valley wind is

derived from the PPI scans at 8° elevation. Figure 3.2 illustrates the PPI sectors and the azimuths of the along-valley RHI scans, while Figure 3.5 shows the portion of the PPI scans lying within the valley at a distance of 4 km up-valley from the lidar.

The scan pattern does not support a full "volume scan" analysis in the sense of Banta et al. (1999). That study employed PPI scans at 0.5° elevation increments, whereas the present dataset has 5° increments beginning at 3°, resulting in substantially lower vertical resolution. In addition, the lidar range here (≈4–5 km) is considerably shorter than the >10 km range in Banta et al. (1999). Because the Inn Valley is wide, elevations >8° only capture the full valley width beyond ~4 km, near the instrument's range limit. Despite these limitations in range and resolution, combining the multi-elevation PPI scans can still provide tentative visualizations of the valley flow, and the cross-valley RHI scans may help identify cross-valley flow features.

Table 3.2.: Description of the Doppler wind lidar scans performed for this study. ϑ is the azimuth angle from north and φ is the elevation angle from a horizontal plane. $\delta\vartheta$ and $\delta\varphi$ denote the increment for stepped scans or the scanning rate. δt is the duration of a scan in minutes. The numbers have been corrected for the observed lidar azimuth orientation offset (see section 4.2).

Name	Type	$\vartheta_{\min}$	$\vartheta_{\max}$	$\delta\vartheta$	$\varphi_{\min}$	$\varphi_{\max}$	$\delta\varphi$	δt
DVRHI	Stepped RHI	13.75°	103.75°	45°	1°	59°	2° s^{-1}	1.5 min
UVRHI	Stepped RHI	215.75°	305.75°	45°	1°	59°	2° s^{-1}	1.5 min
RHI152.75	RHI	152.75°	152.75°	0°	1°	59°	2° s^{-1}	0.5 min
RHI332.75	RHI	332.75°	332.75°	0°	1°	59°	2° s^{-1}	0.5 min
DVPPI	Stepped PPI	16.7°	102.7°	2° s^{-1}	3°	33°	5°	5.5 min
UVPPI	Stepped PPI	216.7	304.7°	2° s^{-1}	3°	33°	5°	5.5 min

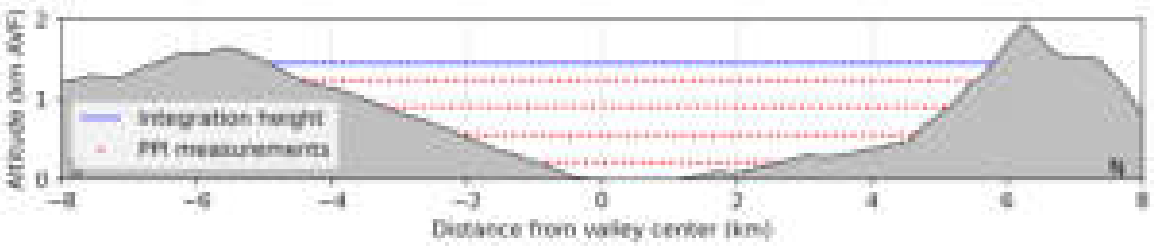

Figure 3.5.: Coordinates of the plane position indicator (PPI) measurements at 3°, 8°, 13°, and 18° elevation in the y-z-plane looking up-valley for a constant range gate at 4 km up-valley from the Doppler lidar (cross-section West in Figure 4.6). The integration height used for the valley volume flux calculation is shown as a blue line.

Retrieval of vertical wind profiles

The radial velocities retrieved from the DWL are processed into vertical profiles of wind components using the modular wind-profile retrieval software Atmospheric Profile Processing toolKIT (AtmoProKIT; Erdmann and Gasch, 2024). The software accepts radial

velocities as a function of time and range gate index (level 1). For each time step, there is a corresponding elevation and azimuth angle. The software produces a quality-controlled profile of wind components u, v, and w as a function of time and height AGL (level 2). The software uses all available scans for the profile retrieval. In the case of this study, the scans consist of PPIs and RHIs. The processing is an iterative process. Initially, a strict CNR threshold is applied for filtering. This is a first guess. Then, sequentially, the CNR threshold is lowered. Only data that are supported by sufficient good data points around them and that are within the expected range of the extrapolated previous guess are accepted. The level 2 wind profile retrieved in this study has a vertical resolution of 100 m and a temporal resolution of 10 min. This study uses both level 1 radial velocities and level 2 wind profiles.

3.2.2. Airborne Doppler wind lidar AIRflows

The novel airborne DWL system AIRflows was tested in complex terrain for the first time during this TEAMx pre-campaign. AIRflows flies aboard the Cessna F406 research aircraft operated by the Technische Universität Braunschweig, an unpressurized twin-engine turboprop. AIRflows consists of five small DWLs oriented in fixed directions (Figure 3.6). The multi-lidar, fixed-direction setup improves the resolution along the track by one order of magnitude compared to scanning systems (Gasch et al., 2023). Thus, the horizontal wind is retrieved with a resolution of 100 m in the along-track direction. The retrieval resolution in across-track is equal; however, the footprint in across-track direction is slightly larger than the distance from the aircraft to the ground. The lidar units can operate with three different pulse lengths (160, 320, 640 ns), which correspond to different along-beam resolutions of the radial velocity measurements (24, 48, 96 m). The selection of settings for a flight is determined by the aerosol concentration. Higher aerosol concentrations permit shorter pulse lengths and, consequently, higher vertical resolutions. The Inn Valley flight during the pre-campaign in September 2024 was conducted with a pulse length of 320 ns and 48 m range gate length processing. The radial velocity processing for the airborne DWL is similar to the processing of the ground-based DWL with the addition of a signal dependent averaging duration and distance. The profiles are corrected for motion with data from the aircraft. Quality controlled wind profiles were kindly provided by Dr. Philipp Gasch.

3.3. ICON-LES model setup

The ICON model is a global modeling system jointly developed by the German Weather Service and the Max Planck Institute for Meteorology (Zängl et al., 2015). It uses an icosahedral grid and works under the non-hydrostatic assumption. It can be used for a variety of applications, from numerical weather prediction to climate simulations. ICON allows flexible nesting from coarser NWP resolution down to LES resolution. In this study, ICON is used in a LES setup. The simulations are conducted and provided by Prof. Juerg Schmidli (Goethe University Frankfurt). The ICON-LES model simulations used were originally designed to assess the model performance in complex terrain above the Sarntal Alps (Schmidli, personal communication, 2025), by comparing the output to the AIRflows measurement flights on 18 and 19 September 2024.

Figure 3.6.: Left: Sketch of the Cessna 406 research aircraft of the Technische Universität Braunschweig with the airborne Doppler lidar (ADL) system AIRflows on board. Right: Photo of the five Doppler lidars of the AIRflows system pointing in fixed directions, photographed from below the aircraft. Courtesy of Dr. Philipp Gasch, combined by the author.

The model domain can be seen in Figure 3.7. The nested domain resolutions from outermost to innermost are 520 m, 260 m, 130 m, and 65 m. Since the innermost domain is centered on the Sarntal Alps, the domain that contains Kolsass well inside is DOM02 with 260 m grid spacing (see black star in Figure 3.7). The simulations were initialized at 0000 UTC on the corresponding day. The output is saved from 0600 to 1800 UTC and has an hourly temporal resolution. Online nesting was used, with boundary conditions updated at each time step. The model version ICON-2024.01-dwd-2.0 with 80 levels was used. The simulation was forced with the MeteoSwiss ICON-1-analysis. Standard physics was used on the outer domain and a Smagorinsky closure (Dipankar et al., 2015) on the inner domains. The topography originates from the ASTER dataset (NASA/METI/AIST/Japan Spacesystems and U.S./Japan ASTER Science Team, 2019) and has a resolution of 30 m.

3.4. Additional data

Topography dataset

The terrain data used for the terrain filter, to determine the valley width, and for plotting originate from a lidar-based Digital Terrain Model (Sonny, 2024). The 1" model was used, which has an approximate resolution of 20 m × 30 m.

ERA5

The global ECMWF Reanalysis v5 (ERA5) dataset by the European Centre for Medium-Range Weather Forecasts (ECMWF) is used to analyze the large-scale weather conditions during the measurement period and to produce the synoptic charts for the case study period (Hersbach et al., 2020). ERA5 data are also used to identify synoptically undisturbed days. ERA5 has a resolution of 0.25° × 0.25°.

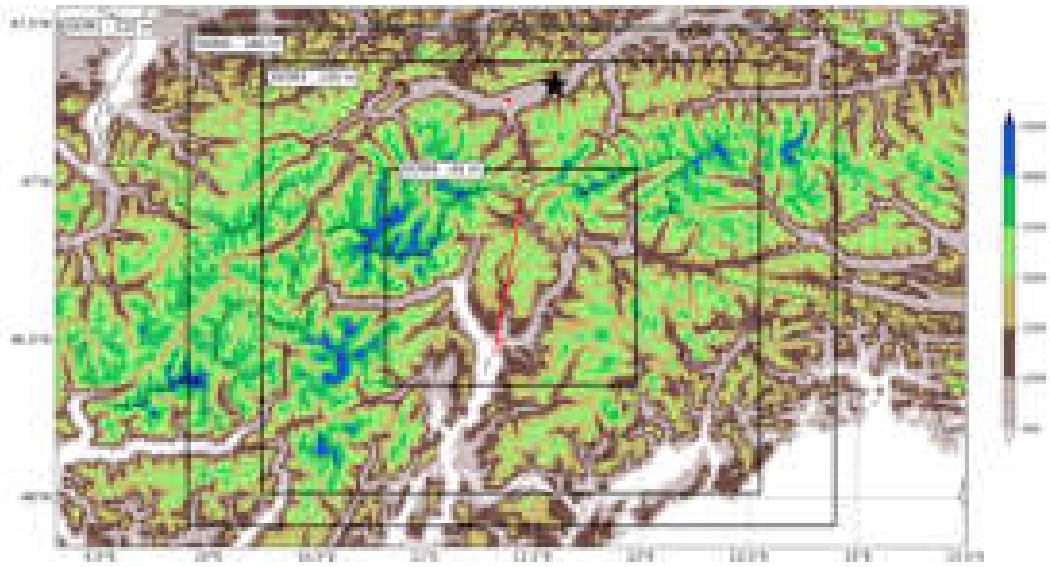

Figure 3.7.: Altitude in m ASL and the domains of the ICON-LES runs with corresponding resolutions. The black star marks the measurement site Kolsass. The southern red diamond marks Bozen/Bolzano, the northern one marks Innsbruck. Adapted from a figure provided by Prof. Juerg Schmidli (Goethe University Frankfurt).

Weather stations and radiosoundings

Data from the Innsbruck Box (i-Box) network station Kolsass (Rotach et al., 2017) operated by the University of Innsbruck are used to assess local weather conditions at the measurement site (`https://acinn-data.uibk.ac.at/pages/i-box-kolsass.html`). Data from the weather station at the University of Innsbruck are used to determine daily sunshine hours (GeoSphere Austria, `https://data.hub.geosphere.at/`). The daily radiosoundings at 0300 UTC from Innsbruck Airport are used to determine the stability in the valley (University of Wyoming Radiosonde Archive, `https://weather.uwyo.edu/upperair/sounding.shtml`).

Doppler wind lidar Innsbruck

Data from a permanently installed DWL on the rooftop of the Department of Atmospheric and Cryospheric Sciences of the University of Innsbruck (613 m ASL) complemented the analysis of the DWL data in Kolsass. The model is a StreamLine XR (SLXR142) manufactured by HALO Photonics. The vertical profiles used in this study are 10-minute averages based on PPI scans at 70° elevation. These profiles were processed and provided by Assoc. Prof. Alexander Gohm (University of Innsbruck). Note that the Innsbruck lidar data was not processed with AtmoProKIT, unlike the Kolsass lidar data.

Cloud observations

The presence of clouds in the Inn Valley is evaluated using the SEVIRI HRV Cloud RGB satellite product by EUMETSAT (`https://user.eumetsat.int/resources/user-guides/`

hrv-clouds-rgb-quick-guide). In addition, the SYNOP reports from the Innsbruck Airport weather station are consulted for cloud heights and types (https://www.ogimet.com/).

4. Methodology

This chapter describes the processing and quality control of the DWL data. The procedure used to determine the exact lidar orientation during post-processing is outlined. In addition, the calculation of the VVF is explained in detail, including sections for each component of the integration. Several methods to estimate the weighting factor are tested and presented. Finally, a new method to estimate the weighting factor is shown.

4.1. Quality control of radial velocity measurements

The processing of the instrument specific data format into standardized level 1 data was done using the AtmoProKIT wind retrieval software by Erdmann and Gasch (2024). For further analysis, the level 1 data is used, providing radial velocity—the velocity component along the line of sight—as a function of time and range gate with a temporal resolution of 1 s. AtmoProKIT also retrieves a quality-controlled wind profile every 10 minutes with a vertical resolution of 100 m. This processed dataset is referred to as level 2. The processing with AtmoProKIT is explained in more detail in subsection 3.2.1 “Retrieval of vertical wind profiles”. AtmoProKIT does not provide quality-controlled level 1 data.

Filtering of level 1 data is necessary due to three main sources of errors in the data. First, when the CNR is low, the radial velocity data becomes unreliable (i.e., the spectral peak used to obtain the radial velocities is not well pronounced anymore). However, a simple CNR threshold filter could exclude substantial amounts of acceptable data or include unreliable data. Second, hard target returns can occur due to ground interception or obstacles in the lidar beam path, introducing erroneous measurements that must be filtered out. Finally, larger flying objects and second-trip echoes (for shallow scans) can introduce other errors. An example of unfiltered level 1 radial velocities from a 8° PPI scan is shown in Figure 4.1a.

Level 2-based filtering

This filter validates the level 1 radial velocities using the level 2 background wind profile. It is applied by computing an expected level 1 radial velocity from the quality-controlled level 2 wind profile. Then, only measured level 1 data that fall within 3 m s^{-1} of the expected value are considered. The threshold of 3 m s^{-1} is large enough to allow for turbulent fluctuation but small enough to remove larger deviations. The threshold aligns with the threshold of the standard module chain of the DWL processing software AtmoProKIT. In cases of large variation of the wind speed along the valley the threshold may need to be adjusted accordingly. The expected background radial velocity (level 1 v_r) is derived from the level 2 zonal (u), meridional (v) and vertical (w) wind components for a given azimuth (ϑ) and elevation angle (φ), as defined in (4.1):

$$v_r = u \cdot \sin\vartheta \cdot \cos\varphi + v \cdot \cos\vartheta \cdot \cos\varphi + w \cdot \sin\varphi. \tag{4.1}$$

The result of the application of this filter is shown in Figure 4.1b.

Interpolation-based acceptance

For low elevation scans, the level 2-based filtering approach removes some valid data in the lowest 100 m due to its insufficient vertical resolution. Due to the coarse resolution, the gradient of the wind speed towards the ground cannot be adequately resolved. The level 2-based filter then causes small data gaps along a beam, where the expected radial velocity computed with the level 2 profile deviates more than $\pm 3\,\mathrm{m\,s^{-1}}$ from the single measurement. To mitigate this problem, linear interpolation is applied to the remaining level 1 data along a beam to fill the gaps. The interpolated values are then used as a reference and level 1 data points that fall within $3\,\mathrm{m\,s^{-1}}$ of the interpolated value are accepted; otherwise, they remain rejected. The interpolation-based acceptance is only necessary in few cases. The result of the application of this filter is shown in Figure 4.1c.

Ground return filtering

Ground returns, hard targets as well as data behind the topography are removed by comparing the measurements with a lidar-based Digital Terrain Model (Sonny, 2024). The range gate positions are calculated based on the known lidar position and the corresponding azimuth and elevation angles. Each range gate position is then compared to the terrain model, and data points within 50 m of the terrain surface, as well as those situated behind topographic obstacles, are excluded. The 1" model used for this process has an approximate resolution of 20 m × 30 m. The result of the application of this filter is shown in Figure 4.1d.

Removing isolated spurious measurements

Even after level 2-based and terrain-based filtering, spurious measurements can remain, since some radial velocity measurements fall into the valid range of the level 2-based filter by chance (since the lidar measurements are distributed across the full spectrum in case of noise). To remove remaining spurious measurements, a beam-wise rolling window filter is applied. The rolling window filter also increases data availability in the case of strong horizontal shear, i.e., when the level 2 wind profile may not be representative for the full retrieval volume scanned by the lidar. For each individual lidar beam, a rolling window of ten range gates is used to compute the fraction of valid measurements based on the number of non-missing (non-NaN) values. A data point is considered valid if the proportion of non-NaN values in the respective window exceeds 70%. This filters individual or smaller clusters of non-NaN values that are surrounded by NaNs. The process is performed independently for each measured beam. Visual inspection of lidar radial velocity measurements after applied quality filtering shows reliable performance of applied quality control procedures. The result of the application of all presented filters is shown in Figure 4.1e.

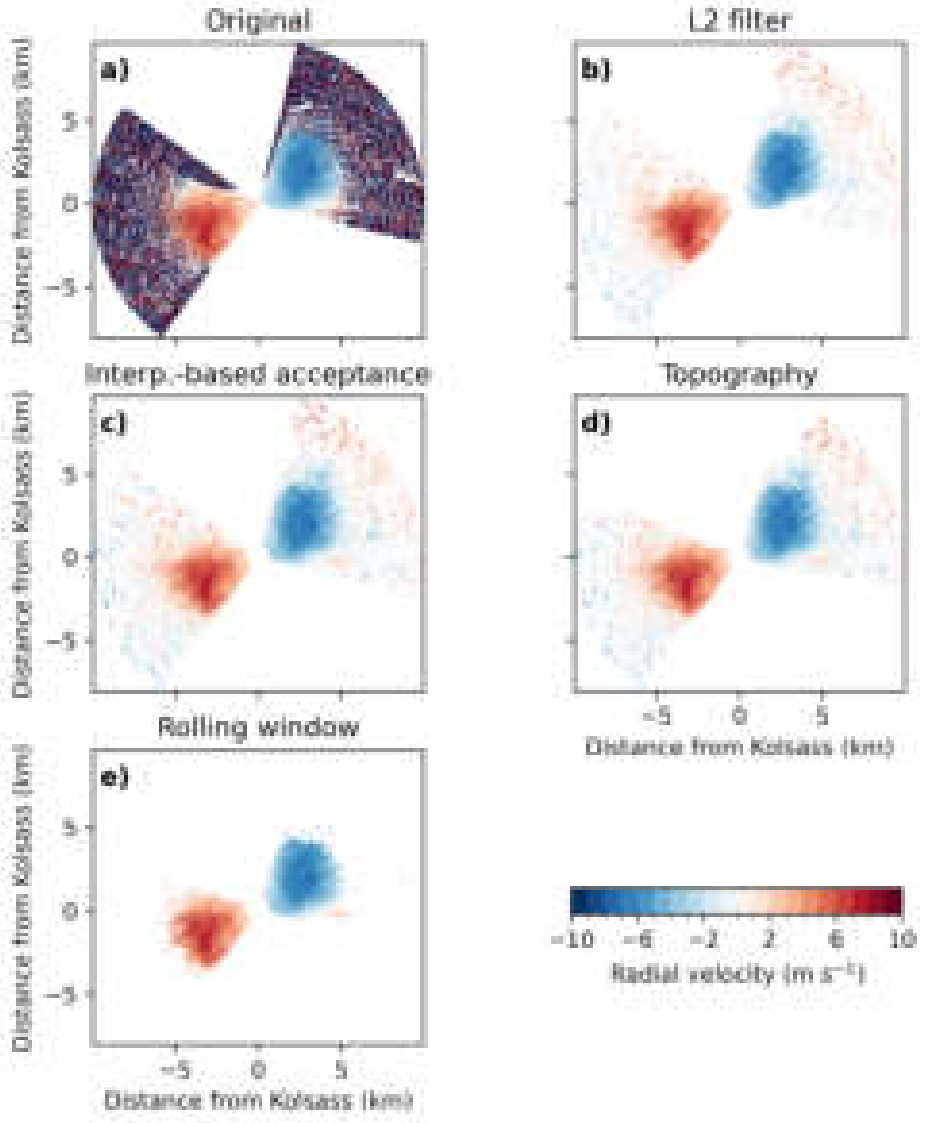

Figure 4.1.: Visualization of the sequential data quality filters applied to the radial velocity field from plane position indicator (PPI) sector scans at 8° elevation. Each panel incorporates all preceding filters: a) original dataset; b) after applying the Level-2-based filter; c) after the interpolation-based acceptance; d) after the topography filter; and e) after the rolling-window filter.

4.2. Lidar orientation correction

Orienting the Leosphere WLS200s DWL exactly towards the north in the field presents a challenge. A hand-held magnetic compass was used to determine the orientation. The compass can be influenced by nearby electronic devices, such as smartwatches or mobile phones. At the measurement site Kolsass there is the added challenge of power lines in close vicinity (see Figure 3.4). When standing a couple of meters from the lidar, it is hard to determine where the "north" face of the lidar is pointing, which introduces additional human error.

To address this challenge, several methods are employed to determine the azimuth offset from north. The methods use low-elevation PPI scans at 3° and 8°. For these scans, the CNR is displayed in combination with the topography mask described above (section 4.1 "Ground return filtering"). When the lidar beam hits topography, the CNR has a local maximum ("hard target"). For an optimally oriented lidar, the application of the topography mask should remove the hard targets signals seen in the lidar CNR. After applying the topography mask, some hard targets parallel to the valley axis remain (see Figure 4.2c), which is an indication that the lidar is not oriented true to north. The hard targets remaining after application of the topography mask can be evaluated to verify the azimuthal lidar orientation.

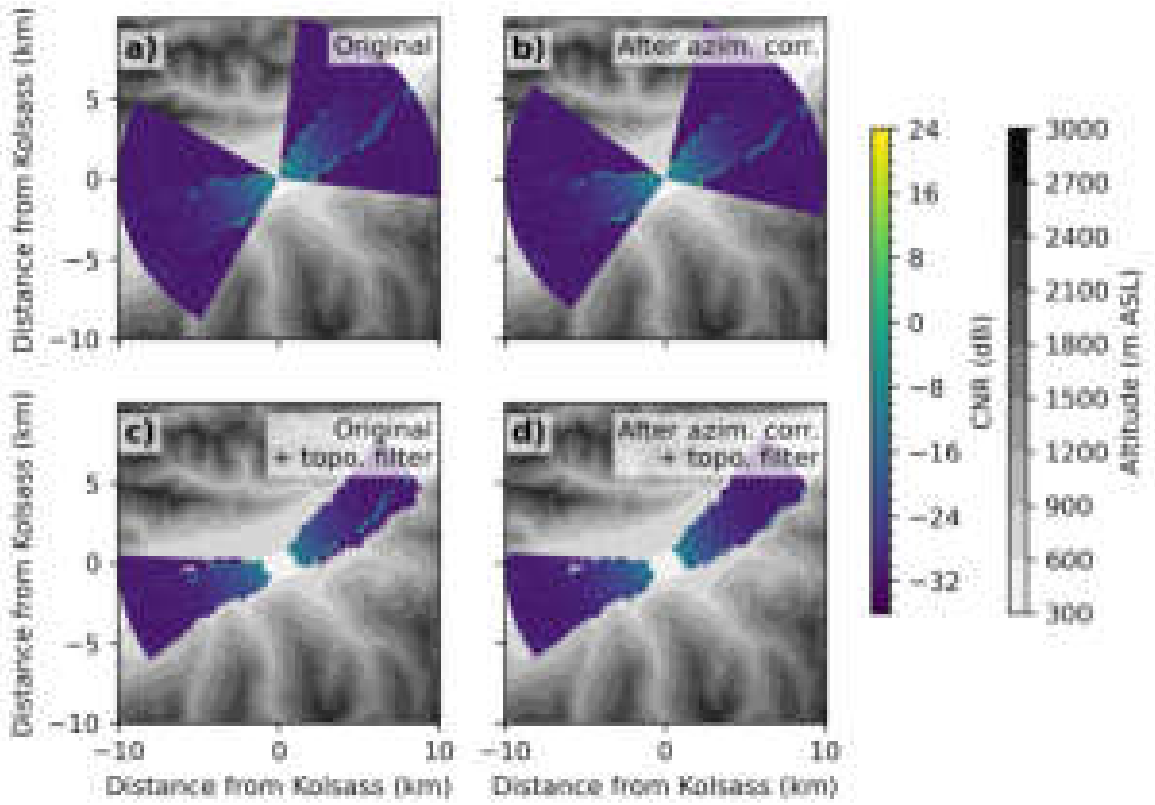

Figure 4.2.: plane position indicator (PPI) scans at 3° elevation of carrier-to-noise ratio (CNR) shown with altitude ASL as the background. a) Original dataset. b) Dataset rotated by 6.75° in the positive compass direction. c) Remaining data from the original dataset after applying the topography filter. d) Remaining data after rotation and application of the topography filter.

The offset from north is determined by varying the azimuth angle and applying the topography mask. Two different methods are applied to the PPI scans at 3° and 8° elevation to determine the offset. The first method quantifies the pixels with a CNR > 5 dB that remain after applying the topography mask. This number is then minimized by adjusting the azimuth offset (see Figure 4.3).

The second method involves counting the pixels with a CNR > 5 dB within the topography masked area. This number is then maximized by varying the azimuth offset again (see

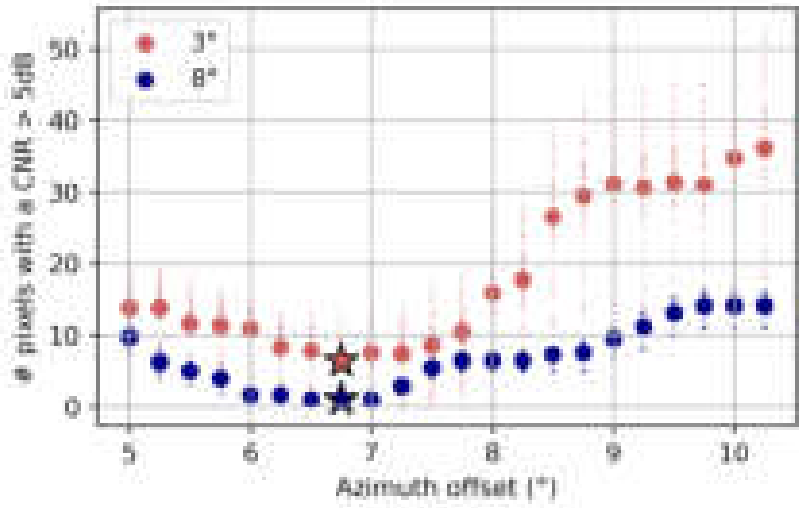

Figure 4.3.: Number of pixels with a carrier-to-noise ratio (CNR) larger than 5 dB after the application of the topography filter for plane position indicator (PPI) scans at 3° and 8° elevation as a function of correction factors added to the azimuth angle. The large dots show the means for each azimuth offset. The stars show the respective minima.

Figure 4.4). After testing various CNR thresholds, the most consistent results are observed at the 5 dB threshold.

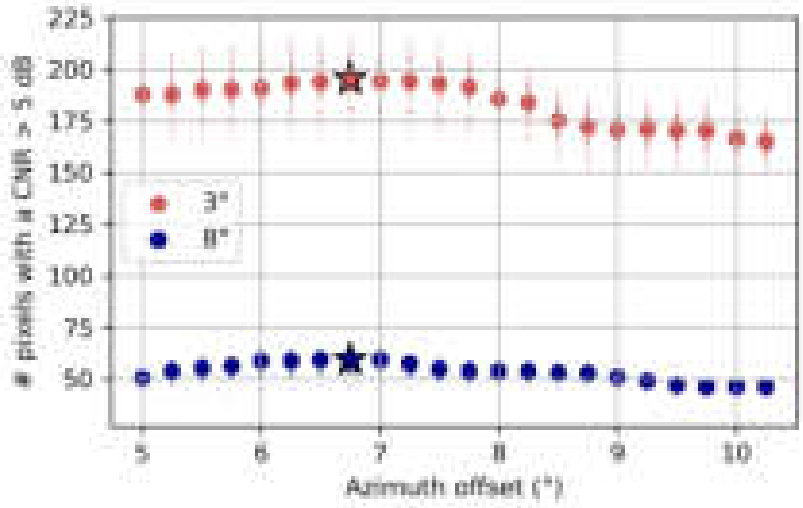

Figure 4.4.: Number of pixels in the topography mask with a carrier-to-noise ratio (CNR) larger than 5 dB for plane position indicator (PPI) scans at 3° and 8° elevation as a function of correction factors added to the azimuth angle. The large dots show the means for each azimuth offset. The stars show the respective maxima.

The findings indicate that the DWL has an azimuth offset of +6.75° ± 0.5°, with north set at 0° and positive being in the clockwise direction. The result is consistent with both methods.

Based on the discovery of the misorientation present in this study, procedures were developed for the TOC to align the DWLs more accurately toward the north. The orientation is determined via a hard target calibration. The scanner is pointed towards a known fixed and exposed position (e.g., a church tower), which can be seen as a local maximum ("hard target") in the CNR. The exact orientation of the scanner can then be determined since the azimuth angle of the lidar when pointing at the hard target is known, as well as the exact locations of the lidar and the hard target.

4.3. Calculation of the valley volume flux

The VVF quantifies the volume of air flowing through a valley cross-section. A schematic diagram of the proposed coordinate system can be seen in Figure 4.5, in which x is in along-valley direction, and y is in cross-valley direction.

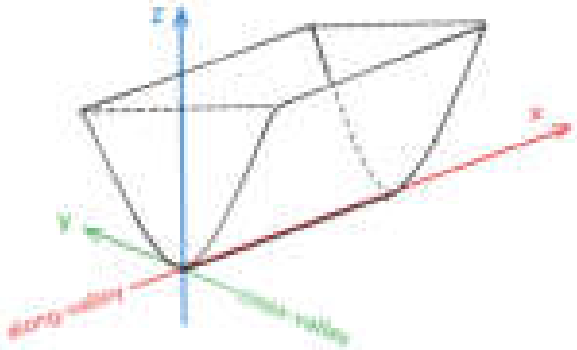

Figure 4.5.: Schematic diagram of the valley coordinate system.

The goal is to estimate the VVF at multiple cross-sections along the valley. These cross-sections are 4 km up-valley from the lidar (West), at the lidar site in Kolsass (Center), and 4 km down-valley from the lidar (East) (Figure 4.6). The distance of 4 km is chosen because it is the farthest distance from the lidar with good data availability. The VVF (Φ) for a location x along the valley can be calculated with (4.2)

$$\Phi(x) = \int_0^D F \cdot u_{\text{along}}(x, z) \cdot W(x, z) \mathrm{d}z, \tag{4.2}$$

adapted from Clements et al. (1989) and Rucker et al. (2008). Equation 4.2 includes the weighting factor F, which is part of the discussion of subsection 4.3.3. The valley-width W at each measurement height z is derived from a lidar-based Digital Terrain Model (Sonny, 2024). The integration height D is chosen as the average ridge height, which is 2000 m ASL, corresponding to approximately 1455 m AVF (see yellow contour in Figure 4.6). This choice is consistent with other studies in the area, such as Deidda (2023). In the following subsections the components of Equation 4.2 are explained in more detail.

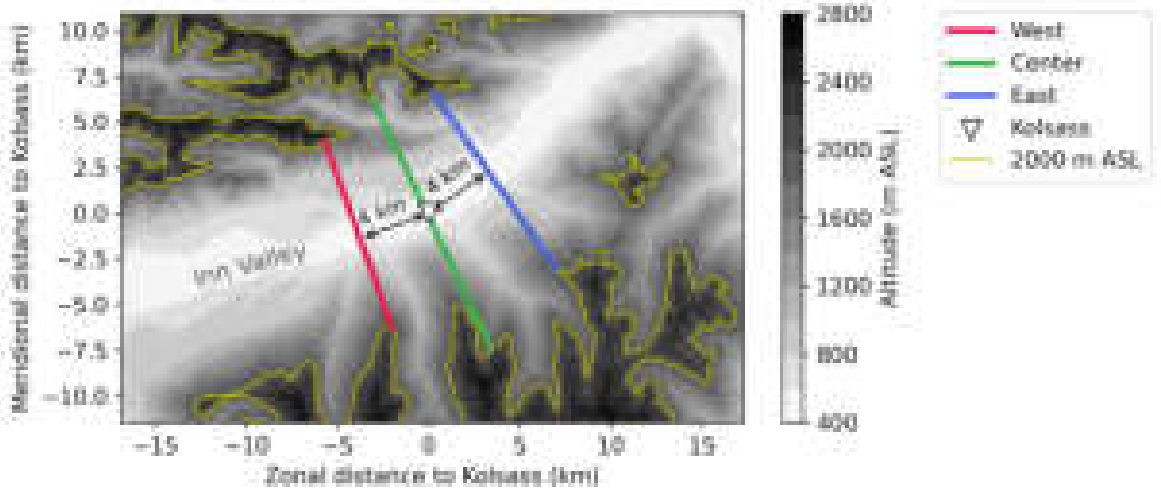

Figure 4.6.: Topographical map of the area around Kolsass, including the cross-sections at three locations, which were chosen for volume flux calculations: 4 km up-valley from Kolsass (West, red), Kolsass (Center, green), and 4 km down-valley from Kolsass (East, blue). The yellow contour denotes 2000 m ASL. Up-valley direction is to the left.

4.3.1. Valley width W

The valley width at every measurement height is determined with the help of a lidar-based topographical dataset (see section 3.4). The width is the distance between the two valley side walls at a certain height. The width is measured perpendicular to the local valley orientation. For this study, three locations were chosen for cross-sections: Kolsass (Center), and 4 km up-valley (West) and down-valley (East) from there (see Figure 4.6). The three cross-sections including the integration height of 1455 m AVF are shown in Figure 4.7.

4.3.2. Along-valley wind u_{along}

Estimating the VVF requires quantifying the flow through a valley's cross-sectional area, which is challenging. A simplified solution to the problem can be achieved using a wind profile at the center of the valley. The non-homogeneity of the along-valley wind can be accounted for by a weighting factor (see section 4.3.3).

For cross-section Center (Kolsass), the quality controlled level 2 wind profile of horizontal wind speed is used. The along-valley wind component u_{along} is calculated from the derived components u and v with equation 4.3

$$u_{\text{along}} = u \cdot \sin\gamma + v \cdot \cos\gamma, \tag{4.3}$$

where u and v are the zonal and meridional wind components, respectively, and γ is the azimuth of the valley orientation (degrees clockwise from north).

For the locations at a distance up-valley (West) or down-valley (East) from the lidar, the along-valley RHI scans (level 1) are utilized to extract a profile of along-valley wind. Vertical profiles of radial velocities are extracted at a distance of 4 km from the lidar, respectively,

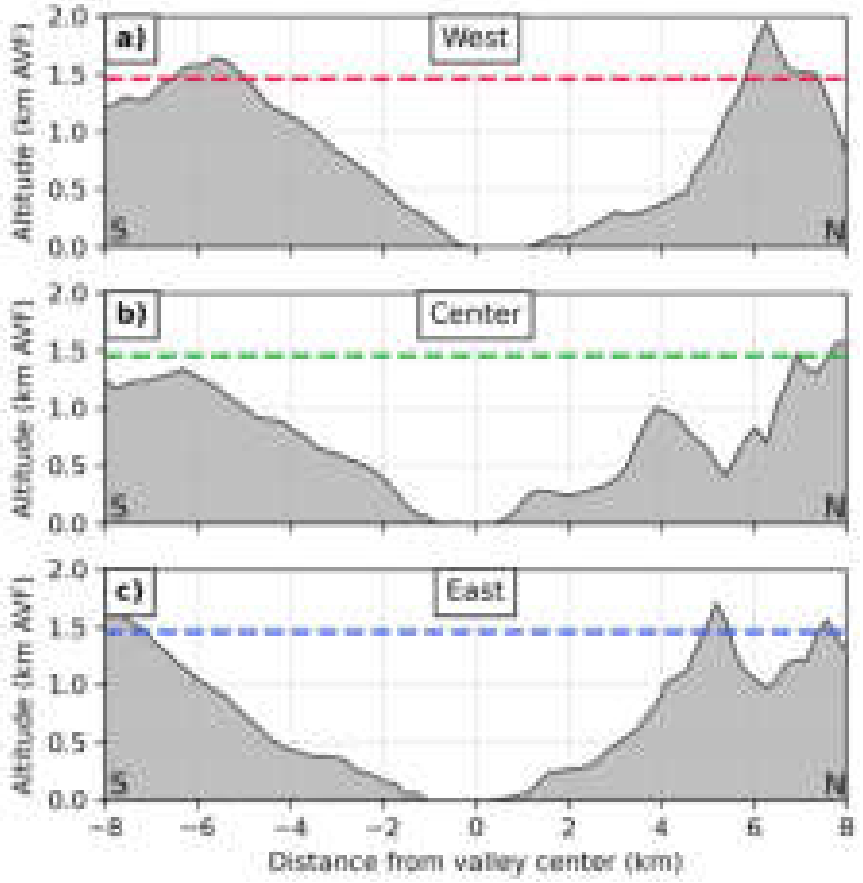

Figure 4.7.: Cross-sections of the topography perpendicular to the valley axis at cross-sections a) West, b) Center, and c) East. The locations of the cross-sections are shown in Figure 4.6. The viewing direction is up-valley. The dashed lines correspond to the integration height at 2000 m ASL or 1455 m AVF. Note the x- and y-axis are scaled differently.

with the nearest neighbor method. Deviations from the targeted 4 km distance when using nearest neighbors are on the order of 100 m within a profile. In order to estimate the along-valley wind speed, the radial velocity needs to be projected onto the horizontal plane. Since only shallow elevation angles up to 20° are used, the vertical velocity projection into the radial velocity is assumed to be zero. The assumption is that the wind vector is aligned quasi-horizontally. Thus, it can be derived that

$$u_{\text{along}} = \frac{v_{\text{r,along}}}{\cos\varphi}, \tag{4.4}$$

with the radial velocity in along-valley direction $v_{\text{r,along}}$ and the elevation angle φ.

Most wind profiles extracted from the RHI scans do not reach all the way to the ground due to insufficient data quality close to the surface (e.g., due to obstacles in the path of the lidar beam at low elevations, or due to fast scanning speeds). Thus, wind profiles are extended towards the ground assuming a logarithmic wind profile. This does not heavily affect the VVF because the minimum valley width is found at the surface. Thus, the wind

speed at lower levels only makes up a small part of the integration, since it is weighted by the valley width. For a visualization of the cross-sectional areas, see Figure 4.7. Intermediate missing levels are linearly interpolated.

The assumption of no vertical velocity is not necessarily fulfilled. The expected deviation for vertical wind speeds of 1 and 2 m s^{-1} increases with increasing elevation angle, as seen in Figure 4.8. For example, if the vertical wind speed was 2 m s^{-1} the deviation of the along-valley wind component is 0.75 m s^{-1} at a measurement elevation of 20°. This is in a similar range as the uncertainty of the wind measurement itself, which is estimated to be around 0.5 m s^{-1} .

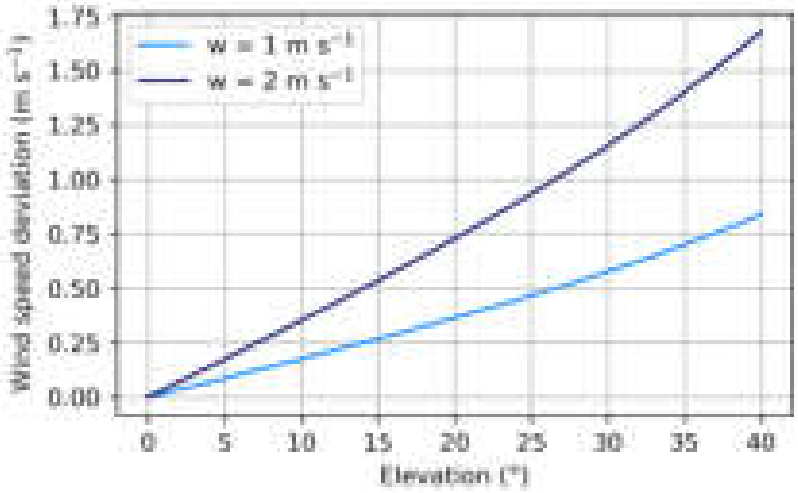

Figure 4.8.: Deviation from the true along-valley wind speed when assuming zero vertical wind, for theoretical vertical wind speeds of 1 and 2 m s^{-1} , as a function of elevation angle during the measurement.

It is assumed that the flow is solely directed in along-valley direction. This assumption is necessary to calculate the VVF using a single DWL. Babić et al. (2021) demonstrated the presence of cross-valley vortices in this curved section of the Inn Valley. The flow here is more complex than a purely along-valley motion. However, since cross-valley vortices do not occur continuously and, when present, their magnitude is typically half an order of magnitude smaller than that of the along-valley wind speed, the assumption of a predominantly along-valley flow is considered reasonable.

4.3.3. Weighting factor F

Estimating the VVF from a single profile can yield large errors, since it is often not representative for the entire cross-section (King, 1989). The weighting factor is a value which accounts for the heterogeneity of the along-valley wind speed within a valley cross-section. For a non-curved valley, the maximum wind speed should be at the valley center and the wind speed should be reduced toward the side walls. An idealized sketch that displays the heterogeneity of a non-curved valley section is shown in Figure 4.9.

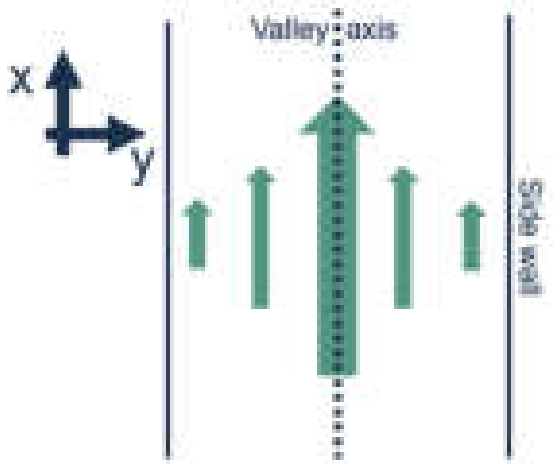

Figure 4.9.: Top view of an idealized sketch of the along-valley wind speed across a valley cross-section with the highest wind speed at the center of the valley. The wind speed is shown by the arrow size.

For the calculation of the VVF the along-valley RHI scans are used. RHIs only yield a single profile approximately at the valley center. Thus, the lower wind speeds towards the valley side walls need to be accounted for. In order to make the single profile representative for the entire cross-section, a weighting factor is introduced (Freytag, 1987; Clements et al., 1989; Rucker et al., 2008). Previous studies have determined several weighting factors for different valleys (see Table 4.1). They did this by examining the along-valley wind speeds as a function of distance from the valley axis using low elevation PPI scans. Their methods vary slightly, e.g., in the choice of elevation angle and in the time period averaged.

Table 4.1.: Previously determined weighting factors F in valley volume (mass) flux studies.

Study	Valley	F
Freytag (1987)	Inn Valley	0.85*
Clements et al. (1989)	Brush Creek Valley	0.7
Rucker et al. (2008)	Wipp Valley	0.87

*Based on Clements and Hoard (1987).

A direct comparison to the weighting factor determined for a section of the Inn Valley by Freytag (1987) is difficult. In the author's more extensive German publication, Freytag (1988) claims to have used the weighting factor presented by Clements and Hoard (1987) for the Brush Creek Valley (later published in Clements et al., 1989) and adapted it for the dimensions of the Inn Valley. It is not specified how the adaptation was performed.

The methods of Rucker et al. (2008) and Clements et al. (1989) are tested and extended to determine the weighting factor for this study. The following sections first describe the implementation of the original method by Rucker et al. (2008), which is explained in greater detail in Rucker (2003). Next, a combination of the methods by Rucker (2003) and Clements et al. (1989) is tested. Thereafter, an attempt at implementing the original

method by Clements et al. (1989) is also presented. Finally, the previously tested methods are extended to meet the needs of this study and the final weighting factor is determined.

4.3.3.1. Rucker (2003) method

The idea is to determine the variation of the along-valley wind across a valley cross-section from PPI scans. For the calculation of the weighting factor the PPI scans at an elevation of 8° are used (Rucker, 2003 used 10°). A shallow elevation is chosen to come as close as possible to a direct measurement of the horizontal along-valley wind. The 8° elevation is favored over the 3° scans since it offers better spatial coverage. The lowest elevation PPI scans have worse coverage due to the vicinity to the surface and low obstacles obstructing the lidar beam. For a more generalized approach, the weighting factors were calculated for three 8° PPI scans combined at a time, covering approximately a time span of 40 minutes together.

The cross-valley wind is assumed to be zero. However, this assumption does not always hold. Cross-valley winds of up to 2 m s^{-1} have been observed in this section of the Inn Valley (Babić et al., 2021). Similar to the calculation of u_{along} for the VVF integration, the along-valley wind is calculated for all beams of a PPI scan. Here, the calculation includes the azimuth angle and the valley orientation since a PPI scan also includes azimuth angles which are not in along-valley direction. The radial velocity v_{r} is projected horizontally in to the along-valley direction with

$$u_{\text{along}} = \frac{v_{\text{r}}}{\cos(\vartheta - \gamma) \cdot \cos\varphi}, \tag{4.5}$$

where ϑ is the azimuth angle from north, φ is the elevation angle from a horizontal plane, and γ is the local valley orientation. The wind vector is assumed to be horizontal and parallel to the valley axis throughout the entire cross-section. Potential errors could be introduced by thermally-driven cross-valley and vertical winds, as well as outflows from tributaries. Implications of the assumption of no vertical wind speed are shown in Figure 4.8. In Rucker (2003), the along-valley wind speed is averaged over three range gates of 300 m each. The method is adapted by averaging over range gates number 94–109, which correspond to distance from the lidar at the ground of 3686–4250 m and a height of 518–597 m AVF.

Rucker (2003) used the function (4.6)

$$\frac{u_{\text{along}}(y)}{u_{\text{m}}} = a\sqrt{1 - \left(\frac{y}{H}\right)^2}, \tag{4.6}$$

where u_{along} is the along-valley wind component as a function of distance from the valley axis y, u_m is the wind speed at the center of the valley, H is the valley half-width, and a is the parameter to be determined in a least-squares fit, which results in a weighting factor by using

$$F = \int_{-H}^{H} \frac{u(y)}{u_m} dy \overset{!}{=} a\frac{\pi}{4}. \tag{4.7}$$

The resulting fit does not fit well to the present data (see example in Figure 4.10). The calculation of the weighting factor according to Rucker (2003) assumes a symmetric parabolic curve with a maximum wind speed at the center of the valley. This may be true for straight sections or narrower valleys, but not for this particular curved section of the Inn Valley. Rucker (2003) claims that functions 4.6 and 4.7 are used for practical reasons. One challenge in adapting the method is that Rucker (2003) used only selected scans in a day to determine the weighting factor. However, the goal here is to use all the PPI scans to calculate the weighting factor. The proposed fit only works at certain times of the day.

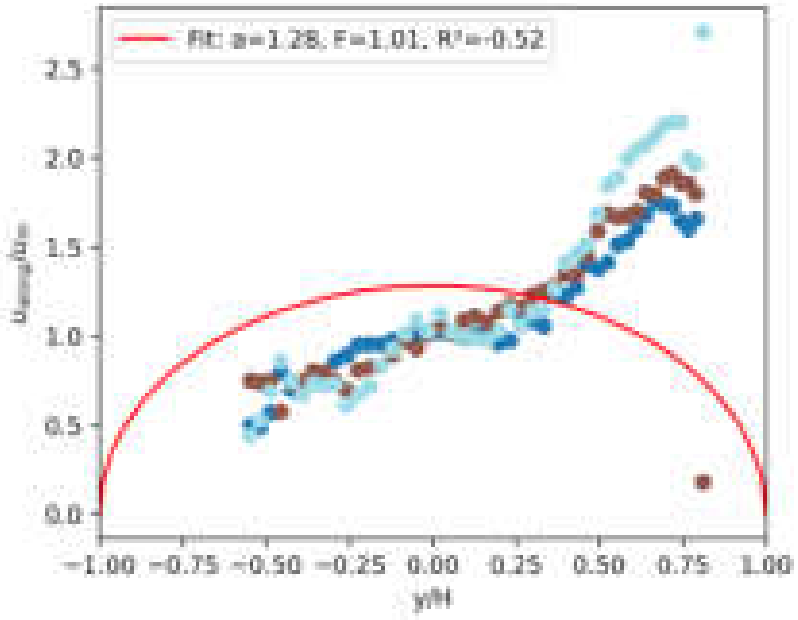

Figure 4.10.: Example of a weighting factor calculation with erroneous fit following the method by Rucker (2003). Three 8° plane position indicator (PPI) scans in down-valley direction on 20 September 2024 at 0306–0347 UTC are shown. Along-valley wind (u_{along}) normalized by the wind speed at the center (u_{m}) as a function of the normalized distance from the valley center (y/H). Each scatter plot color shows one of the three PPI scans. The red line is the least square fit of the data with Equation 4.6.

4.3.3.2. Combination of methods by Rucker (2003) and Clements et al. (1989)

Since the fit function proposed by Rucker (2003) does not work well, a more general parabolic function is tested. The approach is all the same as in the previously described method of Rucker (2003), with the only difference being the choice of function to be fitted. The parabolic function

$$\frac{u_{\text{along}}(y)}{u_{\text{m}}} = A + B \cdot \left(\frac{y}{H}\right)^2 \tag{4.8}$$

is chosen, following the approach by Clements et al. (1989). u_{along} is the along-valley wind component as a function of distance from the valley axis y, u_m is u_{along} at the center of

the valley, H is the valley half-width, and A and B are the parameters to be fitted in a least-squares fit. The weighting factor is then defined as

$$F = A + \frac{B}{3}. \tag{4.9}$$

The combination of the method by Rucker (2003) and the parabolic function proposed by Clements et al. (1989) will hereafter be called R03/C89. Note that R03/C89 does not follow the full approach of Clements et al. (1989), but instead uses only the parabolic Equation 4.8 they propose. The implementation of the original method of Clements et al. (1989) is presented in the following subsubsection 4.3.3.3.

An example for the same time period as shown using the original method of Rucker (2003), but now fitted with Equation 4.8 is shown in Figure 4.11. However, R03/C89 still does not fulfill the requirements, as it likewise assumes a wind profile with a maximum at the valley center. This assumption limits its applicability, since in many cases the maximum within the cross-section is not observed at the center.

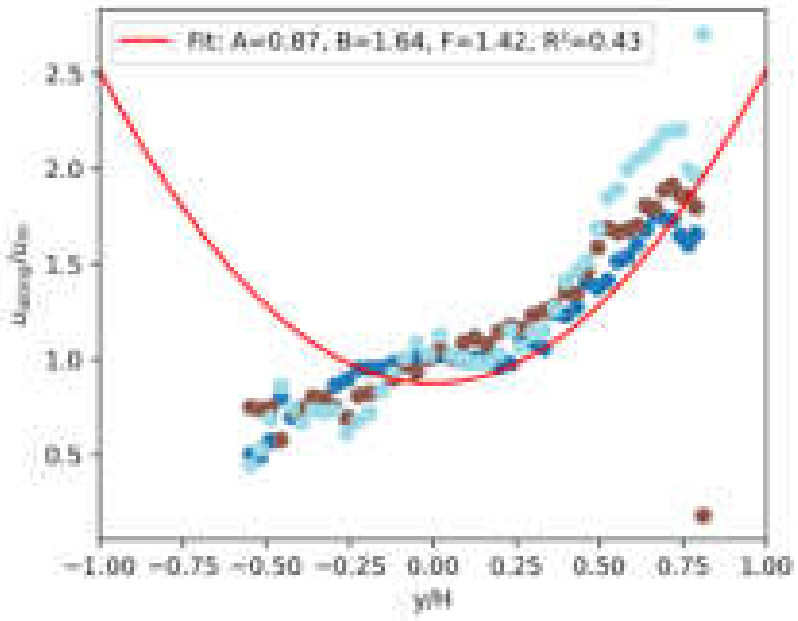

Figure 4.11.: Same as in Figure 4.10 but with the fitted function (4.8) by Clements et al. (1989) instead.

4.3.3.3. Original Clements et al. (1989) method

An implementation of the original Clements et al. (1989) method is also tested. Clements et al. (1989) had a slightly different approach than Rucker (2003). Instead of averaging over several range gates, they chose one range gate, which in their case corresponded to the location of the balloon site. For the purpose of this study, range gate 110 is chosen, which is at a horizontal distance from Kolsass of 4324 m at 3° and 4287 m at 8° elevation. During the measurement nights, Clements et al. (1989) did PPI scans in up-valley and down-valley direction in 0.4° elevation increments between 0.5° and 12.1°. All these scans were used to

calculate the weighting factor. In contrast, this study did not have such a scan pattern, as PPI scans are available in 5° increments starting at 3°. For accurate results it is best to use low elevation scans to minimize the error from calculating the horizontal wind speed and also to reach a far enough horizontal distance away from the lidar.

Since the goal of Clements et al. (1989) was to observe the nighttime drainage flow, they utilized the scans between 0000 and 0600 local time and computed the mean. With the present data, the method of Clements et al. (1989) has to be adapted to work with fewer elevation angles and thus with fewer scans. A time frame with constant up-valley flow is established to test the adapted method, selecting 1400–2000 UTC on 20 September. Initially, the method is tested using the lowest three available elevations, but it is found that for the test day of interest, 13° is not consistent across the valley width (see Figure 4.12a) and has to be excluded for the calculation of F. This leaves only the scans at 3° and 8° elevation. Figure 4.12b shows the least-square fit with parabolic Equation 4.8 applied to the normalized data. Following the same procedure as Clements et al. (1989), the weighting factor F is given by 4.9, which in this case yields $F = 0.64$. While this may seem reasonable, it is challenging to find similar time periods on other days, that make a calculation of F possible with this method.

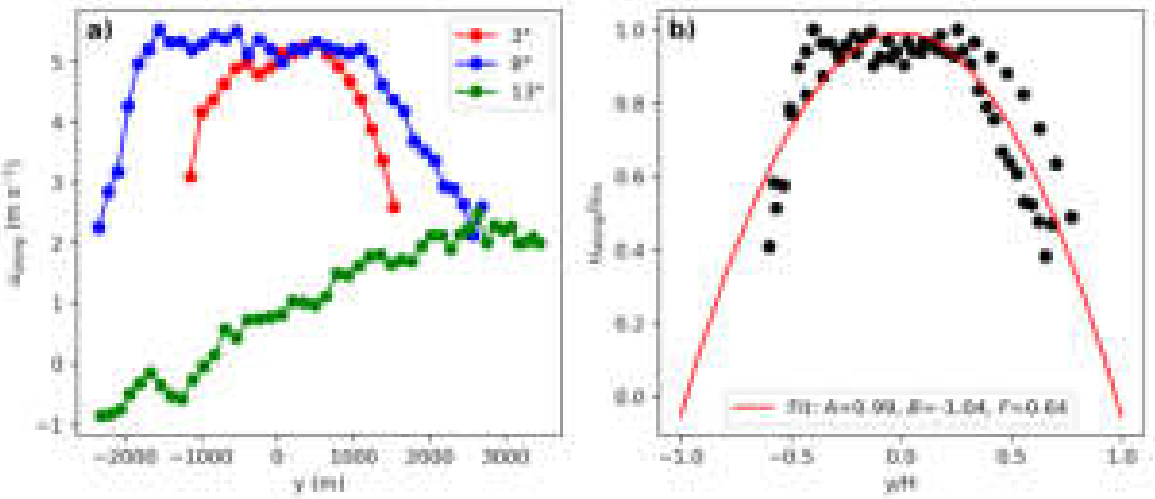

Figure 4.12.: a) Along-valley wind speed at three heights (3°, 8°, 13° elevation) as a function of distance from the valley axis on 20 September 2024 averaged between 1400 and 2000 UTC in up-valley direction. b) Same as a) but with only the lower two heights (3° and 8° elevation) included and normalized axes. The solid line is the least square fit of the data with the function (4.8).

The method originally proposed by Clements et al. (1989) only works on selected hours on selected days. For many hours of the day, the fit struggles to adequately display the cross-valley structure of the along-valley wind (see example in Figure 4.13). While Clements et al. (1989) were interested in only a specific time period of the day, this study aims at looking at the full diurnal cycle of the VVF. Therefore, it would be desirable to compute a weighting factor from data from the entire day. However, due to the limitations mentioned above, it is difficult to generalize the method for this study. Applying the method of Clements et al. (1989) with three elevation angles demonstrates that, in practice, a height-dependent

weighting factor is needed to properly account for the cross-valley variation of along-valley wind speed at different heights (Figure 4.12a and Figure 4.13a). Although such refinement would be desirable, a more detailed investigation was beyond the scope of this study.

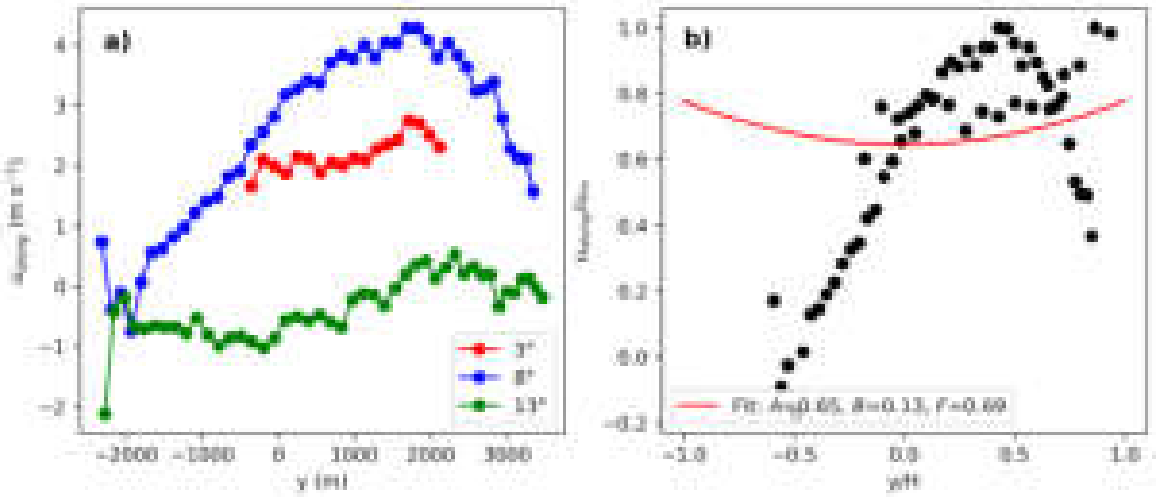

Figure 4.13.: Same as Figure 4.12 but for 21 September 1400–2000 UTC in down-valley direction.

4.3.3.4. Extension of existing methods

Current methods by Rucker (2003) and Clements et al. (1989) do not satisfy the requirements for this study. The main challenges encountered are:

1. Parabolic fits often fail to adequately represent the observed data.
2. The maximum wind speed is frequently displaced from the valley center.

After testing several versions and combination of methods, it was decided to extend previously described methods. PPI scans at 8° are processed in the same way as described in subsubsection 4.3.3.1, resulting in normalized along-valley wind speed as a function of the normalized distance from the valley axis.

Challenge 1 is addressed by moving away from an approach with data being fitted on functions. Instead, three PPI scans at a time are binned into 0.1 y/H units, and the median for each bin is calculated. This gives an average representation of the conditions across the valley width during a 40 min time period while removing isolated outliers. Since the PPI scans do not cover the entire width of the valley, the binned medians are interpolated linearly towards the edge of the valley with the assumption of $u_{\text{along}} = 0\,\text{m s}^{-1}$ at the valley side wall. Cross-sections with more than 50% missing values are excluded from the analysis.

To address issue 2, an alternative to defining the weighting factor via a parabolic fit is needed. This alternative should account for the fact that the highest wind speed is often not observed at the center of the valley. Since the along-valley RHI scans are at the center, it remains necessary to know how the center relates to the mean wind speed across the entire cross-section. Previous methods relied on using the maximum in the cross-section;

however, since the Inn Valley is curved in this section, the maximum wind speed is often not at the center. A more generalized method is to calculate the ratio between the wind speed at the center (u_{center}) and the average wind speed across the cross-section ($\bar{u}$):

$$F = \frac{\bar{u}}{u_{\text{center}}}. \tag{4.10}$$

The medians of the bins are averaged to obtain an average normalized wind speed across the valley cross-section ($\bar{u}$). The wind speed at the center (u_{center}) is defined as the average of the two central bins. This newly proposed method is called "bin method" hereafter. An example of three binned PPI scans and the interpolation towards the valley side walls is shown in Figure 4.14.

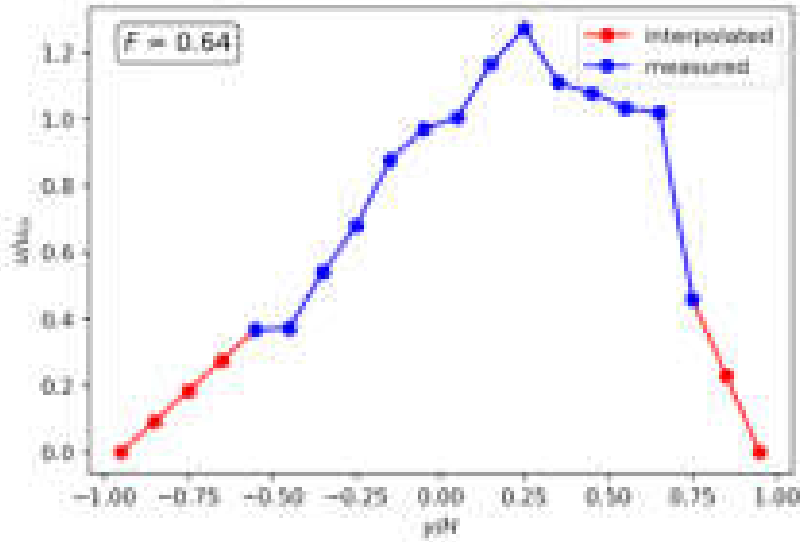

Figure 4.14.: Example weighting factor calculation for three 8° plane position indicator (PPI) scans in down-valley direction on 19 September 2024 at 1001–1041 UTC. Medians of the binned along-valley wind (u_{along}) normalized by the wind speed at the center (u_{m}) as a function of the normalized distance from the valley center (y/H). The wind is interpolated towards the side walls with the assumption of zero wind speed at the wall. The resulting weighting factor F is the ratio between the average over the cross-section and the wind speed at the center (average of two central bins).

Three PPI scans in one direction (up-valley/down-valley) are combined, resulting in a weighting factor for each direction approximately every ≈ 40 minutes, unless a profile was excluded due to too many missing values, as mentioned above. The daily average weighting factor is computed for both directions on the case study days. Although there are cases in which the wind speed at the center exceeds the mean across the section ($F > 0$), or the wind speed at the center has a different sign than the cross-sectional average ($F < 0$), these do not represent the average situation. Therefore, daily averages are calculated both including and excluding profiles with $F > 1$ and $F < 0$, as shown in Table 4.2. Ideally, a time- and space-dependent weighting factor would be used instead of a constant weighting factor, but this is outside the scope of this study. Therefore, a constant weighting factor of 0.67

is used, which is the average over the four case study days, including both up-valley and down-valley directions and excluding profiles with $F > 1$ and $F < 0$.

Table 4.2.: Values of weighting factors F and F_{0-1} for up-valley and down-valley direction, including standard deviation over different dates (bin method).

Date	**Direction**	F	$\mathbf{0 < F < 1}$
19 Sep	Up-valley	0.67 ± 0.25	0.67 ± 0.14
19 Sep	Down-valley	0.59 ± 0.25	0.56 ± 0.21
20 Sep	Up-valley	0.64 ± 0.16	0.64 ± 0.16
20 Sep	Down-valley	0.71 ± 0.20	0.68 ± 0.18
21 Sep	Up-valley	0.68 ± 0.11	0.68 ± 0.18
21 Sep	Down-valley	1.12 ± 0.77	0.71 ± 0.18
22 Sep	Up-valley	0.79 ± 0.23	0.72 ± 0.10
22 Sep	Down-valley	0.93 ± 0.42	0.70 ± 0.12
∅		0.77 ± 0.40	0.67 ± 0.16

4.3.3.5. Discussion on weighting factor estimation

The bin method has its limitations in the Inn Valley. Since the valley is rather broad, it is difficult to capture the flattening of the flow towards the valley sidewalls. In most cases, only about 75% of the valley atmosphere is sampled.

Previously developed methods relied on the idea that the maximum wind speed occurs at the center of the valley. This assumption does not always hold in this section of the Inn Valley. Because the valley is curved in the section around Kolsass, the flow is expected to be affected. As a result, the maximum wind speed is often not in the center of the valley, but rather towards the northern valley side down-valley from the lidar and to the southern side up-valley from the lidar. The adapted method presented here explicitly takes into account the possibility that the maximum wind speed may not be in the center.

Furthermore, the bin method does not seem to work equally well for all times of the day and for all days. On some days, it is possible to find a quite decent parabolic curve with a flattening of the wind profiles towards the edges. Whereas at other times, no such structure is visible, and the distribution of wind speeds seems random. This poses a challenge for defining a general weighting factor, since the number of usable fits per day varies a lot. It is also obvious from the data that there is no single weighting factor that can adequately represent all hours on all days, since this is a flow dependent factor.

4.3.3.6. Diurnal variations of the weighting factor

The estimation of the weighting factor is challenging, as it is neither constant from day to day nor within a single day. In Figure 4.15 an example of the diurnal variations of F on 21 September is shown for the R03/C89) method, as well as for the bin method. The diurnal variations for the other three days are not discussed in detail here but are shown in Appendix A. The R03/C89 method and bin method result in similar weighting factors for

some of the periods, e.g., during the night in up-valley direction. However, large differences between up-valley and down-valley estimates arise for the R03/C89 method during the night. In comparison, the bin method provides no estimate for the same time period in down-valley direction, which is likely due to profiles being excluded in the process because of too many missing values in the cross-section.

In general, the bin method provides results with less variation throughout the day than the R03/C89 method. An exception to this can be seen at 0200 UTC (Figure 4.15). Here, the bin method shows a weighting factor of almost 3 in down-valley direction. Examination of the PPI scan at the time reveals that the flow was highly asymmetric (not shown). Radial velocities were 6 m s^{-1} at the northern side wall, 1–2 m s^{-1} at the center of the valley and 0 m s^{-1} at the southern side wall, therefore leading to a large weighting factor.

An advantage of the bin method is that it can be applied to valleys where the maximum wind speed does not occur at the valley center. However, important limitations remain, as the weighting factor is likely to vary in both time and space. Ideally, the weighting factor would be estimated continuously (e.g., on an hourly basis) and, where possible, for multiple heights within the valley. Determining such a robust, time- and space-dependent weighting factor is beyond the scope of this study. Within the LIVAVERT(EX)^2 project, efforts to estimate the weighting factor will therefore continue.

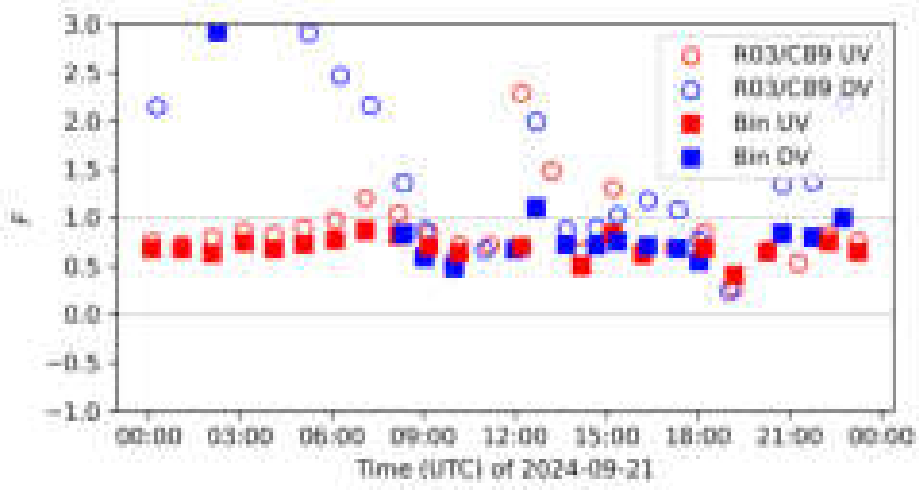

Figure 4.15.: Diurnal variation of the weighting factor F on 21 September 2024 for up-valley (UV) and down-valley (DV) direction calculated with two different methods; combination of Rucker (2003) and Clements et al. (1989) (R03/C89), and extension of method including binning (bin). For detailed explanation of weighting factor calculation see above. The same figures for the other three days of the case study period can be found in Appendix A.

4.3.4. Valley volume flux for AIRflows and LES

The VVF is not only computed for the ground-based DWL but also for four transects with the airborne DWL AIRflows, as well as for two LES runs with the ICON model. Both AIRflows and LES provide wind profiles across the entire cross-section, unlike the ground-based DWL, which only provides profiles from RHIs at the center. Consequently, no weighting

factor is necessary because the non-homogeneity is already accounted for by the knowledge of the wind field across the entire cross-section. A representative wind profile is obtained by computing the mean along-valley wind speed at each height from all the wind speeds across the cross-section (Henne et al., 2004). The VVF retrieved from AIRflows measurements can be used to validate the VVF retrieved from ground-based data. As scanning the entire valley width was not possible with the ground-based lidar, the flow had to be interpolated towards the valley side walls for the computation of the weighting factor (see subsection 4.3.3). The computation of the VVF with the airborne DWL contains wind information from the entire cross-section, making the comparison to the VVF derived with a weighting factor especially valuable (subsection 6.2.1).

4.3.5. Computation of valley volume flux divergence

Understanding whether the valley atmosphere experiences net subsidence or ascent requires an estimate of the divergence of the VVF across the study segment. Here, the portion of the valley between the two cross-sections East and West is treated as a control volume. If there are no other contributions from outside the control volume, any difference between the VVF at these two cross-sections must be balanced by vertical air movement through the upper boundary of this volume. This provides a practical way to infer vertical motion from horizontal flux measurements, given that direct observations of subsidence are not available.

A theoretical budget calculation for the valley segment can be established such that

$$\Phi_{\text{East}} - \Phi_{\text{West}} = \Delta\Phi = \Phi_{\uparrow\downarrow}. \tag{4.11}$$

It is assumed that with the VVF at two cross-sections (Φ_{West}, Φ_{East}), an indirect measurement of the vertical movement $\Phi_{\uparrow\downarrow}$ through the top of the valley volume is possible. Tributaries also need to be taken into account, since they can enhance or reduce the volume flux in the valley (Zängl, 2004). However, it is not possible to estimate the effect of tributaries with the available data. In numerical simulations of the Inn Valley, Deidda (2023) found that the VVF in the small tributaries is often one order of magnitude smaller than in the main valley, while larger tributaries can increase or reduce the VVF in the main valley by up to two thirds. The tributaries near the measurement site are rather small. Since the entrances to larger tributaries such as the Achen Valley and Ziller Valley are about 15–18 km from the lidar, they are unlikely to affect the differences between cross-section East and West, which are only 8 km apart.

Based on the differences, theoretical calculations can be done for the necessary compensating subsidence. The vertical velocity is found as

$$w = \frac{\Phi_{\uparrow\downarrow}}{A}, \tag{4.12}$$

where A is the area of the "lid" of the volume of the valley segment. The area at the top of the valley segment is estimated to be around $A = 90\,\text{km}^2$.

4.3.6. Uncertainty estimation

Uncertainties in the estimation of the VVF arise from several causes. The largest uncertainties are the wind speed estimation itself and the weighting factor. Other factors contributing to uncertainty are the assumption of the wind being primarily in along-valley direction, and the assumption of no (or small) vertical velocity.

The VVF is defined as in Equation 4.2. The uncertainty of the VVF Φ regarding the weighting factor F is defined as

$$\sigma_{\Phi,F} = \sigma_F \cdot J, \tag{4.13}$$

where $J = \int_0^D u_{\text{along}}(z)\, W(z)\, \mathrm{d}z$ and $\sigma_F = 0.16$ is the uncertainty regarding F (Table 4.2). The uncertainty of Φ regarding u_{along} is defined as

$$\sigma_{\Phi,u} = F \cdot \sigma_u \cdot I, \tag{4.14}$$

where $I = \int_0^D W(z)\, \mathrm{d}z$ and $\sigma_u = 0.5\,\mathrm{m\ s^{-1}}$ is the estimated uncertainty regarding the along-valley wind speed measurement. The total uncertainty at each time step is found as

$$\sigma_\Phi = \sqrt{\sigma_{\Phi,F}^2 + \sigma_{\Phi,u}^2}. \tag{4.15}$$

The uncertainty at each time step and for each of the cross-sections can be seen as shading in the example for 22 September in Figure 4.16. The uncertainty of the VVF at each time step is around 25% on average, unless the VVF is nearing zero, in which case it is larger.

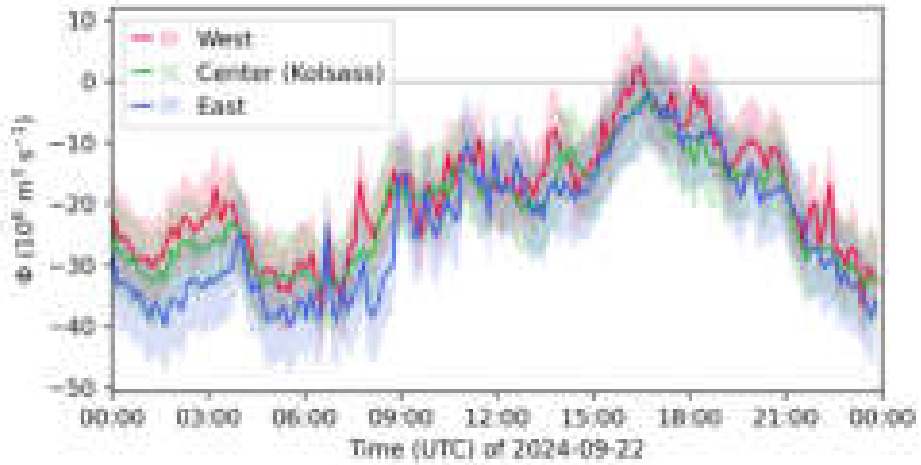

Figure 4.16.: Valley volume flux (Φ) from a ground-based Doppler wind lidar at three cross-sections (see Figure 4.6) on 22 September 2024. The shading shows the uncertainty at each timestep.

5. Synoptic conditions

In this chapter, the procedure for selecting the four-day case study period is presented. Then, the synoptic and meteorological conditions during these four days are analyzed.

5.1. Selection of synoptically undisturbed days

The methodology for selecting synoptically undisturbed days from the geopotential height field was adapted from Lehner et al. (2019), the key difference being the use of the newer ERA5 dataset instead of the older ECMWF Reanalysis - Interim (ERA-interim) dataset. The analysis was done for the same observational site, Kolsass. The selection criterion is based on horizontal gradients of geopotential height, specifically $|\Delta Z/\Delta x| \leq 4 \times 10^{-5}$ and $|\Delta Z/\Delta y| \leq 4 \times 10^{-5}$ at 0000 and 1200 UTC of the day and at 0000 UTC of the following day. The north-south gradient was calculated between 48°N, 12°E and 46.5°N, 12°E, and the west-east gradient between 47.25°N, 11.25°E and 47.25°N, 12.75°E. When the criterion is applied to all time steps (12-hourly), only 12.2% of time steps remain. The distribution of the geopotential gradients can be seen in Figure 5.1.

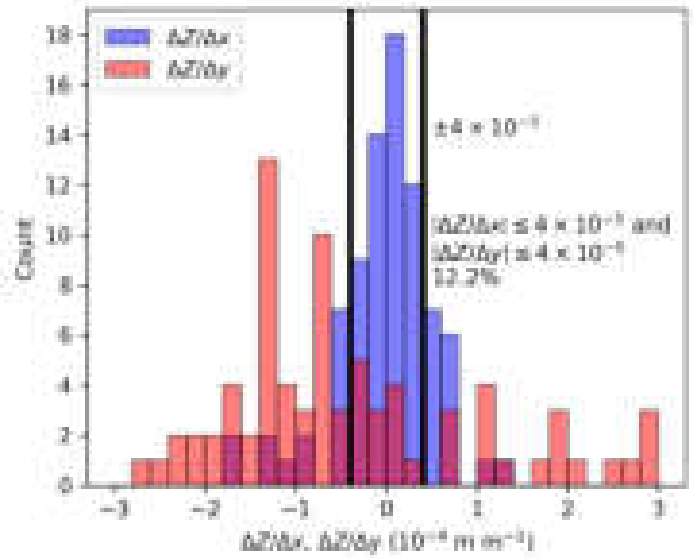

Figure 5.1.: Distribution of time steps meeting the geopotential criterion $|\Delta Z/\Delta x| \leq 4 \times 10^{-5}$ and $|\Delta Z/\Delta y| \leq 4 \times 10^{-5}$. Note this does not take into account the order of the time steps and if the criterion is met at 0000 UTC and 1200 UTC of a day and at 0000 UTC of the following day. Figure inspired by Lehner et al. (2019), their Figure 1.

Based on the requirement that the geopotential criterion be met at 0000 UTC, 1200 UTC, and 1200 UTC of the following day, only two days satisfy it: 20 and 21 September 2024. If the threshold were slightly relaxed to 5×10^{-5} 18.3% of the data points are still included (not shown). 22 September would almost meet the conditions, but the 1200 UTC time step is still outside the limit.

However, it was decided to include 22 September, since an analysis of consecutive days is interesting and the rest of the measurement period was far from being undisturbed. The main analysis is thus focused on these three days. Another day, 19 September, is also included because, although it is not synoptically undisturbed, multiple along-valley and cross-valley flights with the AIRflows airborne DWL system were conducted in the Inn Valley, specifically around the ground-based observational site in Kolsass. This allows for a comparison and evaluation of the proposed method. In addition to airborne data, daytime LES runs with the ICON model are also available for 19 September, which is an additional reason to include the day in the analysis.

Formally, Lehner et al. (2019) also include a clear-sky criterion for their identification of synoptically undisturbed days. Since the days were already significantly reduced by the geopotential gradient criterion and since the identification of clear-sky days was outside of the scope of this work, it was decided not to implement a second criterion. For reference, the daily sunshine duration for the four chosen days from the automatic weather station run by Geosphere Austria at Innsbruck University, 18 km from Kolsass, can be found in Table 5.1. From this it becomes evident that the chosen days were dominantly sunny, with 20 September being the day with the least sunshine hours with 6.1 hours. A more in depth analysis of the cloud cover conditions of the four days can be found in section 5.2. The conditions during the four-day case study period 19–22 September are described below. The VVF analysis in chapter 6 focuses on these four days.

Table 5.1.: Daily total sunshine hours at the weather station Innsbruck University.

Date	Sunshine hours
19 Sep	8.3
20 Sep	6.1
21 Sep	8.9
22 Sep	9.1

5.2. Conditions during the four-day case study period

Four days are chosen as a case study period for the VVF analysis. Below, the large-scale synoptic flow, as well as the flow across the Alps and the weather conditions in the valley during the case study period will be described.

The case study period covers the days immediately following a heavy rainfall event that occurred from 13 to 16 September 2024. This event caused widespread flooding in Eastern Austria as well as parts of Czechia, Slovakia, Poland, Romania, and Hungary. The heavy rainfall resulted from a rare synoptic setup: a cut-off low with a highly active precipitation

zone was trapped for several days over Central Europe by two blocking ridges (Maskell, 2024).

The evolution of the synoptic conditions from 19 to 22 September 2024 can be seen in the 500 hPa geopotential height and surface pressure (Figure 5.2), 700 hPa wind (Figure 5.4), and 700 hPa temperature and relative humidity (Figure 5.3). By 19 September 2024, a well-defined high-pressure system extended throughout the troposphere from the North Sea and Scotland across southern Scandinavia to western Russia (Figure 5.2a). Opposing this, an upper-level low sat over the central Mediterranean, though it had little surface expression. On the northern edge of this system, a trough with its own upper-level low-pressure core—first visible at 300 hPa, later also at 500 hPa—moved westward over the day. This system traveled from the Czech Republic through the Rhine-Main region to Luxembourg. It was a classic cold-core upper-level low, rich in cold air aloft, again without a corresponding surface signal. In the Alpine region, winds above ridge level were southeasterly in the morning, shifting to southerly by evening. South of the Alps strong easterly winds prevail (Figure 5.3a). On 20 September, the upper level low was now above Brittany and the surface high in the north merged with another high over Greenland (Figure 5.2b). The flow south of the Alps weakened but remained easterly, while the southerly to southeasterly flow across the Alps and above the measurement site weakened aswell (Figure 5.3b). By 21 September, the northern high had shifted eastward, placing Central Europe between that system (now over Eastern Europe) and an upper-level cyclone near Brittany (Figure 5.2c). This setup drew warm air northward from the south and southwest. The southerly flow across the Alps strengthened compared to the previous day (Figure 5.3c). On 22 September, a trough northeast of Iceland began moving south. At the same time, geopotential heights dropped over Western Europe due to an eastward-moving upper-level low over the Bay of Biscay (Figure 5.2d). As a result, the Alpine flow turned southwesterly in response to the approaching low-pressure system (Figure 5.3d).

The daily minimum and maximum 2 m temperatures at the weather station in Kolsass during the four case study days are shown in Table 5.2. Minima and maxima of temperatures increase during the four-day period.

Table 5.2.: Daily minimum and maximum 2 m temperature at the weather station in Kolsass. The station is operated by the University of Innsbruck as part of the i-Box network (Rotach et al., 2017).

Date	T_{min} (°C)	T_{max} (°C)
19 Sep	4.8	20.6
20 Sep	5.1	21.1
21 Sep	7.0	23.0
22 Sep	6.9	24.1

The daily radiosoundings at 0300 UTC at Innsbruck Airport (not shown) reveal a surface inversion on all four mornings. On 19 September the inversion is rather weak, whereas on the following three mornings it is pronounced and reaches a height of 1.2 km ASL. The radiosoundings also show indications of a cloud layer at 4 km ASL on 21 and 22 September.

In general the air mass south is more humid than the air mass north of the main Alpine crest on the first three days (see Figures 5.4a–c). On 22 September the humidity gradient is

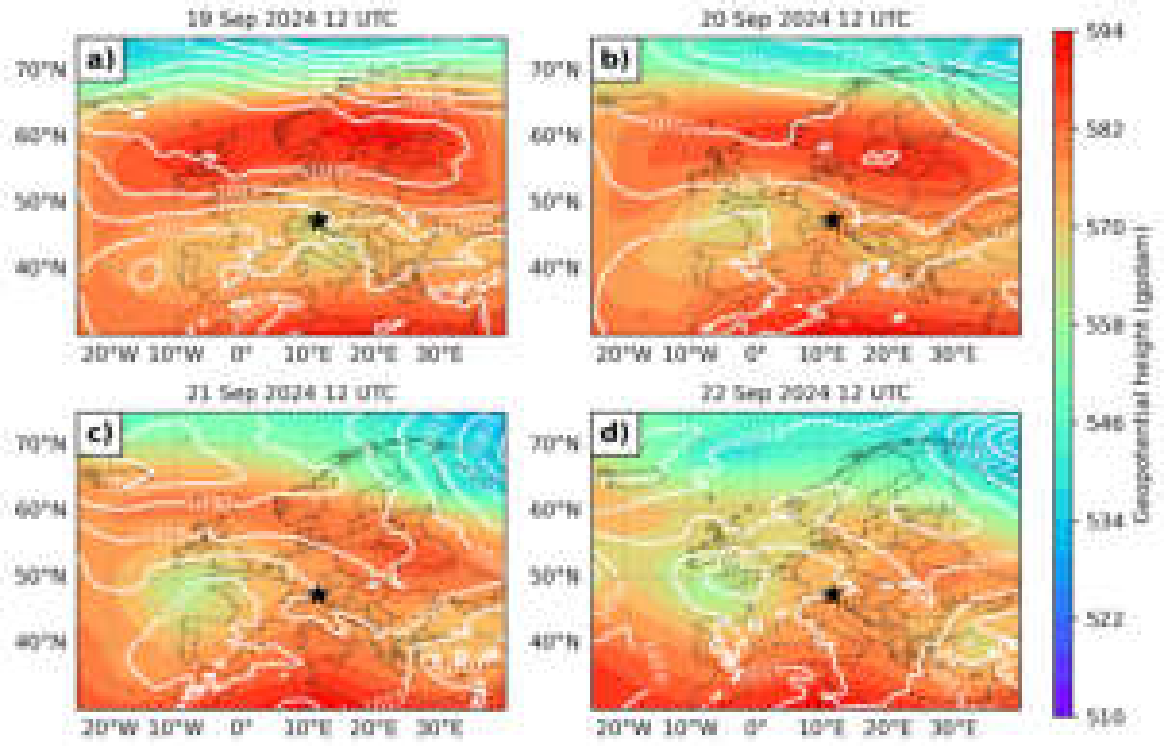

Figure 5.2.: ERA5 data for the time period 19 to 22 September 2024. Each plot is showing the conditions at 12 UTC on a) 19 September, b) 20 September, c) 21 September, and d) 22 September. The colored shading shows the geopotential height at 500 hPa. The white contours show mean sea level pressure with a spacing of 5 hPa. The black lines are national borders. The location of the measurement site is marked with a black star.

more east-west oriented with more humid air to the west (see Figure 5.4d). There was no strong temperature gradient across the Alps at 700 hPa in north-south direction during the four days (Figure 5.4).

Cloudiness in the Inn Valley during the period was generally relatively low (see Table 5.1 for daily sunshine hours). The following descriptions of the cloud conditions in the Inn Valley are based on satellite products (not shown; section 3.4). On 19 September, the skies were mostly clear. Some convective clouds developed above the ridges and were partially also advected above the measurement site during the afternoon. During the night to 20 September, conditions remained mostly clear, with scattered clouds at all levels advected from the east in the second half of the night. On 20 September, low-, mid-, and high-level clouds were advected into the region from the southeast at 8–10 UTC. After a short period of partly clear conditions, clouds at all levels moved into the Inn Valley again in the afternoon. The area had completely overcast conditions after 13 UTC. The night to 21 September was clear. During the afternoon on 21 September, mid-level clouds developed locally. The night to 22 September was mostly clear, while during the day, high-level clouds were advected from the southwest. No significant precipitation was recorded during this period in the Inn valley (not shown).

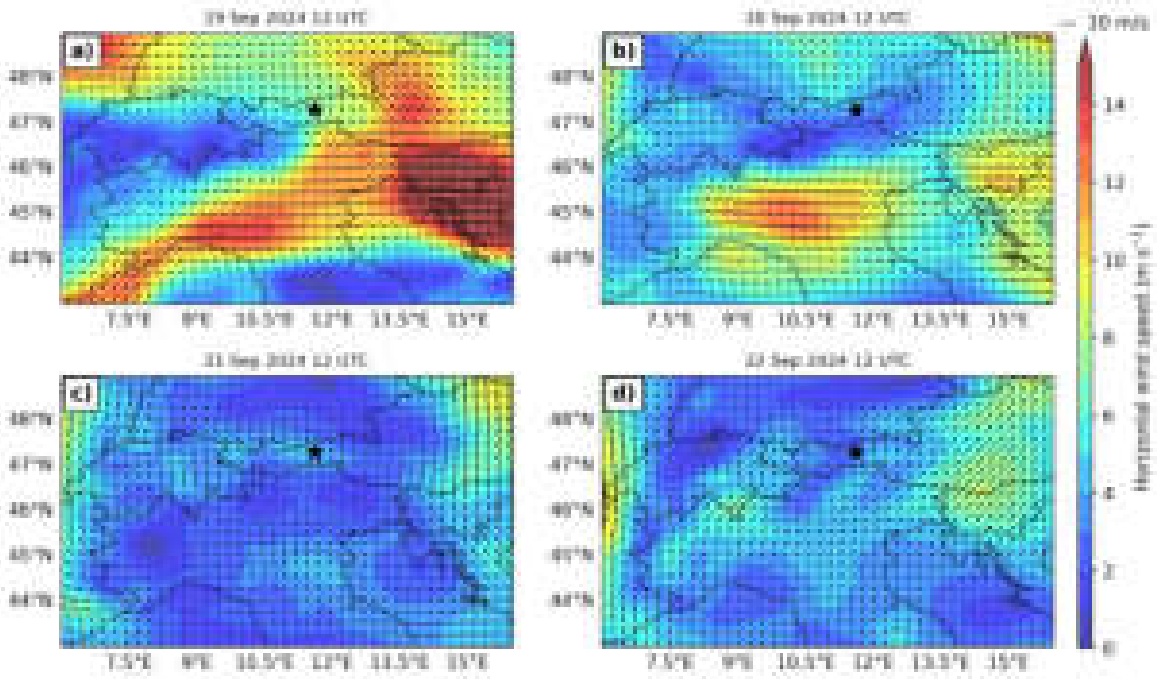

Figure 5.3.: ERA5 data at 700 hPa for the time period 19 to 22 September 2024. Each plot is showing the conditions at 12 UTC on a) 19 September, b) 20 September, c) 21 September d) 22 September. The shading and arrows show the horizontal wind speed. The black lines are national borders. The location of the measurement site is marked with a black star.

During the case study period, south foehn flow was present. During the nights of 19–20, 20–21, and 21–22 September, foehn conditions were observed, although foehn never reached Innsbruck (Figures B.1, B.2, B.3). On 22 September, however, the foehn finally broke through into the Inn Valley, persisting for six hours in the afternoon (Figure B.4).

Sunrise and sunset times during the case study period were approximately at 0500 UTC and 1715 UTC. Solar noon was at 1108 UTC.

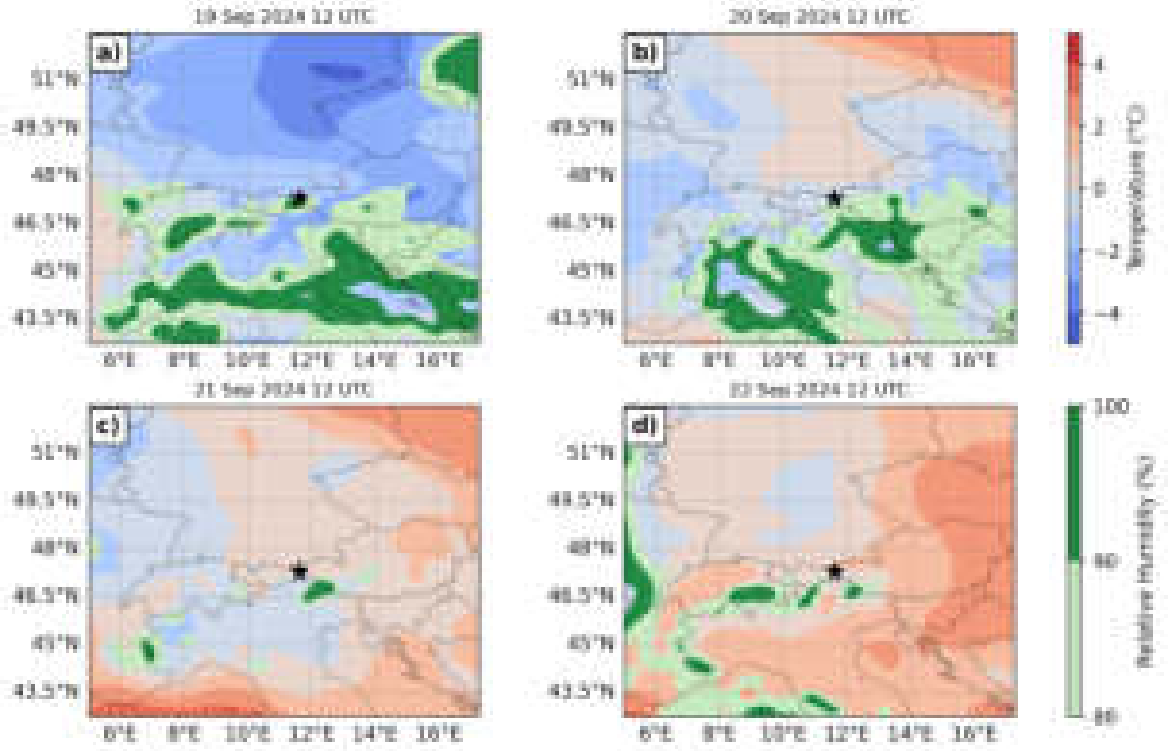

Figure 5.4.: ERA5 data at 700 hPa for the time period 19 to 22 September 2024. Each plot is showing the conditions at 12 UTC on a) 19 September, b) 20 September, c) 21 September d) 22 September. The red to blue shading shows the temperature. The green shading shows relative humidity above 80%. The black lines are national borders. The location of the measurement site is marked with a black star.

6. Valley volume flux estimated from a ground-based Doppler wind lidar

In this chapter the results of the VVF analysis from the ground-based DWL are shown. After an assessment of the whole measurement period, the four days chosen in section 5.1 will be described in more detail. This is followed by theoretical calculations of compensating subsidence as a consequence of VVF divergence along the valley.

6.1. Overview of the entire measurement period

The VVF is calculated for the entire observation period from 10 September to 21 October (Figure 6.1). There is no data from 8–10 October due to an instrument malfunction. This leaves a total of 38 days with data.

In general, frequent changes between up-valley (positive) and down-valley (negative) VVF are observed (Figure 6.1b). The period of the variation varies, as the switch between up-valley and down-valley does not always occur twice-daily, as would be expected on textbook valley wind days (Vergeiner and Dreiseitl, 1987). Periods of consecutive days of only up-valley or only down-valley flux are also observed. The daily maxima of the up-valley VVF are around $20–50 \cdot 10^6$ m^3 s^{-1}. The daily minima of the down-valley VVF have a similar (negative) magnitude. Figure 6.1a shows that the VVF is similar for all three cross-sections most of the time. Occasionally, the VVF at the Center cross-section (lidar location) exhibits a larger magnitude. This difference could be attributed to the fact that the wind profile at cross-section Center is derived differently than the cross-sections West and East, which are derived from the along-valley RHI scans. At cross-section Center the profile is derived from multiple RHI and PPI scans over a time period of approximately 15 min. However, the reasons why occasionally the Center cross-section has a higher VVF than the cross-sections West and East remain unclear.

Figure 6.1b shows that the VVF is vertically consistent. Periods of separated in- and outflow at the same time within the valley are rare.

The VVF difference between the cross-sections East and West (Figure 6.1c) is on average smaller than $10 \cdot 10^6$ m^3 s^{-1} and thus no systematic large VVF divergence is observed in this valley section, confirming expectations. During some rare occasions, the difference reaches a magnitude of more than $20 \cdot 10^6$ m^3 s^{-1}. These large differences often occur on days with synoptically disturbed conditions and frontal passages.

The analysis in the following sections will focus on the case study period from 19–22 September 2024. These four days are not ideal for the investigation of valley winds because they are still influenced by large-scale flow and other phenomena, such as foehn. However,

these days were chosen because the synoptic conditions were the most undisturbed and among the few days without precipitation out of the 38 days of measurements.

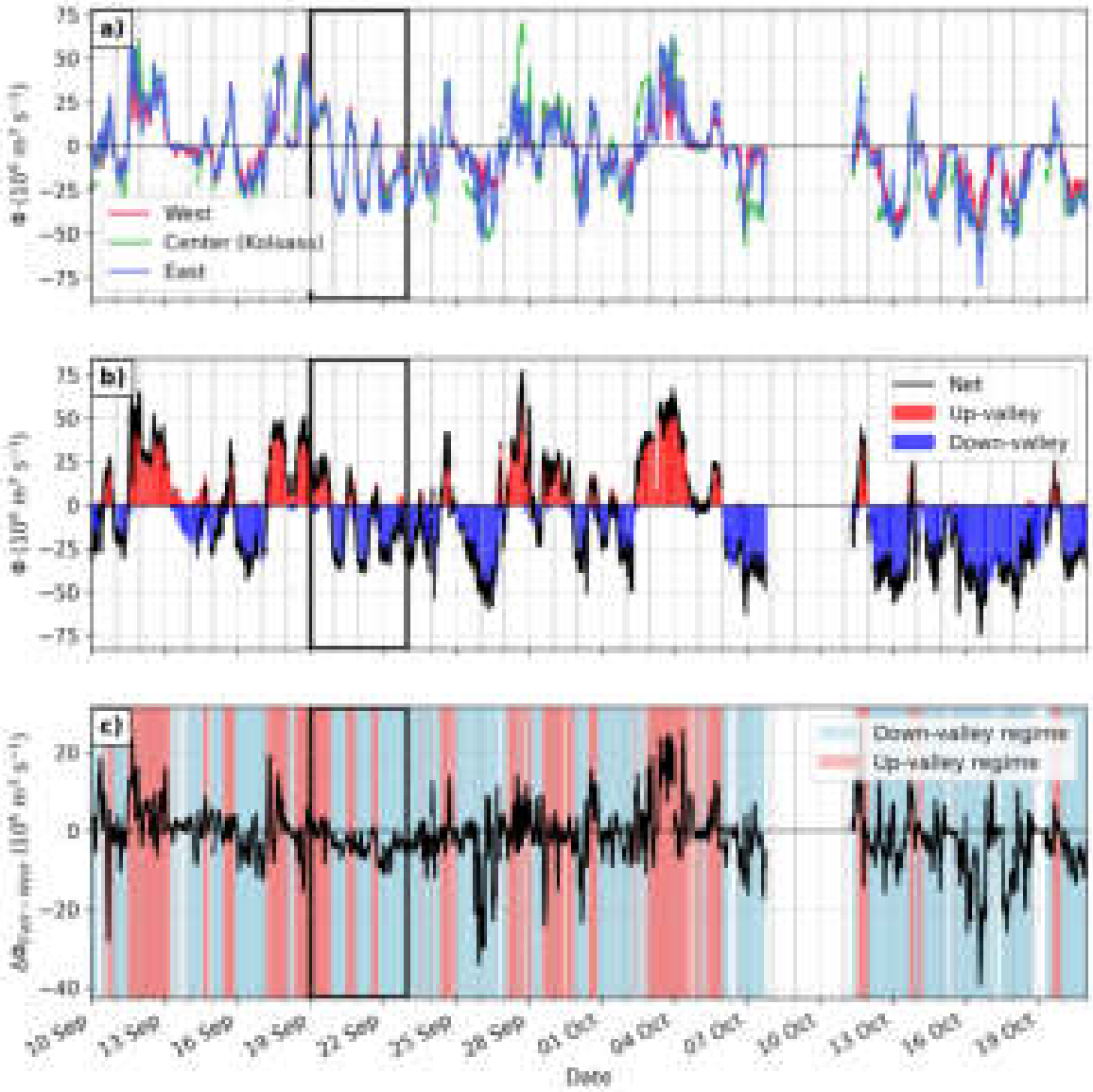

Figure 6.1.: Overview of the measurement period with a moving average of 90 min. a) Valley volume flux (VVF; Φ) for the three cross-sections in Figure 4.6. b) VVF at cross-section Center separated into up-valley (red) and down-valley contributions (blue). The net flux is shown as a black line. Note that the black line in panel b) is the same as the green line in panel a). c) VVF difference (ΔΦ) between cross-section East and cross-section West (black line, East–West). Positive values indicate up-valley direction. The black rectangles indicate the four-day case study period.

6.2. Case study days

The VVF analysis shows that the observation period was dominated by synoptic disturbances, suppressing the development of a "classical" valley wind system on many days. Examining thermally-driven flows in the form of the VVF under undisturbed conditions in the Inn Valley is particularly insightful, as Freytag (1987) showed. For this purpose four case study days are chosen that meet the criteria of synoptically undisturbed conditions to a certain extent (see section 5.1).

6.2.1. 19 September

Flow regime

The first day of the case study period is 19 September 2024. This day was not a classical valley wind day, but is interesting to look at nonetheless, since there are data from four overflights with the airborne DWL AIRflows on this day as well as a LES run with the ICON model (chapter 7).

The wind speed and direction measured by the ground-based DWL (Figure 6.2a and 6.2b) show that there was only a shallow layer of weak down-valley (southwesterly) flow that started to build up around 0200 UTC, reaching its maximum at 0600 UTC with a thickness of 1000 m AVF and disappearing at 1000 UTC. Above this layer, a persistent jet-like up-valley (northeasterly) flow layer with higher wind speeds of up to 8 m s^{-1} is found throughout the night. The up-valley jet at night was likely driven by the easterly synoptic flow (section 5.2). With the erosion of the shallow down-valley flow, the jet sank towards the surface. The up-valley flow occupied the entire depth of the boundary layer after 0900 UTC in Kolsass, as well as in Innsbruck (Figure B.1a,b). There was no convective boundary layer growth and the up-valley flow was rather weak throughout the day. The up-valley wind weakly interacted with the upper-level flow past 1400 UTC. This could be associated with negative vertical wind speeds observed at the same time (see Figure 6.2c). The evening transition from up-valley to down-valley flow started around 1900 UTC at an altitude of 1000 m AVF and progressed to the lower layers until is was complete at 2230 UTC. This behavior is atypical, as a typical evening transition begins close to the surface and grows vertically (Whiteman, 1990). During the night, the flow above ridge level was south-easterly and gradually turned southerly over the course of 19 September.

One feature worth pointing out is the negative vertical wind speeds at 2000 to 3000 m AVF between 1300 and 1400 UTC (Figure 6.2c). This feature likely originates from a small shower that did not reach the ground. During precipitation, the lidar measures the speed of falling droplets, resulting in negative vertical wind speeds. Small-scale convective clouds in the vicinity can be seen on satellite images (not shown). No precipitation was recorded at nearby ground stations, but the Doppler spectrum width and CNR of the DWL show signs of precipitation (not shown).

Volume flux analysis

The up-valley jet results in a positive VVF throughout the night. Although weak down-valley flow close to the surface creates a negative VVF contribution, the overall VVF remains

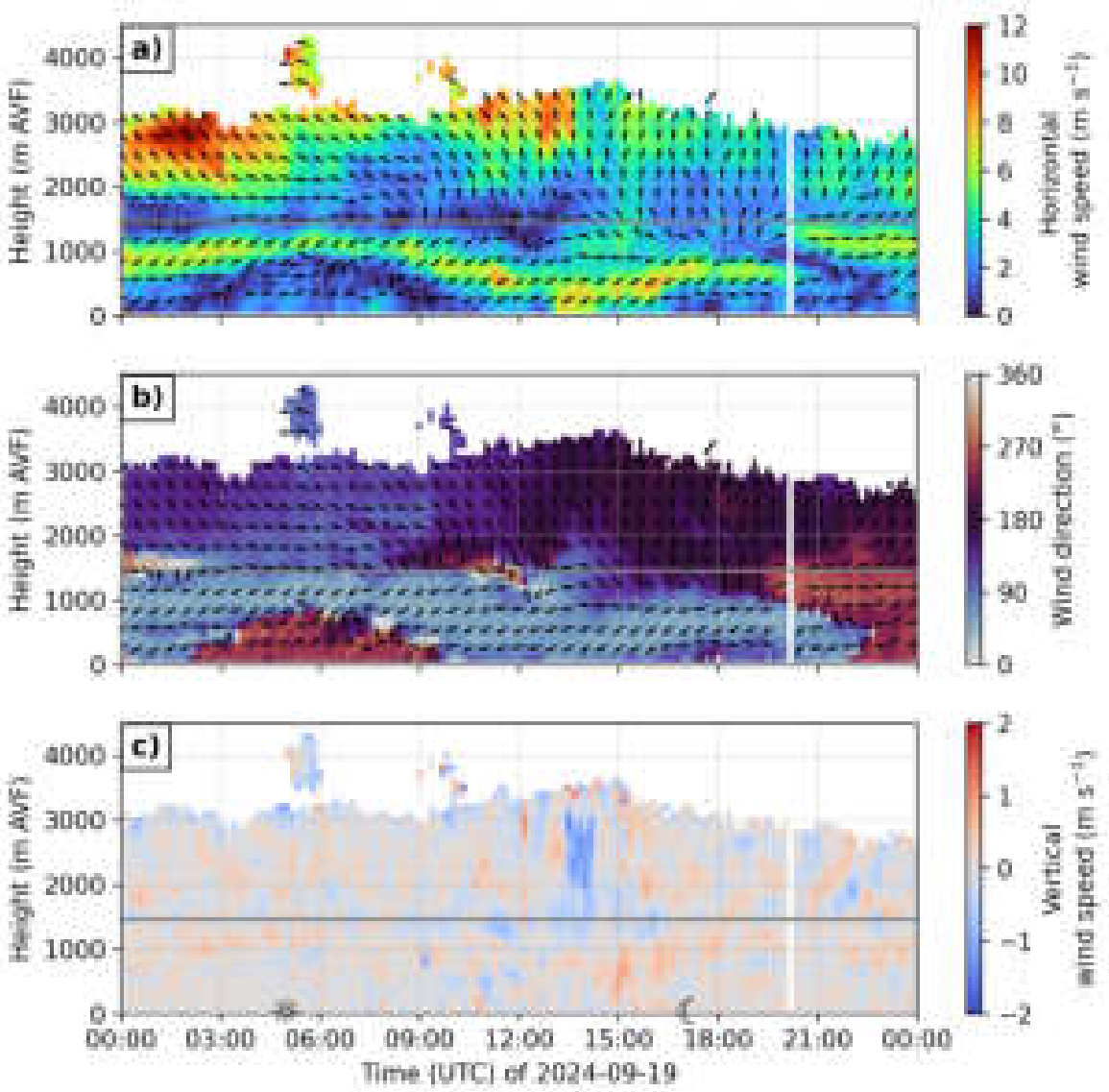

Figure 6.2.: Time height plot of Doppler wind lidar observations for 19 September 2024 showing a) horizontal wind speed, b) wind direction, and c) vertical wind speed. Arrows show the wind direction. The sun and moon symbols indicate the sunrise and sunset times. The gray bold line indicates the average ridge height.

positive from 0000 to 2000 UTC. Consequently, only a single reversal in the sign of the VVF occurred on 19 September. The fluctuations of the VVF were between 10 and 30 $\cdot$ 10^6 m^3 s^{-1}. The minimum VVF during up-valley flow was observed around 0430 UTC and the maximum around 1400 UTC. This timing falls within the typical range for the up-valley maximum in September in the Inn Valley, which is 1300–1700 UTC (Dreiseitl et al., 1980).

The crosses in Figure 6.3a show the VVF obtained from two transects each across Kolsass and Vomp with the airborne DWL AIRflows on the morning of 19 September. The VVF from the airborne observations is computed as described in subsection 4.3.4. The transects across Kolsass correspond to the cross-section Center in Figure 4.6. The transects across Vomp are

≈1 km down-valley from the cross-section East in Figure 4.6. The airborne cross-sections across Vomp are named "East airborne" and compared with the ground-based cross-section East. It is assumed that the wind field is homogeneous in along-valley direction between the cross-section East and Vomp to a first approximation. The difference between ground-based and airborne VVF can be calculated by comparing the closest possible time steps. The time step differences between the corresponding ground-based and airborne measurement are 1–5 min. The difference between ground-based and airborne retrieved VVF varies between 1 and $4 \cdot 10^6$ m^3 s^{-1}. The ground-based VVF is 2–16% larger than the airborne VVF for the four transects, which is well within the approximate 25% uncertainty of the ground-based VVF (subsection 4.3.6). Although only four transects are compared, the small differences provide encouraging evidence for the validity of the presented method.

The mentioned layer of weak down-valley flow in the early morning can also be seen in the separated VVF in Figure 6.3b between 0200 and 1000 UTC. During the early morning, a weak down-valley VVF close to the surface and an up-valley VVF above was observed. The up-valley VVF does not grow during the typical hours of convective boundary layer development during the day. The up-valley VVF is almost constant throughout the day, with the exception of a minimum at noon. Break-down of the up-valley flow starts after sunset, which is typical (Whiteman, 1990).

The difference between the cross-section East, 4 km down-valley from Kolsass, and the cross-section West, 4 km up-valley from Kolsass, exhibits fluctuations in the range of −5 to $10 \cdot 10^6$ m^3 s^{-1} for the majority of the day. The time period from 1330–1500 UTC is an exception to these fluctuations; the difference is smaller (more negative) here. At 1400 UTC, the difference reaches a negative minimum, indicating a VVF divergence along the valley. A VVF divergence is found when the VVF is larger up-valley from the lidar than down-valley from the lidar. The observed VVF divergence could be related to a local downdraft from the shower mentioned above that did not reach the ground. There is agreement between the VVF divergence and the mean vertical wind speed (Figure 6.3c), which could indicate subsidence at the valley-scale above the area. A further explanation could be outflow from the tributaries caused by south foehn, redirected in up-valley direction. A short period of weak south foehn, which did not penetrate the Inn Valley, was observed in the afternoon above Innsbruck (Figure B.1). Outflow from the Weer valley (see "Weerbach" in Figure 3.2) has been observed to be deflected westward during up-valley wind in the Inn Valley (Pfister et al., 2024). Further discussion of the observed episodic VVF divergences can be found in section 6.3.

6.2.2. 20 September

Flow regime

The second day of the case study period, 20 September 2024, follows a more classical valley wind day according to the definition, with a twice-daily reversal of the wind speed (Vergeiner and Dreiseitl, 1987). Conditions were less than ideal with respect to cloudiness in the valley. Clouds at all levels reduced the incoming solar radiation for two hours in the morning (0800–1000 UTC), and for the rest of the day after 1300 UTC (not shown).

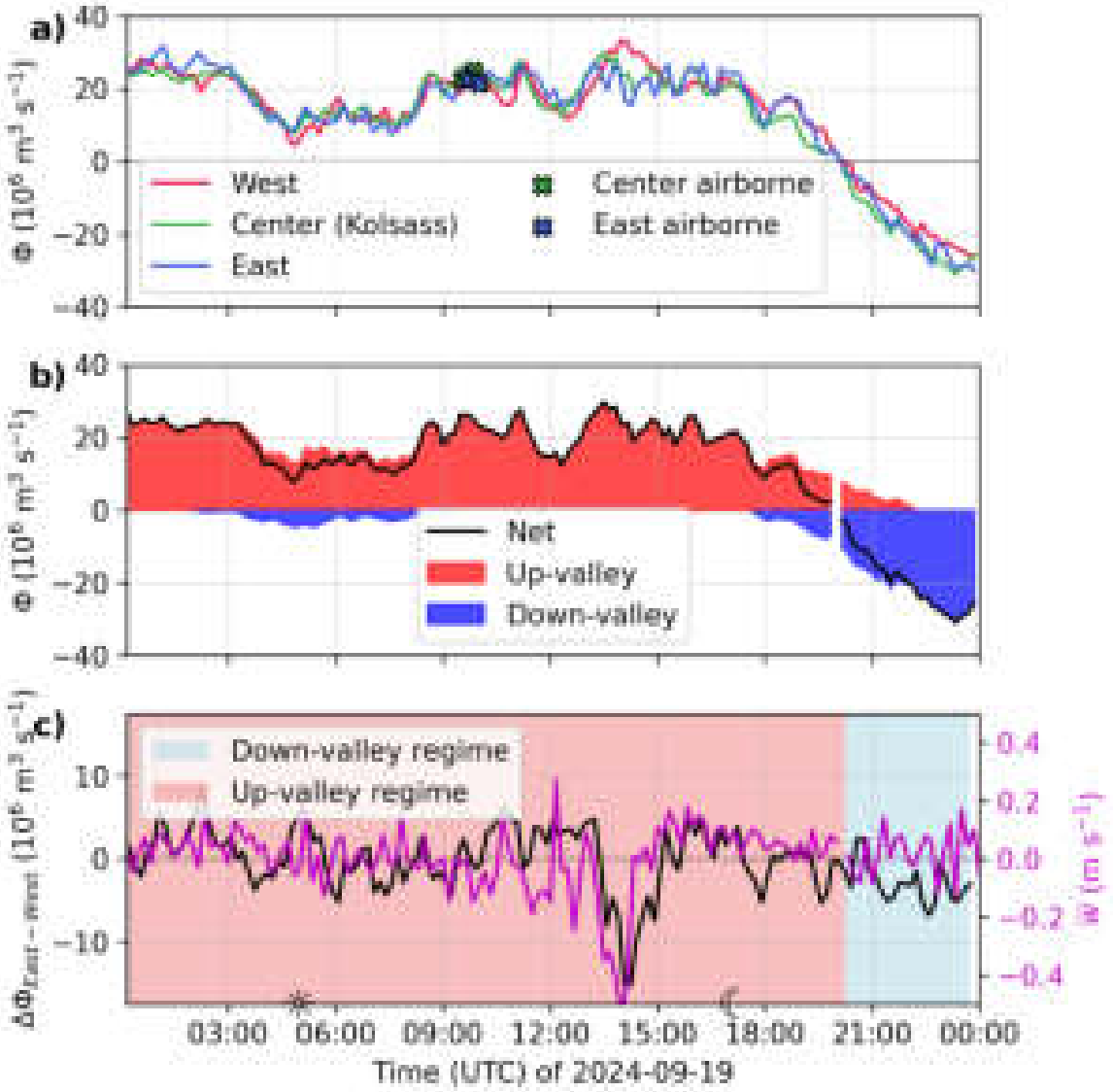

Figure 6.3.: Results for 19 September 2024: a) Valley volume flux (VVF; Φ) for three cross-sections from a ground-based Doppler wind lidar (DWL) and two overflights with an airborne DWL across the Center and East cross-sections each. Note the airborne East cross-section was 1 km further down-valley than the ground-based one. b) VVF at cross-section Center seperated into up-valley (red) and down-valley component (blue). The net flux is shown as a black line. Note that the black line in panel b) is the same as the green line in panel a). c) VVF difference (ΔΦ) between cross-section East and cross-section West (black line, East–West) and average vertical wind speed in the integration layer (up to 1455 m AVF, magenta). Positive (negative) ΔΦ indicates VVF convergence (divergence). Positive values indicate up-valley direction. The sun and moon symbols indicate the sunrise and sunset times. Note the different y-axis scaling compared to the overview Figure 6.1.

Wind speed and direction can be seen in Figure 6.4. A down-valley flow was observed during the night with maximum wind speeds of around 7 m s^{-1} at 1000 m AVF. The down-valley flow reached up to ridge height. At night and in the early morning, the flow above

ridge level was southwesterly. The flow above ridge level weakened during the morning and turned to more southerly direction during noon. The shift from down-valley to up-valley flow occurred at 1200 UTC in Kolsass, and at 1100 UTC in Innsbruck (Figure B.2), which is 1 hour later than the average, but still in the typical range for September (Dreiseitl et al., 1980). The delay can be attributed to clouds reducing the incoming solar radiation between 0800–1000 UTC, which can be seen in the station data from Kolsass (not shown). The shift from down-valley to up-valley flow started at the surface, but the up-valley flow developed its full depth rather quickly.

The up-valley flow layer in the afternoon had a depth of almost 1000 m AVF, which is about 500 m below ridge height. In Innsbruck, the up-valley layer in the afternoon had a depth up to ridge height first, but then the flow close to the surface up to 500 m AVF separated from the flow above (Figure B.2a and b). The strong southerly to southeasterly flow above was likely foehn-related. The foehn strengthened but did not reach the surface. In the afternoon, a period with a clockwise turn of the wind with height was observed; going from northeasterly (up-valley) close to the valley floor to southerly above 2000 m AVF. Around 1500 UTC, the flow at ridge height and up to 2000 m AVF was southeasterly, corresponding to a cross-valley direction. By 1800 UTC, a layer between 1000 and 1500 m AVF began turning to down-valley flow, which is unusual because down-valley wind is typically first observed closer to the surface. On the previous day (19 September), the evening transition had also not started at the surface, even though down-valley wind is typically expected to develop there first (Whiteman, 1990). The full transition was completed by approximately 2200 UTC. In Innsbruck, the first down-valley winds in the evening were only observed at 2100 UTC (Figure B.2a,b), where the transition actually began at the surface. This contrast suggests that the early down-valley winds observed between 1000 and 1500 m AVF in Kolsass may have been deflected foehn winds rather than a typical thermally driven drainage flow.

The vertical wind speed (Figure 6.4c) shows some indications of rising motion around ridge level before sunrise. Throughout the day no strong vertical wind speeds were recorded. Around sunset, there were indications of sinking motion above 3000 m AVF, as well as rising motion around ridge level at night.

Volume flux analysis

An overview of the VVF on 20 September is shown in Figure 6.5. The VVF was negative (down-valley) and similar at all three cross-sections during the night (see Figure 6.5a). The net VVF was positive during a period from 1200 UTC to around 2000 UTC. There were some differences on the order of ~1 hour between the cross sections as to when the transition from up-valley to down-valley flow occurs. The magnitude of the VVF was larger during down-valley flow than during up-valley flow, due to the southwesterly flow above ridge level, as well as south foehn in the upper portion of the valley deflected eastward. Deflected foehn is a common phenomenon in the lower Inn Valley (Gohm and Mayr, 2004; Gohm et al., 2009).

The shift from up-valley to down-valley flow manifested gradually, with the up-valley layer becoming smaller and the down-valley layer becoming increasingly larger during the transition between 1600 and 2200 UTC (see Figure 6.5b). This shift occurred from top to

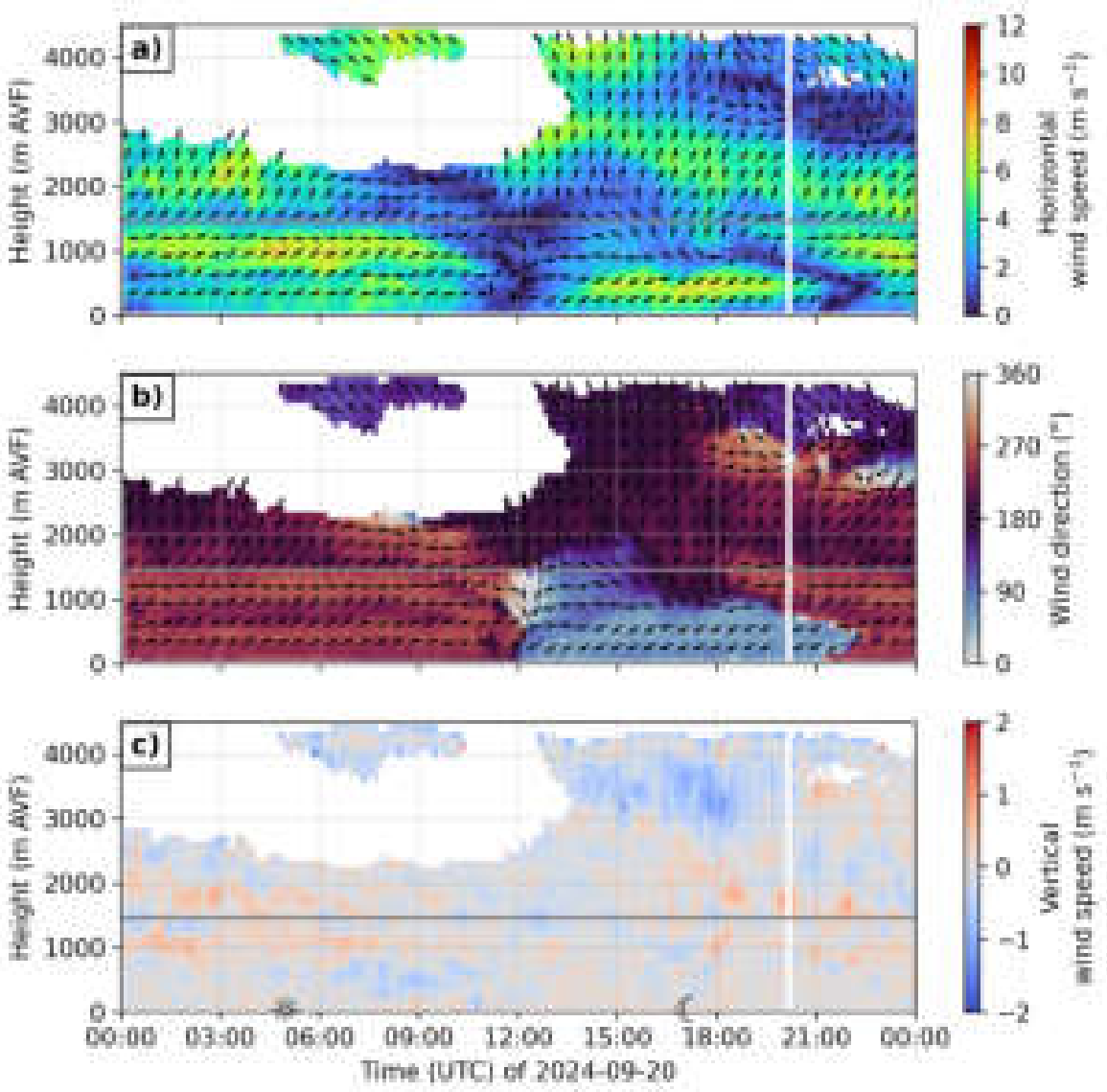

Figure 6.4.: As in Figure 6.2, but for 20 September 2024.

bottom, likely due to synoptic influence. The first down-valley flow in the evening had already occurred one hour before sunset, which is a clear indication that the down-valley VVF was not only thermally driven. The more thermally driven transition began two hours after sunset, when the up-valley VVF also started to weaken.

The difference between the West and East cross-section was negative for most of the day, both during net down-valley and up-valley flow, with values varying between −13 and $3{\cdot}10^6$ m^3 s^{-1}, corresponding to about ±25% of the VVF for most of the day. The magnitude of these regular differences is about the same as that of the average uncertainty of the VVF estimation itself. Negative differences indicate a VVF divergence (see Figure 6.5c). VVF divergence is expected during nighttime, as the down-valley flow from tributaries adds to the VVF in the Inn Valley. In contrast, VVF divergence is somewhat unexpected during up-valley flow, since tributaries are assumed to derive their daytime up-valley flow from the Inn

Valley (Zängl, 2004), which would typically result in VVF convergence there. A noteworthy minimum of less than $-10 \cdot 10^6$ m^3 s^{-1} was observed around 1600 UTC, corresponding to 65% of the VVF at cross-section West. Because the difference between the cross-section East and West is negative, this represents a VVF divergence. The timing of the maximum divergence coincides with a shift in wind direction above 1000 m AVF, suggesting that the divergence may be linked to a spatially heterogeneous change in the upper-level flow. Theoretical estimates of the compensating subsidence associated with such divergences are provided in section 6.3.

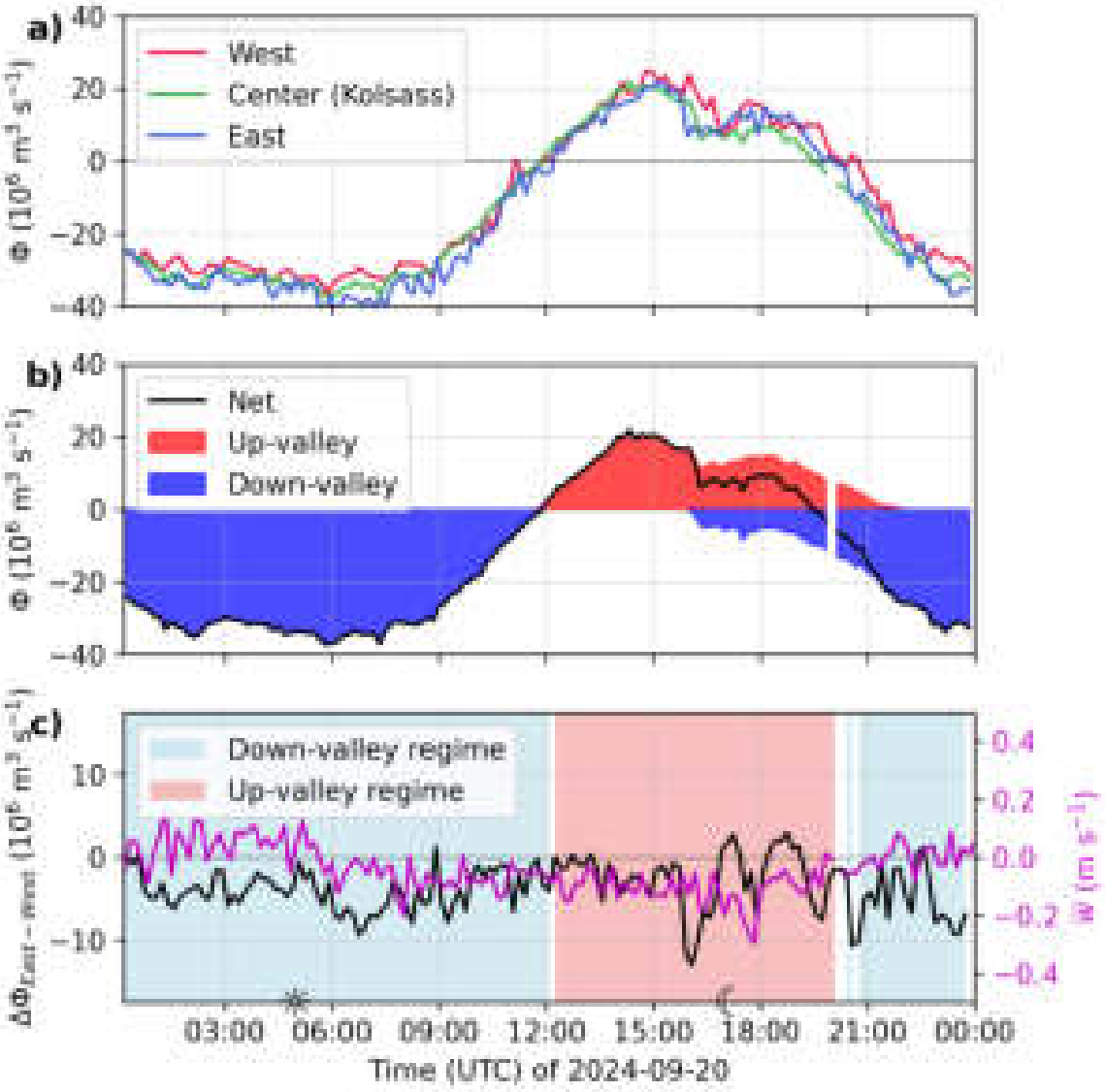

Figure 6.5.: As in Figure 6.3, but for 20 September 2024.

6.2.3. 21 September

Flow regime

On 21 September 2021, a valley-wind system was observed, which was again supported by the upper-level flow during the down-valley phase (Figure 6.6). The nighttime down-valley flow was dominant up to 1200 UTC. In Kolsass, the flow was in southwesterly, down-valley direction from the surface up to 2500 AVF. Maximum wind speeds of around 7–8 m s^{-1} were observed at 1000 m AVF. In Innsbruck, the down-valley flow was only around 500 m deep (Figure B.3a and b). Above the down-valley layer, the foehn from the previous evening lasted until sunrise. After sunrise, the foehn flow above Innsbruck weakened.

During the morning hours, the flow above ridge level was southwesterly, supporting the down-valley flow in the valley. The switch to up-valley flow occurred at 1200 UTC, which is at the same time as on the previous day. The up-valley directed layer during the afternoon was slightly shallower with less than 1000 m depth and lasted shorter than on the previous day. It strengthened during the late afternoon to reach its maximum in the early evening. In Innsbruck, no real convective boundary layer growth was observed and only a very weak up-valley flow developed close to the surface in the afternoon (Figure B.3a).

During the afternoon, the flow above ridge level turned to a more southerly direction and strengthened compared to the morning. At 2000 UTC, the shift to down-valley flow was completed, which is 2 hours earlier than on the previous day. The flow at 1500–2500 m AVF was southwesterly during the evening. Thus, the down-valley winds were not only thermally driven but also dynamically supported. The first signs of down-valley wind in Innsbruck were found at 1930 UTC (Figure B.3a). The build-up of the stable boundary layer was interrupted by a short period of southerlies (likely foehn) almost reaching the ground. After 2100 UTC, the down-valley flow in Innsbruck developed and strengthened subsequently. The foehn winds also regained strength after 2100 UTC above Innsbruck, but did not reach the surface, similar to the previous night.

Rising motion exceeding 1 m s^{-1} was observed during the afternoon at 1500–1900 UTC (Figure 6.6c). First, between 2000 and 3000 m AVF and later between 1000 and 2000 m AVF. Below, some sinking motion on the order of 1 m s^{-1} was also observed. Vertical winds exceeding 2 m s^{-1} were observed in Innsbruck above 800 m AVF (Figure B.3c). This could be related to the interaction of the up-valley flow with the upper-level foehn in the Inn Valley in the late afternoon, leading to rising motion.

Volume flux analysis

The VVF follows a classical wave structure on 21 September, but the magnitude of the down-valley flux is much larger than the magnitude of the up-valley flux. Supported by the large-scale southerly flow, the VVF during nighttime down-valley flow reaches absolute values of $30 - 40 \cdot 10^6$ m^3 s^{-1}, as can be seen in Figure 6.7a. The up-valley VVF layer at cross-section East (Figure 6.7b) reaches a maximum of only $10 \cdot 10^6$ m^3 s^{-1} in the early evening. Since the daytime up-valley flow is shallow and rather weak, the net VVF is rather small during the afternoon, since it is almost compensated by the down-valley directed layer above (Figure 6.7b).

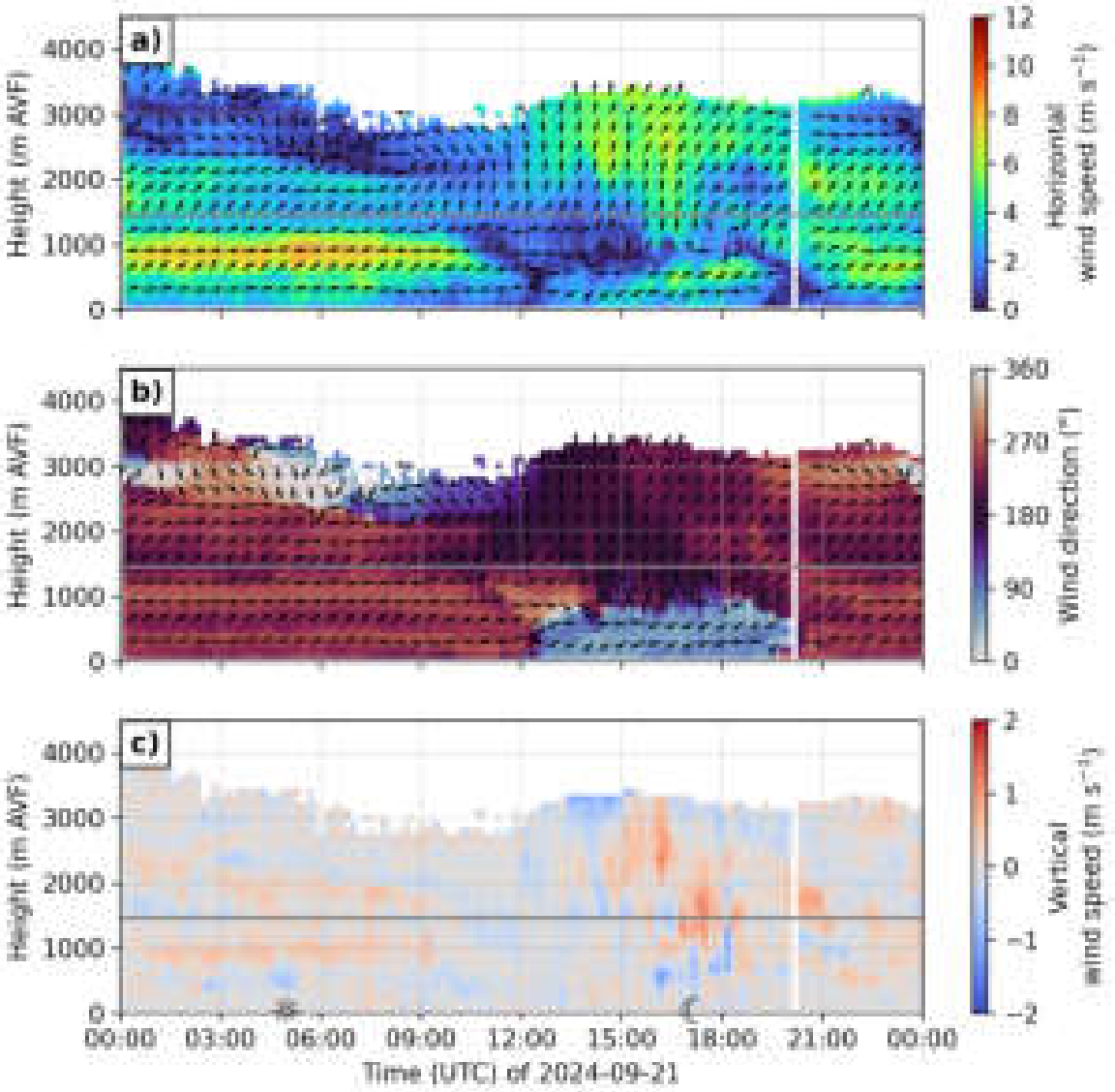

Figure 6.6.: As in Figure 6.2, but for 21 September 2024.

During the down-valley regime, rather strong VVF divergences are observed, especially continuing into the night to 22 September (Figure 6.7c). During the up-valley phase, the differences are smaller, with some minima during the afternoon between 1500 and 1800 UTC that might be linked to some updrafts and downdrafts, which can be seen in the vertical velocity profile in Figure 6.4c. Although VVF divergence generally dominated during nighttime down-valley flow in this four-day period, a noteworthy short-lived episode of VVF convergence (positive difference) was observed at 0200 UTC (Figure 6.7c). Not only in this four-day period, but as previous studies indicate Post and Neff (1986); Freytag (1987), nighttime VVF divergence is typically expected. The observed convergence is therefore unexpected, and no corresponding signal is evident in either the time–height cross-section or the vertical wind speed. Interestingly, VVF at the cross-section Center is not between the values of the cross-section West and East, but rather similar to the VVF at cross-section

West. Since two consecutive timesteps show this maximum in the VVF, it is unlikely that it is just a measurement error (Figure 6.7a). In the PPI scans around 0230 UTC, it is also clearly visible that the wind speed down-valley from the lidar is considerably higher than up-valley from the lidar (not shown). The particular cause for this short-lived event remains unclear. Although this day is disturbed by the large-scale flow and foehn, a diurnal cycle of the valley wind system is still observed in the section around Kolsass.

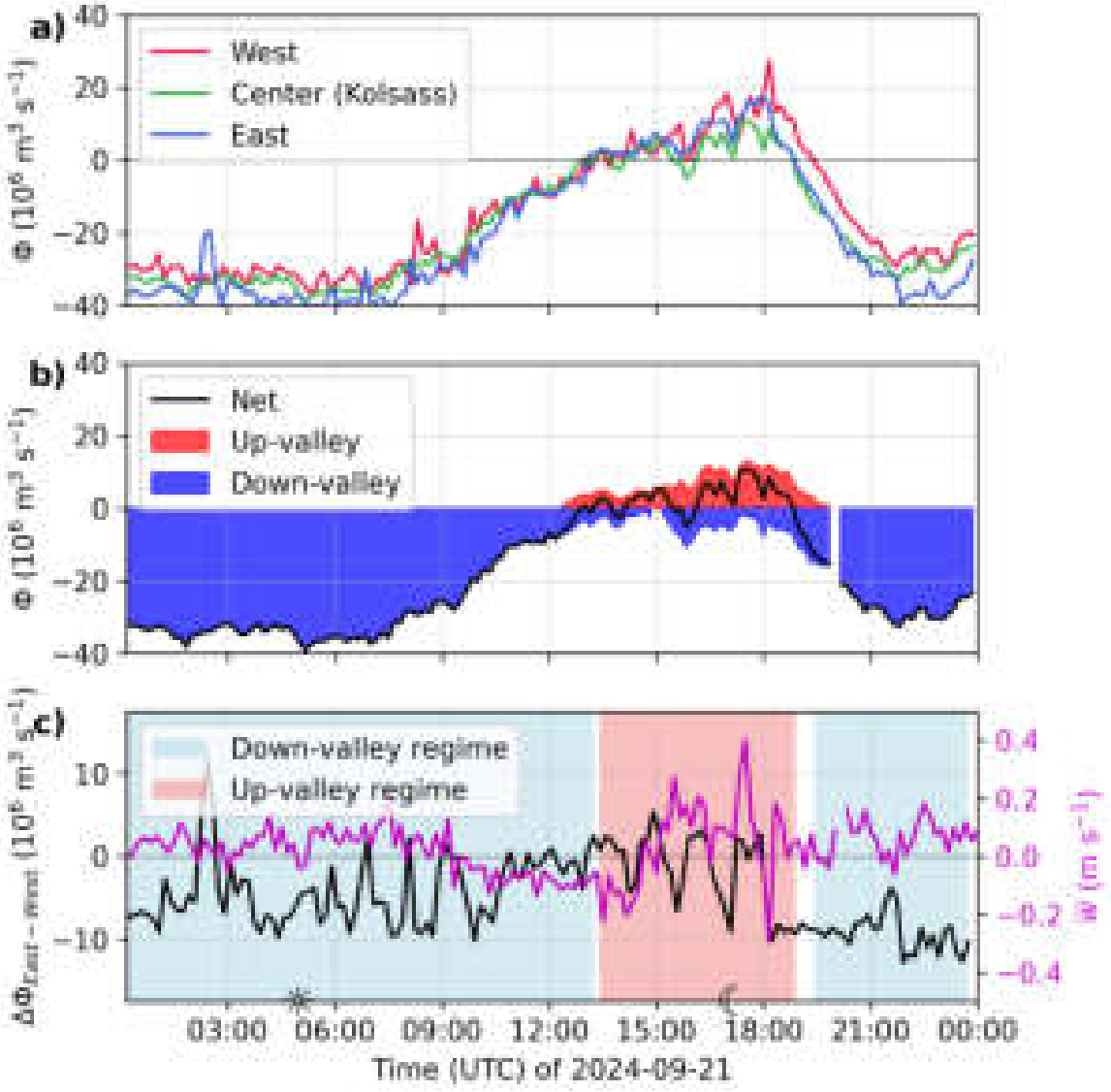

Figure 6.7.: As in Figure 6.3, but for 21 September 2024.

6.2.4. 22 September

Flow regime

The flow on 22 September was dominated by upper-level southwesterly flow in the morning and a south foehn breakthrough in the afternoon. Despite the disturbed conditions caused by the foehn wind, a diurnal cycle of the valley wind system could still be observed close to the surface.

During the night, the entire valley atmosphere up to 2200 m AVF was dominated by westerly to southwesterly, down-valley flow. A down-valley jet formed at night and reached its maximum of 8 m s^{-1} at 1000 m AVF. The jet was still present until 4 hours after sunrise. The flow above the jet was weaker, reaching only 4–5 m s^{-1} . From the lidar data in Innsbruck, it is clear that the observed wind speed maximum at 1000 m AVF had a strong southerly component and was detached from the down-valley flow close to the surface, indicating it was related to foehn flow (Figure B.4a).

A layer with strong vertical shear at upper levels was observed from 0000 UTC with a southwesterly layer up to 2500 m AVF and a layer of weak northerly to northeasterly wind above (Figure 6.8a and b). The sheared layer disappeared after 1200 UTC. The onset of a shallow up-valley directed layer occurred three hours later compared to the previous three days, at around 1500 UTC. The layer of up-valley wind was only about 600-700 m deep and rather weak. The up-valley wind speed maximum of 5 m s^{-1} was observed at 1600–1700 UTC. No up-valley flow was observed in Innsbruck on 22 September (Figure B.4). South foehn with maxima of 11–12 m s^{-1} between 12–17 UTC hindered the development of (north-)easterlies close to the surface.

The flow above the up-valley layer remained southwesterly, thus in down-valley direction. Above the southwesterly layer, there was a layer of stronger westerly winds. The up-valley flow layer lasted until 2200 UTC. Afterwards, the flow in the valley was in down-valley direction again.

The vertical wind speeds in Kolsass did not show pronounced maxima on 22 September (Figure 6.8c). Indications of rising motion were found around ridge level in a two hour period after sunset. On the other hand, vertical motion in the valley exceeding 2 m s^{-1} was observed in Innsbruck at 1200 UTC and around sunset (Figure B.4c). Both these periods of enhanced vertical motions lasted around one hour each. The first period of vertical motion at 1200 UTC coincides with the time where the south foehn first breaks through to the surface. The second period of vertical motion coincides with the time of complex interactions between a foehn interruption (or end) and the initial development of down-valley flow close to the surface.

Volume flux analysis

The net VVF on this day remained negative (= net down-valley) all day, or rather reached almost zero just before sunset (Figure 6.9a and b). However, a diurnal cycle within this negative VVF was observed. Minima of the (negative) VVF were below $-30 \cdot 10^6$ m^3 s^{-1} at night and in the early morning. The maximum (= weakest period) in the down-valley VVF corresponded with the period of strongest up-valley VVF (Figure 6.9b).

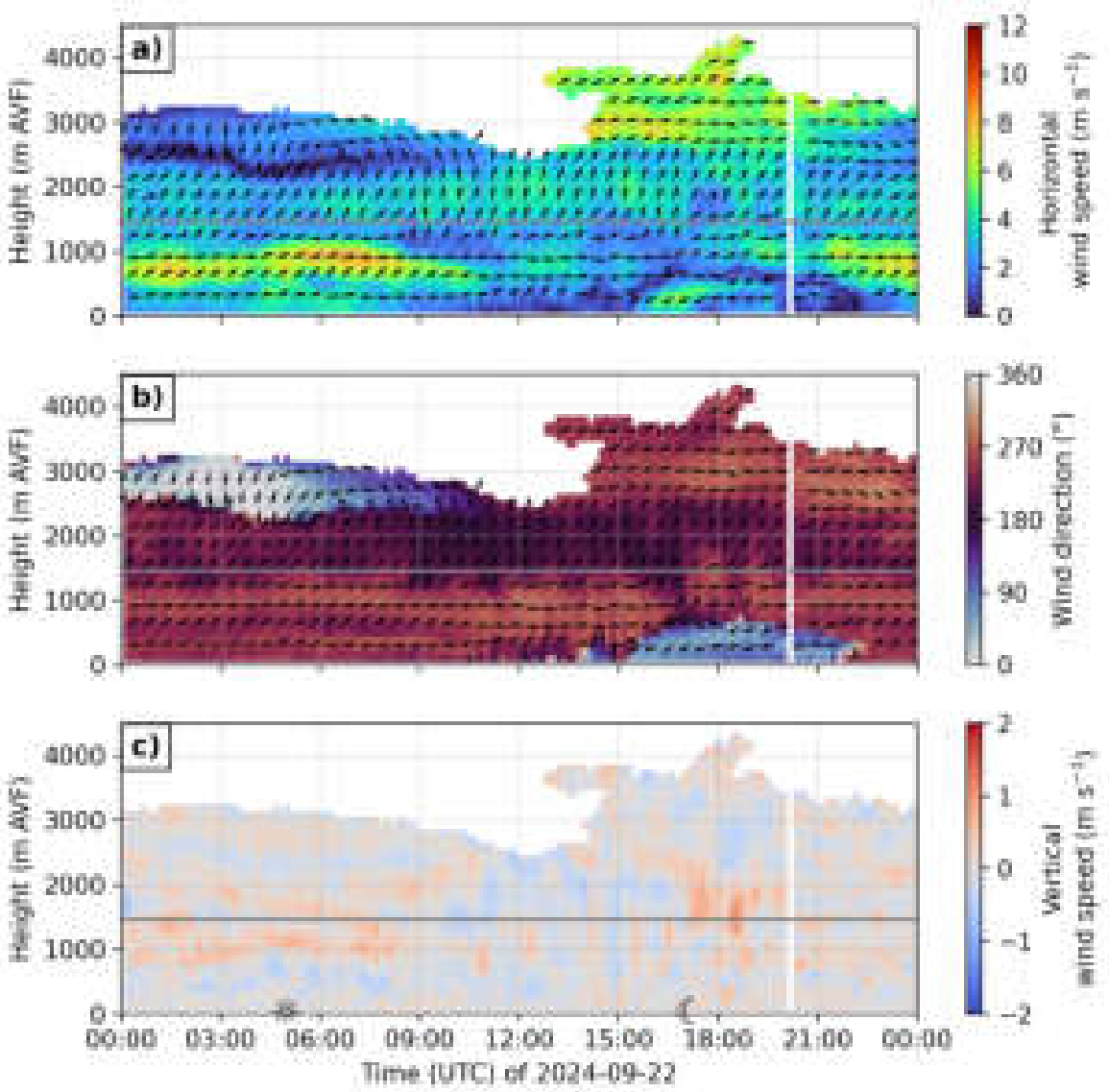

Figure 6.8.: As in Figure 6.2, but for 22 September 2024.

A weak and shallow layer of up-valley flow developed at 1500 UTC. The 600–700 m deep up-valley layer close to the surface in the late afternoon and early evening compensated for the down-valley layer above and reduced the absolute value of the net VVF to almost zero at approximately 1630 UTC (Figure 6.9b). The weak up-valley VVF lasted until 2130. The down-valley VVF gained in strength again after sunset.

During the night, a period of VVF divergence with a difference below $-10 \cdot 10^6$ m^3 s^{-1} was observed between 0130 and 0400 UTC and between 0730 and 0900 UTC during down-valley VVF. The maximum absolute difference observed during this time period was $15 \cdot 10^6$ m^3 s^{-1}, corresponding to 45% of the VVF at the cross-section East at the time. This rather strong VVF divergence could be related to the southerly winds observed in Innsbruck (discussed in Flow regime above) that were deflected into southwesterlies and formed a jet-like structure in the lower Inn Valley. Outflow from the Watten Valley and Weer Valley might also contribute to

the VVF divergence. Their outflow might be increased during southerly flow and potentially also during foehn. Outflow from the Weer Valley has been observed to be deflected eastward during down-valley flow (Pfister et al., 2024). Under south foehn conditions, a weak diurnal cycle of the VVF was still observed, though the up-valley VVF could not develop fully.

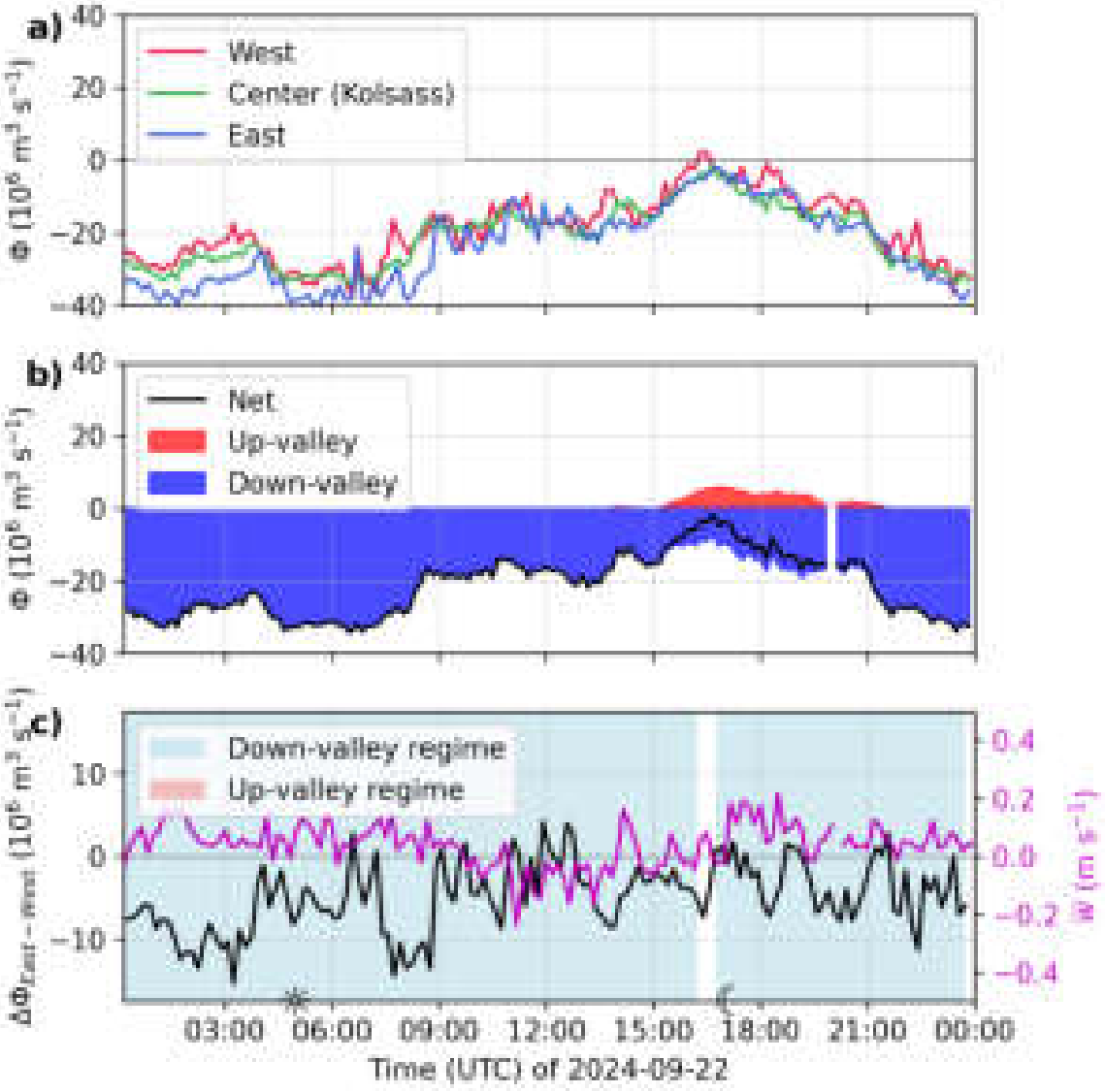

Figure 6.9.: As in Figure 6.3, but for 22 September 2024.

6.3. Implications of flux divergence

The VVF difference between the down-valley location and the up-valley location ($\Delta\Phi$) is calculated following subsection 4.3.5. The hypothesis is that a negative difference will be found at nighttime during down-valley flow (divergence) and a positive difference will be found during the daytime up-valley flow (convergence). The difference during nighttime will

be negative because the VVF at the cross-section further down-valley (East) will be smaller (more negative) than at the cross-section further up-valley. This is because the outflow from the tributary valleys contributes to the VVF in the main valley at night. Respectively, during up-valley flow, the opposite is expected, as tributaries "extract" the air for their up-valley flow from the main valley. See Figure 6.10 for an idealized sketch of this hypothesis.

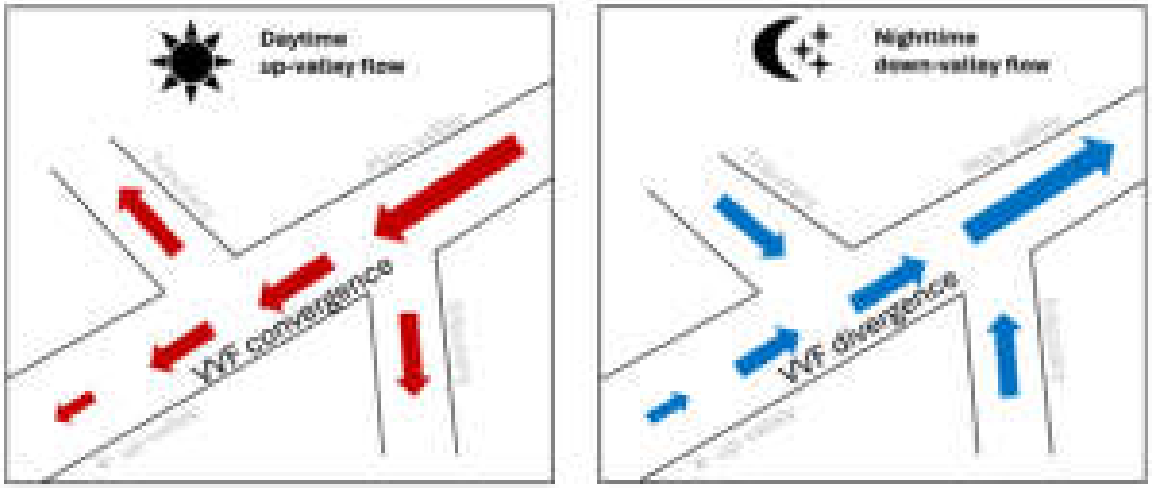

Figure 6.10.: Conceptual sketch of valley volume flux (VVF) convergence/divergence during daytime up-valley flow (left) and nighttime down-valley flow (right). During up-valley flow, air from the main valley is exported into the tributaries, leading to VVF convergence in the main valley. During down-valley flow, tributary valleys contribute to the VVF in the main valley, leading to VVF divergence there.

While VVF divergences were observed frequently during down-valley flow, confirming the hypothesis, no VVF convergences were observed during up-valley flow. Similar studies also did not find VVF convergences during up-valley wind; conversely, they found divergences during up-valley wind (Freytag, 1987; Rucker et al., 2008).

During a few short-lived periods within the four case-study days, divergences in the VVF were detected between the eastern and western cross-sections. The associated compensating subsidence, assuming no contributions from tributaries, was estimated following the approach described in subsection 4.3.5. Theoretical calculations were carried out for the most pronounced events. For example, a VVF difference of $15 \cdot 10^6\,\mathrm{m^3\,s^{-1}}$ during up-valley flow on 19 September (around 1400 UTC) corresponds to an average subsidence of $-0.17\,\mathrm{m\,s^{-1}}$ over the control-volume area. Negative vertical velocity was actually observed at the time of VVF (Figure 6.3c). It remains unclear whether the observation was due to a small shower, as hypothesized in subsection 6.2.1, or due to other processes.

Similarly, a difference of $\Delta\Phi = 13 \cdot 10^6\,\mathrm{m^3\,s^{-1}}$ on 20 September (around 1600 UTC) implies $w \approx -0.14\,\mathrm{m\,s^{-1}}$. Here, no corresponding minimum in the mean vertical velocity was observed (Figure 6.5c). These subsidence values likely represent lower bounds, since the vertical velocity is unlikely to be homogeneous across the valley lid and is expected to be stronger near the valley center. Moreover, in the presence of cross-valley vortices, upward

motion on one sidewall and downward motion on the opposite sidewall may occur (Babić et al., 2021).

During down-valley wind in the night from 21 to 22 September, a period of persistent VVF divergence was observed between 2200 and 0300 UTC (Figure 6.7c and Figure 6.9c). The mean divergence during this interval was $10 \cdot 10^6\,\mathrm{m^3\,s^{-1}}$. Over the five-hour period, this corresponds to an import of approximately 138% of the valley volume. Most imported air is likely to have originated from tributaries, as the average vertical wind speed during the period was positive (Figure 6.7c and Figure 6.9c).

Similar studies have also performed calculations of the necessary subsidence to compensate for along-valley flux divergence. Freytag (1987) found $0.05\,\mathrm{m\,s^{-1}}$ in the Inn Valley while Rucker et al. (2008) found $0.45\,\mathrm{m\,s^{-1}}$ (uncertainty range $0.17–0.49\,\mathrm{m\,s^{-1}}$) in the Wipp Valley. Possible explanations for VVF divergences include valley-scale subsidence compensating for up-valley flow into the tributaries, a pressure-gradient within the valley caused by differential heating, and gravity waves causing supercritical flow (Freytag, 1987; Rucker et al., 2008; Zängl et al., 2001). However, observational confirmation of these mechanisms is still limited. In addition, since the uncertainty of the VVF in this study is estimated to be around 25% on average (subsection 4.3.6), it is unclear whether estimates of compensating subsidence from previous studies based on relatively small divergences are meaningful.

On the other hand, Henne et al. (2004) found that during fair weather summer conditions, an average of three times the valley mass is vertically exported per day in the Mesolcina and Leventina valleys. They find that besides turbulence and large-scale flow, up-slope winds are important drivers of the export. No significant export was observed during the four-day case study period in this study. The conditions were not very favorable for large exports, since daytime up-valley flows were rather weak due to the large-scale flow and south foehn.

6.4. Summary

The combination of DWL profiles and the integrated VVF retrievals offers insights into the dynamics of thermally driven along-valley flow in a section of the Inn Valley. The analysis of four days allows the differentiation between recurring and intermittent features. A recurring feature is up-valley flow during the afternoon. The up-valley VVF is strongest on day 1 of the case study period. The up-valley maximum decreases linearly in strength during the course of the four-day case study period. Down-valley VVF was observed on three of the four days. The down-valley VVF was always larger in magnitude than the up-valley VVF. The first day of the case study period is still influenced by the large-scale easterly flow during the night. In the following days, the influence of southerlies supporting down-valley flow grows, as well as the influence of south foehn above, suppressing the development of strong up-valley flow during daytime. Close to the surface, up-valley winds still develop during the afternoon, but the majority of the valley air remains in down-valley direction by the fourth day of the case study period.

The VVF method allows one to see the magnitude of the along-valley wind components by volume of air easily, especially when separated into up-valley and down-valley components, as shown e.g., in Figure 6.1b. No systematic volume flux divergence during daytime up-valley flow was found, unlike Freytag (1987) and Rucker et al. (2008). The conditions during

the MERKUR (Freytag, 1987) and MAP (Rucker et al., 2008) field campaigns were mostly undisturbed, making them more ideal for valley wind studies. The lack of daytime up-valley VVF divergence during the campaign for this study might be explained by the not fully undisturbed conditions. Not surprisingly, rather large VVF divergences were found during down-valley flow. A possible cause for the divergences is the outflow from the southern tributaries, which was probably not only thermally driven but also enhanced by south foehn.

The analysis could be improved and made more robust by defining more cross-sections. More cross-sections make it possible to see if there is actually a systematic VVF divergence along the valley instead of only comparing two or three cross-sections. An additional DWL placed further down-valley would provide valuable insights into the development of the VVF along the Inn Valley. Additionally, a longer dataset could provide a better understanding of the VVF and the valley wind system under various conditions and seasons.

7. Valley flow in airborne observations and LES

In the following sections, first the evolution of the valley wind in ICON-LES is shown for 19 September (for model setup, see section 3.3). Then, the wind from the model is compared to the measurements with the airborne DWL AIRflows. Finally, the VVF computed from model data is compared to the VVF computed using ground-based and airborne DWLs on 19 and 20 September.

7.1. Evolution of the valley flow in LES

The model allows the study of the temporal evolution of the flow across the entire cross-section. An example of the temporal evolution of the flow at the cross-section in Kolsass is shown in Figure 7.1. On 19 September, the flow in the model shows an atypical diurnal cycle of the valley flow. In the morning, there are already up-valley winds in the valley, as was also seen in observations (subsection 6.2.1). The maximum during the morning (0600–0700 UTC, Figure 7.1a, b) is not at the valley center, but it is shifted towards the northern side of the valley. Throughout the day, the up-valley flow strengthens and peaks at 1500–1600 UTC with a maximum of 9 m s^{-1} in the up-valley flow (Figure 7.1j, k). In the observations, the up-valley flow did not strengthen as much and did not reach more than 7 m s^{-1} at its maximum (Figure 6.2a). The flow above ridge level begins southeasterly and strengthens during the morning until 1200 UTC, after which it weakens and turns more southerly. Observations mostly agree with the flow above ridge level from the model, with the main difference being stronger winds in the observations around 1100–1300 UTC at 3000 m AVF.

7.2. Valley flow structure: airborne observations and LES

To assess the performance of the LES, simulated results are compared with observations from the airborne DWL AIRflows. Figure 7.2 presents a comparison of horizontal wind speed, wind direction, and vertical wind speed along cross-section Center at Kolsass (for location see Figure 4.6).

Overall, observations and simulations agree on the general structure of the horizontal wind. There is northeasterly (up-valley) flow in the lower layer, up to 2000 m ASL in the observations and up to 1500 m ASL in the model. There is a shallow layer of weak southerly to southwesterly winds aloft and southeasterly winds above ridge level. However, several differences emerge regarding the detailed valley flow structure. The model underestimates

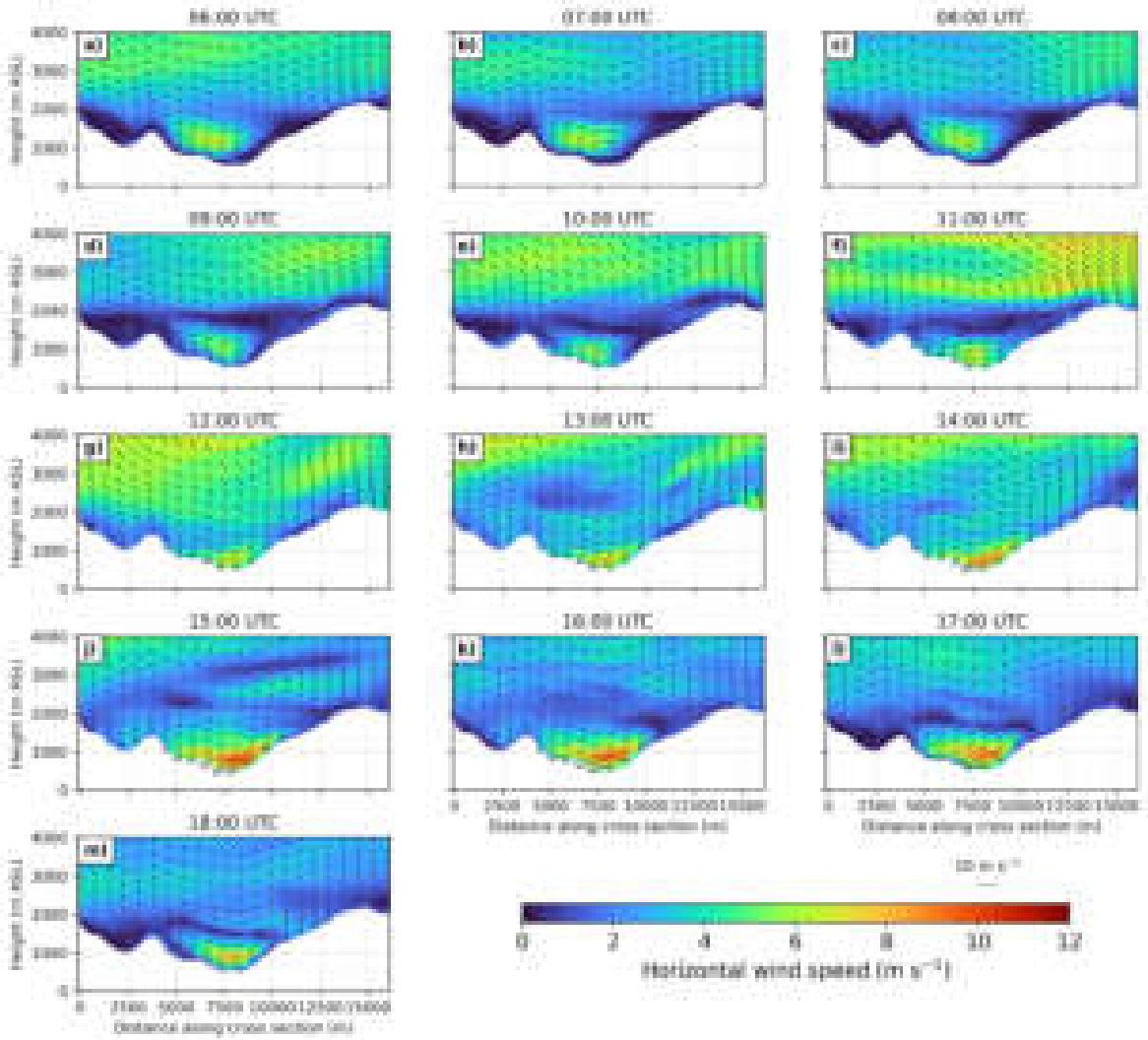

Figure 7.1.: Horizontal wind speed (color shading) with overlaid wind vectors indicating direction at the cross-section Center (Kolsass) looking in down-valley direction on 19 September 2024 from ICON-LES. a)–m) show instantaneous output at an hourly resolution from 0600–1800 UTC.

both the width and magnitude of the valley wind speed maximum. In the simulation, the maximum is located closer to the surface and shifted towards the left (northern) side of the valley, whereas observations indicate a maximum centered at around 1300 m ASL. The model also places the height of the directional shear too low: the change from northeasterly to southwesterly flow occurs at 1600 m ASL in the model, compared to 2000 m ASL in the observations. Above ridge level, the model further overestimates horizontal wind speed by about 2–3 m s^{-1} . In addition, the model produces weak westerlies along the southern valley wall that are absent from the measurements.

Differences are also apparent in the vertical wind speed. The 260 m resolution appears insufficient to resolve the small-scale turbulence observed, such as localized updrafts along the northern side wall and alternating weaker up- and downdrafts across the valley width. Instead, the model produces more smoothed patterns, with persistent rising motion near

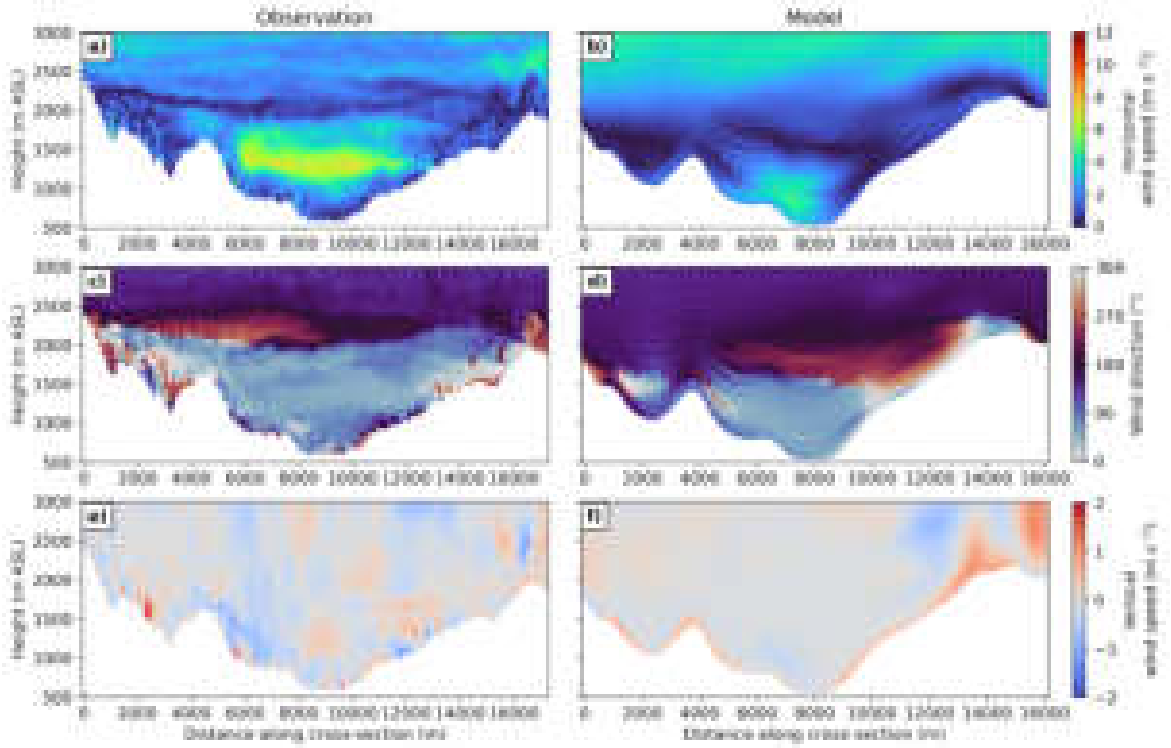

Figure 7.2.: Distance-height cross-section at cross-section Center (Figure 4.6) on 19 September 2024 of horizontal wind speed (a, b), wind direction (c, d), and vertical wind speed (e, f). The left column (a, c, e) shows observations from the airborne Doppler wind lidar AIRflows between 0951 and 0954 UTC and the right column (b, d, f) shows the LES output at 1000 UTC.

the surface and stronger updrafts above the southern ridges. Some of these updrafts are also visible in the observations, but the observed structures are more intermittent and fine-scaled. However, small temporal differences may cause large observed differences in the vertical wind speed.

In summary, the LES reproduces the main features of the observed wind structure but exhibits notable differences in both magnitude and spatial location. It should be emphasized that this analysis is based on a single model time step, as only two transects (at similar times) were performed with the AIRflows system across the lidar site during this campaign. Additional comparisons, particularly with the upcoming TEAMx dataset, will provide insight into the temporal consistency of these features across the diurnal cycle.

7.3. Valley volume flux: observations and LES

The LES run enables calculation of the VVF along the same cross-section Center defined for the ground-based DWL. Unlike the lidar, which provides only a single profile at the valley center from an RHI scan, the simulation resolves profiles across the entire valley width. This allows the computation of a mean along-valley wind profile. The subsequent VVF integration can be performed without a weighting factor (see subsection 4.3.4). Simulations

are available on 19 and 20 September, each 0600–1800 UTC. Results for the VVF on 19 September are shown in Figure 7.3.

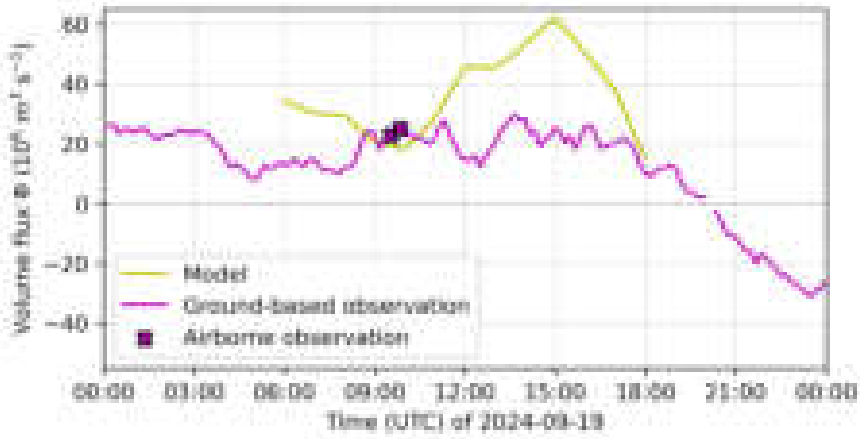

Figure 7.3.: Valley volume flux (VVF; Φ) on 19 September 2024 as calculated from ground-based Doppler wind lidar (DWL) observations (magenta), airborne DWL observations (crosses), and from the LES model (yellow) for the cross-section Center (see Figure 4.6).

Both model and observations indicate a positive (up-valley) VVF throughout the day. Agreement is best in the morning (0900–1000 UTC) and at 1800 UTC. However, notable discrepancies occur during the main valley-wind period: the model produces a strong increase in VVF between 1000 and 1500 UTC, followed by a decline thereafter, while the observations suggest a nearly constant flux over this interval. The simulated maximum reaches $60 \cdot 10^6\ \mathrm{m^3\ s^{-1}}$ at 1500 UTC, nearly three times larger than the observed value. The difference arises from the overestimation of the valley wind by the model, which was already observed in the temporal evolution of the wind speed across the cross-section (section 7.1) and in the comparison with the airborne measurements (section 7.2). Overall, the LES captures the correct sign and timing of the VVF on 19 September but substantially overestimates its magnitude during the peak period.

A second simulation day, 20 September, allows for further comparison with observations (Figure 7.4). This day represents a more typical valley-wind case, with a well-defined diurnal cycle evident in both model and observations. Overall, there is good agreement in the progression of the VVF: from down-valley in the morning, to up-valley during the day, and back towards down-valley in the evening. Differences arise mainly in the magnitude and timing. The model produces maxima about $10–20 \cdot 10^6\ \mathrm{m^3\ s^{-1}}$ stronger and minima of similar amplitude lower than observed. The transition from down-valley to up-valley flow occurs at nearly the same time in both datasets, around 1130–1200 UTC. However, the return transition to down-valley flow appears about 1.5 hours earlier in the simulation than in the observations, although the comparison is limited by the lack of model output after 1800 UTC.

In summary, the comparison of DWL data to a LES run offers valuable insights into model performance in the MoBL. A more systematic analysis over a longer time period is necessary to draw general conclusions about the model performance. Nevertheless, for

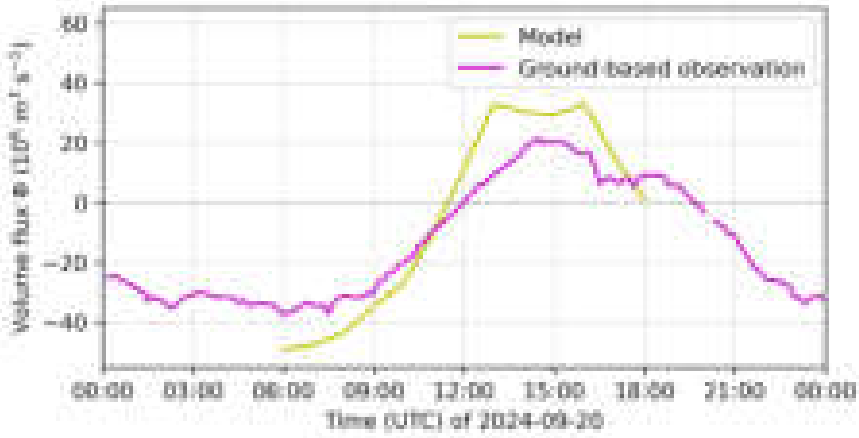

Figure 7.4.: As in Figure 7.3 for 20 September 2024.

these two days, the amplitude of the simulated VVF was larger than what observations suggested, while the timing of switch from down-valley to up-valley VVF was similar.

7.4. Model-based time and height dependence of weighting factor

As mentioned in subsection 4.3.3, ideally the weighting factor would have a time- and space-dependency. The available model output enables the calculation of a time- and height-resolved weighting factor for 19 and 20 September. For the calculation, the model was interpolated to equidistant vertical levels. The weighting factor $F_{t,z}$ is defined as

$$F_{t,z} = \frac{\bar{u}_{t,z}}{u_{\text{center}_{t,z}}}, \tag{7.1}$$

where $\bar{u}_{t,z}$ is the average along-valley wind speed across the cross-section and $u_{\text{center}_{t,z}}$ is the wind speed at the center of the cross-section at a certain time t and height z. A time-height diagram for the resulting weighting factor with corresponding along-valley wind speeds on 19 September is shown in Figure 7.5. It is clear that the weighting factor is not constant throughout the day, even at the same height. Additionally, at most timesteps, it varies with height. Some areas with very large variations for times and heights that are close together can be attributed to low wind speeds. It seems like the weighting factor determination is more challenging when the wind speeds are low. On this day, the large variations appear to be predominantly close to ridge level. Close to the surface, where the valley is narrower, the weighting factor is more constant.

On 20 September, the along-valley wind speeds are generally lower than on the day before (Figure 7.6). While the large variations are mostly found close to ridge level on the previous day, they are now also seen in the lower third of the valley depth. During this time, the valley flow was asymmetrical, with the maximum wind speed being shifted towards the northern valley side (not shown). Asymmetrical wind distributions can lead to large weighting factors, since the average wind speed may be considerably higher than the

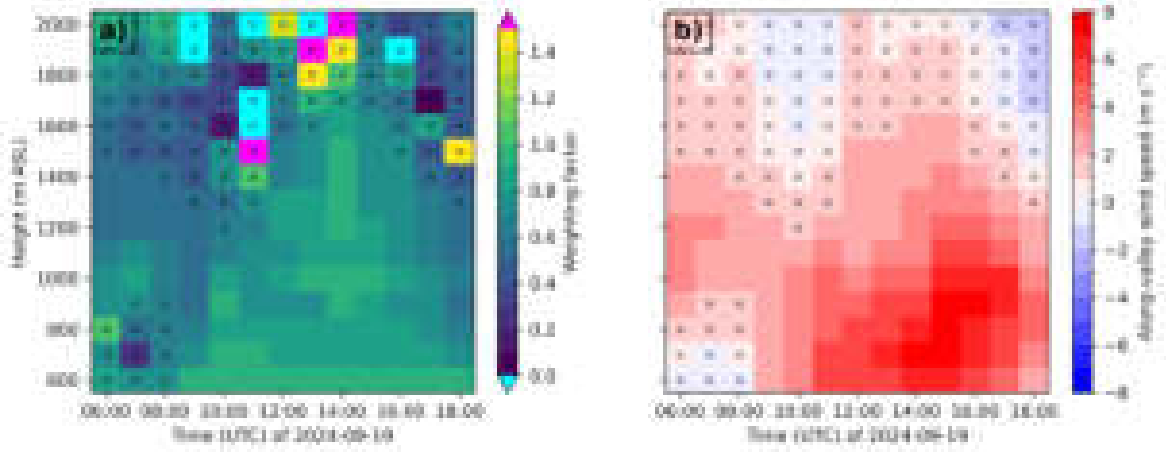

Figure 7.5.: a) Weighting factor and b) mean along-valley wind speed across the cross-section Center (Kolsass, see Figure 4.6) as a function of time and height ASL derived from the LES. The crosses show areas with absolute along-valley wind speeds smaller than 2 m s^{-1}. The temporal resolution is 1 h and the vertical resolution is 100 m.

wind speed at the center. As on the previous day, the weighting factor is rather constant in the lowest 300 m of the valley. The upper levels present more variations, while not all variations can be attributed to low wind speeds. Many areas with low wind speeds also show consistent weighting factors in time and height.

The time- and height-resolved weighting factor determined from the model emphasizes that, although the new method developed in this study is applicable to a broad valley, there is still room for improvement. For example, a time- and space-dependent weighting factor could more adequately weight wind profiles compared to a constant weighting factor. The upcoming TEAMx dataset will also provide possibilities to compute weighting factors from more transects with an airborne DWL.

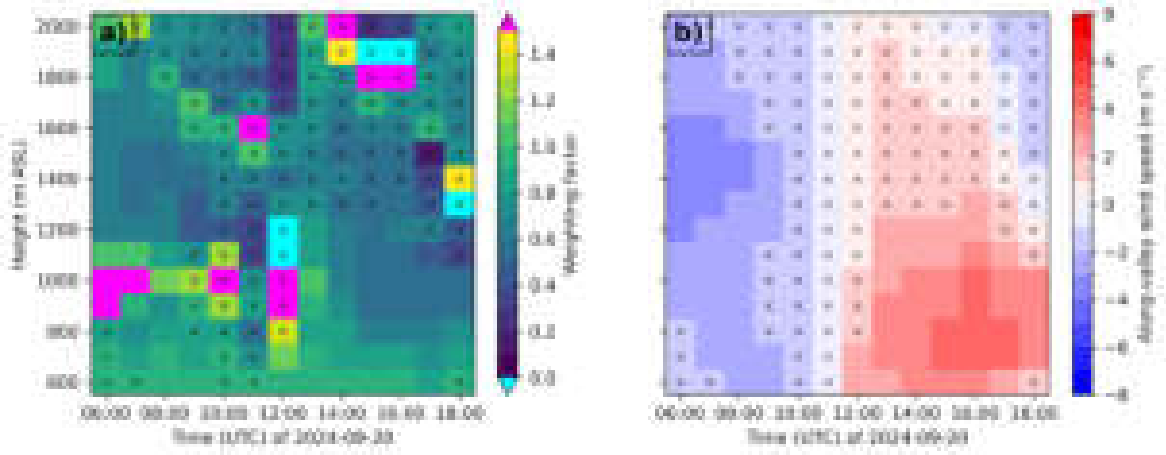

Figure 7.6.: As in Figure 7.5 for 20 September 2024.

7.5. Summary

This chapter assessed the representation of valley winds in ICON-LES by comparison with airborne and ground-based DWL observations. The model captures the overall structure, sign, and timing of the valley flow, including the diurnal reversal between down-valley and up-valley winds. However, the model consistently overestimates wind speeds and VVF, particularly during peak valley flow times, and displaces the wind maximum vertically and laterally within the valley cross-section. Comparisons with airborne DWL show that the model underrepresents the width and vertical extent of the valley wind core and smooths small-scale turbulent features in both horizontal and vertical wind components, likely due to limited resolution. While agreement in VVF timing is generally good, especially on the less typical valley-wind day of 19 September, the simulated amplitudes are much larger. On the more typical valley wind day, the progression of VVF is similar throughout the day. However, the magnitudes are slightly overestimated by the model and the evening transition to down-valley flow occurs earlier than observed. Model-based analysis of the weighting factor further demonstrates strong time- and height-dependence, particularly near ridge level and during weak or asymmetric flow, highlighting limitations in assuming a constant weighting factor.

8. Conclusions and outlook

This thesis set out to assess the feasibility of deriving the VVF in a broad Alpine valley using DWL measurements. The establishment of a VVF budget can provide an estimate of the horizontal transport thorugh a valley section and an indirect measurement of the vertical movement through the upper interface of a control volume. Understanding horizontal transport and vertical exchange of air within mountain valleys is central to describing their thermally driven circulations, yet direct observations of these fluxes remain challenging. The objective of this thesis was to assess existing methods for calculating the VVF, improve them for application in broad valleys, and validate their performance using novel airborne observations. By combining a six-week ground-based DWL deployment in the Inn Valley with targeted airborne observations and simulations, this study examines previous approaches, highlights their limitations, and proposes refinements that are tailored to the Inn Valley yet broadly applicable. The work is embedded in TEAMx, an international research initiative aiming to improve the understanding and parameterization of exchange processes over mountainous terrain. The findings of this thesis directly informed the preparation of the TOC in summer 2025, during which a large DWL network was deployed in South Tyrol. The newly developed methods in this study will also form the basis for the analysis of the measurements collected there.

Previous methods for the VVF calculation were developed for narrow valleys (Clements et al., 1989; Rucker et al., 2008) or did not include modern DWL data (Freytag, 1987). One of the main challenges was the definition of the weighting factor for the broad Inn Valley. The weighting factor makes it possible to compute the VVF from a single wind profile at the center of the valley, while taking into account the heterogeneity of the wind profile across the cross-section. Previously developed methods assumed a maximum wind profile at the center of the valley. However, this often proved to be untrue in this curved section of the Inn Valley. Thus, existing methods were unable to provide reliable results in a broad valley. A simpler approach for the estimation of the weighting factor was more ideal in this setting. Instead of estimating the weighting factor from parameters fitted to a parabolic function, the average wind speed across the entire cross-section is related to the wind speed at the center. This relation is established through binning radial velocity measurements obtained from shallow PPI sector scan measurements. This method facilitates the estimation of the weighting factor for asymmetrical wind cross-sections. Another improvement compared to previous studies is that all PPI scans at a certain elevation in a day are used, while others previously only included certain hours of the day for the estimation (Clements et al., 1989; Rucker et al., 2008). Expanding the database yields more reliable results and enables the study of the temporal evolution of the weighting factor.

From the 38 days of measurements, the four days with the most undisturbed conditions from the period are chosen as case study days for a detailed analysis. The conditions during the case study days were not completely undisturbed, i.e. did not provide textbook valley

wind cases. On the first day, large-scale easterly flow favors the development of up-valley wind. On the following three days, foehn flow disturbs the development of up-valley winds. The influence of the foehn strengthens from day to day. On the fourth day, a foehn breakthrough was observed in Innsbruck. Although conditions were not ideal, a valley wind system developed on all days, albeit weak and only close to the surface.

The VVF is calculated for three valley cross-sections, each 4 km apart. The volume in between the eastern and western cross-section is treated as a control volume. With the knowledge of the inflow and outflow from the cross-sections, the difference between the cross-sections can be interpreted as an indirect measurement of the vertical flux through the upper interface. Although small tributaries are present within the control volume, their impact is supposed to be minor (Deidda, 2023). Previous studies reported VVF divergence during daytime up-valley flow, i.e., an increase of VVF in the streamwise direction (Freytag, 1987; Rucker et al., 2008). From a theoretical perspective, however, systematic divergence during daytime up-valley flow is not expected. Against this background, the absence of a systematic daytime VVF divergence in the present study represents a notable contrast to earlier observational findings. This discrepancy motivates a closer examination of the mechanisms proposed in the literature to explain daytime VVF divergence, including valley-scale subsidence compensating for up-valley flow into tributaries, intra-valley pressure gradients induced by differential heating, and gravity-wave-induced supercritical flow (Freytag, 1987; Rucker et al., 2008; Zängl et al., 2001). These mechanisms require targeted observational verification, which remains challenging with the available data. In contrast, VVF divergence was observed regularly during nighttime down-valley flow, consistent with theoretical expectations. It is hypothesized that the nighttime outflow from tributaries, which could especially be increased during south foehn events, is the main contributor for the observed VVF divergence at night. Isolated cases of daytime VVF divergence were also identified, but these events appear to be rare and are likely attributable to episodic upper-level forcing rather than to a systematic valley-scale process.

Airborne DWL measurements used in this study yield full cross-sections of the along-valley flow. Thereby, a direct estimation of the VVF is available and the weighting factor used in the ground-based measurements can be validated. The VVF derived from four transects using an airborne DWL differed by only 2–16% from the VVF obtained with the ground-based DWL. Given that the uncertainty of the ground-based VVF is estimated to be about 25%, this agreement is well within the expected range. Overall, the comparison demonstrates that the methods tested and further developed in this thesis perform well.

Two days of daytime numerical simulations using the ICON model in LES mode at 260 m resolution were compared with airborne and ground-based lidar data. The model simulates the structure of the valley wind similarly to the observations. The timing of the transition from down-valley to up-valley wind was also similar. The main difference between the model and the observations is that the model simulates stronger up-valley winds. On the first afternoon, the model simulates an intensification of the up-valley winds, which leads to a steep increase in VVF. In contrast, the up-valley VVF remains almost constant during the same period in the observations. The evolutions are more similar on the second day, although the VVF magnitudes are larger in the LES.

The conclusions of this study are subject to several limitations. Only four case-study days could be analyzed in detail, and all of them were influenced to some extent by synoptic

disturbances such as easterly flow and foehn. As a result, the findings do not represent undisturbed thermally driven valley-wind conditions, which makes the interpretation of observed phenomena more challenging. For daytime up-valley flow, it is assumed that tributary fluxes are exporting, and therefore cannot account for the flux divergence observed in the main valley. Under these conditions, the measured flux divergence can be interpreted primarily in terms of vertical exchange within the main valley. At night, however, tributary contributions are likely not negligible; together with the influence of foehn flow, they can explain the observed VVF divergence. Consequently, the nighttime results likely reflect the expected influence of tributaries, and little can be inferred about vertical exchange in the main valley during this period. In addition, the weighting factor used for the VVF retrieval was estimated from all available PPI scans at a single elevation and treated as constant over time and along the valley. While this presents an advance compared to previous methods, uncertainties persist. Especially situations with strong cross-valley heterogeneity or temporal variability in the wind profile are difficult and require further validation of the weighting factor and VVF estimation. Finally, the model-observation comparison is based on only two daytime cases, which limits its generalizability.

The presented method will be used in the LIVAVERT(EX)^2 project, which is embedded in TEAMx. The goal is to apply the VVF method prepared in this study to a network of seven DWLs deployed in several valleys in South Tyrol (Italy) for the TOC during summer 2025 in order to investigate convective initiation in the area. The ground-based deployment was accompanied by airborne measurements, which will enable a more extensive validation of the presented method.

One of the early findings of this study was that the lidar was not correctly aligned towards north. Due to this finding, the orientation procedure was changed from a handheld compass alignment to a hard-target calibration for the deployment during the TOC. Another adjustment learned from the test campaign was increasing the frequency of the along-valley RHI scans and reducing the scan speed to improve vertical resolution and increase lidar range.

The VVF estimation could still be improved by refining the estimation of the weighting factor. In this study, 8° PPI scans were used to estimate an average weighting factor for the case study period. In other valleys, the topography will be different and additional PPI elevations should be tested. Moreover, a time- and space dependent weighting factor could further improve the VVF estimation. The weighting factor could be estimated hourly and separately for up-valley and down-valley wind. The VVF estimation could also be made more robust by defining additional cross-sections. Having more cross-sections allows one to examine the VVF evolution along the valley within the control volume.

Overall, this thesis demonstrates that a refined VVF estimation method can be successfully applied in a broad and complex valley using combined ground-based and airborne DWL measurements. The necessary steps taken in this study to achieve a VVF estimation are shown schematically in Figure 8.1. The findings highlight both the potential and the limitations of using DWLs in complex terrain and emphasize the importance of carefully defining the weighting factor. The lessons learned here directly informed the measurement strategy for the TOC, particularly with respect to lidar orientation and scanning strategy. With further refinement, particularly through time- and space-dependent weighting factors,

the VVF method has the potential to become a robust tool for quantifying valley wind dynamics in a wide range of valleys.

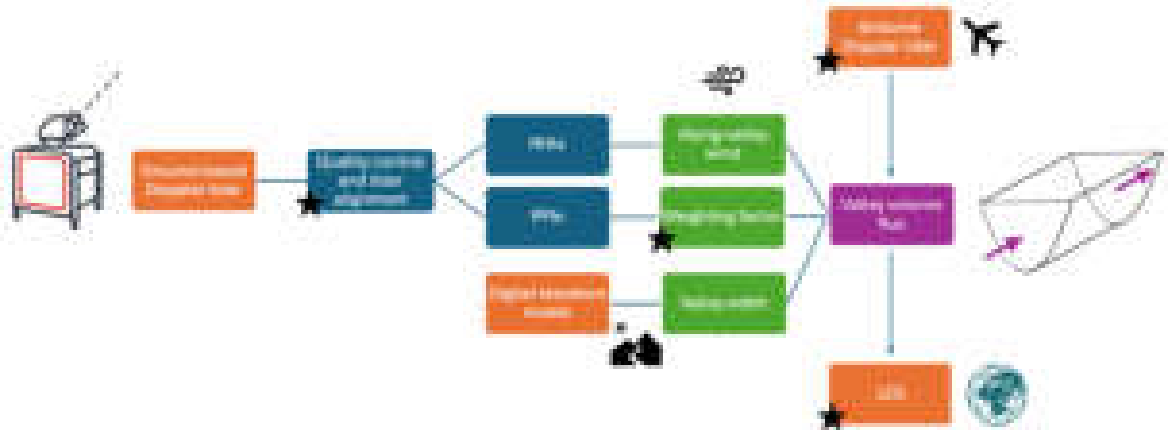

Figure 8.1.: Schematic illustrating the workflow used to estimate the VVF. Data sources are shown in orange, required variables in green. Boxes marked with a star denote novel aspects of this thesis.

Bibliography

Adler, B., and Coauthors, 2021: CROSSINN: A Field Experiment to Study the Three-Dimensional Flow Structure in the Inn Valley, Austria. *Bulletin of the American Meteorological Society*, **102 (1)**, E38–E60, DOI: https://doi.org/10.1175/BAMS-D-19-0283.1.

Allwine, K. J., 1993: Atmospheric Dispersion and Tracer Ventilation in a Deep Mountain Valley. *Journal of Applied Meteorology and Climatology*, **32 (6)**, 1017–1037, DOI: https://doi.org/10.1175/1520-0450(1993)032<1017:ADATVI>2.0.CO;2.

Babić, N., B. Adler, A. Gohm, N. Kalthoff, M. Haid, M. Lehner, P. Ladstätter, and M. W. Rotach, 2021: Cross-valley vortices in the Inn valley, Austria: Structure, evolution and governing force imbalances. *Quarterly Journal of the Royal Meteorological Society*, **147 (740)**, 3835–3861, DOI: https://doi.org/10.1002/qj.4159.

Babić, N., Z. Večenaj, and S. F. J. De Wekker, 2017: Spectral gap characteristics in a daytime valley boundary layer. *Quarterly Journal of the Royal Meteorological Society*, **143 (707)**, 2509–2523, DOI: https://doi.org/10.1002/qj.3103.

Bader, D. C., and C. D. Whiteman, 1989: Numerical Simulation of Cross-Valley Plume Dispersion during the Morning Transition Period. *Journal of Applied Meteorology and Climatology*, **28 (7)**, 652–664, DOI: https://doi.org/10.1175/1520-0450(1989)028<0652:NSOCVP>2.0.CO;2.

Banta, R. M., L. S. Darby, P. Kaufmann, D. H. Levinson, and C.-J. Zhu, 1999: Wind-Flow Patterns in the Grand Canyon as Revealed by Doppler Lidar. *Journal of Applied Meteorology and Climatology*, **38 (8)**, 1069–1083, DOI: https://doi.org/10.1175/1520-0450(1999)038<1069:WFPITG>2.0.CO;2.

Bingöl, F., J. Mann, and D. Foussekis, 2009: Conically scanning lidar error in complex terrain. *Meteorologische Zeitschrift*, **18 (2)**, 189–195, DOI: https://doi.org/10.1127/0941-2948/2009/0368.

Brehm, M., and C. Freytag, 1982: Erosion of the night-time thermal circulation in an alpine valley. *Archives for Meteorology, Geophysics, and Bioclimatology Series B*, **31 (4)**, 331–352, DOI: https://doi.org/10.1007/BF02263439.

Clements, W. E., J. A. Archuleta, and D. E. Hoard, 1989: Mean Structure of the Nocturnal Drainage Flow in a Deep Valley. *Journal of Applied Meteorology and Climatology*, **28 (6)**, 457–462, DOI: https://doi.org/10.1175/1520-0450(1989)028<0457:MSOTND>2.0.CO;2.

Clements, W. E., and D. E. Hoard, 1987: The cross-valley structure of the nocturnal along-valley wind in Brush Creek, Colorado. *Proceedings of the Fourth Conference on Mountain Meteorology*, Seattle, WA.

De Wekker, S. F. J., K. S. Godwin, G. D. Emmitt, and S. Greco, 2012: Airborne Doppler Lidar Measurements of Valley Flows in Complex Coastal Terrain. *Journal of Applied Meteorology and Climatology*, **51 (8)**, 1558–1574, DOI: https://doi.org/10.1175/JAMC-D-10-05034.1.

Deidda, P., 2023: On the Effect of Tributary Valleys on Thermally Driven Winds in the Main Valley: A Case Study in the Inn Valley. M.S. thesis, University of Innsbruck, Innsbruck, Austria, URL: https://ulb-dok.uibk.ac.at/download/pdf/8889108.pdf.

Dipankar, A., B. Stevens, R. Heinze, C. Moseley, G. Zängl, M. Giorgetta, and S. Brdar, 2015: Large eddy simulation using the general circulation model ICON. *Journal of Advances in Modeling Earth Systems*, **7 (3)**, 963–986, DOI: https://doi.org/10.1002/2015MS000431.

Dreiseitl, E., H. Feichter, H. Pichler, R. Steinacker, and I. Vergeiner, 1980: Windregimes an der Gabelung zweier Alpentäler. *Archiv für Meteorologie, Geophysik und Bioklimatologie Serie B*, **28 (3)**, 257–275, DOI: https://doi.org/10.1007/BF02245357.

Egger, J., S. Bajrachaya, U. Egger, R. Heinrich, J. Reuder, P. Shayka, H. Wendt, and V. Wirth, 2000: Diurnal Winds in the Himalayan Kali Gandaki Valley. Part I: Observations. *Monthly Weather Review*, **128 (4)**, 1106–1122, DOI: https://doi.org/10.1175/1520-0493(2000)128<1106:DWITHK>2.0.CO;2.

Erdmann, A., and P. Gasch, 2024: A modular wind profile retrieval software for heterogeneous Doppler lidar measurements. Preprint, DOI: https://doi.org/10.5194/gmd-2024-222.

Feigenwinter, C., L. Montagnani, and M. Aubinet, 2010: Plot-scale vertical and horizontal transport of CO2 modified by a persistent slope wind system in and above an alpine forest. *Agricultural and Forest Meteorology*, **150 (5)**, 665–673, DOI: https://doi.org/10.1016/j.agrformet.2009.05.009.

Freytag, C., 1987: Results from the MERKUR experiment: Mass budget and vertical motions in a large valley during mountain and valley wind. *Meteorology and Atmospheric Physics*, **37 (2)**, 129–140, DOI: https://doi.org/10.1007/BF01040843.

Freytag, C., 1988: Atmosphärische Grenzschicht in einem Gebirgstal bei Berg- und Talwind. Wissenschaftliche Mitteilungen Nr. 60, Meteorologisches Institut, Universität München, Munich, Germany.

Fritz, A., 2023: Scale interaction of simulated thermally driven winds in the Inn Valley, Austria: sensitivity to the horizontal grid size and planetary boundary layer parameterization. M.S. thesis, University of Innsbruck, Innsbruck, Austria, URL: http://diglib.uibk.ac.at/ulbtirolhs/8634131.

Gasch, P., J. Kasic, O. Maas, and Z. Wang, 2023: Advancing airborne Doppler lidar wind profiling in turbulent boundary layer flow – an LES-based optimization of traditional

scanning-beam versus novel fixed-beam measurement systems. *Atmospheric Measurement Techniques*, **16 (22)**, 5495–5523, DOI: https://doi.org/10.5194/amt-16-5495-2023.

Gleeson, T. A., 1951: On the Theory of Cross-Valley Winds Arising from Differential Heating of the Slopes. *Journal of the Atmospheric Sciences*, **8 (6)**, 398–405, DOI: https://doi.org/10.1175/1520-0469(1951)008<0398:OTTOCV>2.0.CO;2.

Goger, B., M. W. Rotach, A. Gohm, O. Fuhrer, I. Stiperski, and A. A. M. Holtslag, 2018: The Impact of Three-Dimensional Effects on the Simulation of Turbulence Kinetic Energy in a Major Alpine Valley. *Boundary-Layer Meteorology*, **168 (1)**, 1–27, DOI: https://doi.org/10.1007/s10546-018-0341-y.

Gohm, A., and G. J. Mayr, 2004: Hydraulic aspects of föhn winds in an Alpine valley. *Quarterly Journal of the Royal Meteorological Society*, **130 (597)**, 449–480, DOI: https://doi.org/10.1256/qj.03.28.

Gohm, A., and Coauthors, 2009: Air Pollution Transport in an Alpine Valley: Results From Airborne and Ground-Based Observations. *Boundary-Layer Meteorology*, **131 (3)**, 441–463, DOI: https://doi.org/10.1007/s10546-009-9371-9, URL: https://doi.org/10.1007/s10546-009-9371-9.

Graf, M., M. Kossmann, K. Trusilova, and G. Mühlbacher, 2016: Identification and Climatology of Alpine Pumping from a Regional Climate Simulation. *Frontiers in Earth Science*, **4**, DOI: https://doi.org/10.3389/feart.2016.00005.

Haid, M., A. Gohm, L. Umek, H. C. Ward, T. Muschinski, L. Lehner, and M. W. Rotach, 2020: Foehn–cold pool interactions in the Inn Valley during PIANO IOP2. *Quarterly Journal of the Royal Meteorological Society*, **146 (728)**, 1232–1263, DOI: https://doi.org/10.1002/qj.3735.

Harnisch, F., A. Gohm, A. Fix, R. Schnitzhofer, A. Hansel, and B. Neininger, 2009: Spatial distribution of aerosols in the Inn Valley atmosphere during wintertime. *Meteorology and Atmospheric Physics*, **103 (1-4)**, 223–235, DOI: https://doi.org/10.1007/s00703-008-0318-3.

Henne, S., and Coauthors, 2004: Quantification of topographic venting of boundary layer air to the free troposphere. *Atmospheric Chemistry and Physics*, **4 (2)**, 497–509, DOI: https://doi.org/10.5194/acp-4-497-2004.

Hersbach, H., and Coauthors, 2020: The ERA5 global reanalysis. *Quarterly Journal of the Royal Meteorological Society*, **146 (730)**, 1999–2049, DOI: https://doi.org/10.1002/qj.3803.

Hu, X., X. Cai, X. Wang, Y. Song, X. Wang, L. Kang, and H. Zhang, 2022: Surface wind climates in the North China Plain: Implications for air quality. *International Journal of Climatology*, **42 (16)**, 10 322–10 336, DOI: https://doi.org/10.1002/joc.7902.

King, C. W., 1989: Representativeness of Single Vertical Wind Profiles for Determining Volume Flux in Valleys. *Journal of Applied Meteorology and Climatology*, **28 (6)**, 463–466, DOI: https://doi.org/10.1175/1520-0450(1989)028<0463:ROSVWP>2.0.CO;2.

Kurita, H., H. Ueda, and S. Mitsumoto, 1990: Combination of Local Wind Systems under Light Gradient Wind Conditions and Its Contribution to the Long-Range Transport of Air Pollutants. *Journal of Applied Meteorology*, **29 (4)**, 331–348, DOI: https://doi.org/10.1175/1520-0450(1990)029<0331:COLWSU>2.0.CO;2.

Laiti, L., D. Zardi, M. de Franceschi, G. Rampanelli, and L. Giovannini, 2014: Analysis of the diurnal development of a lake-valley circulation in the Alps based on airborne and surface measurements. *Atmospheric Chemistry and Physics*, **14 (18)**, 9771–9786, DOI: https://doi.org/10.5194/acp-14-9771-2014.

Lehner, M., and M. W. Rotach, 2018: Current Challenges in Understanding and Predicting Transport and Exchange in the Atmosphere over Mountainous Terrain. *Atmosphere*, **9 (7)**, 276, DOI: https://doi.org/10.3390/atmos9070276.

Lehner, M., M. W. Rotach, and F. Obleitner, 2019: A Method to Identify Synoptically Undisturbed, Clear-Sky Conditions for Valley-Wind Analysis. *Boundary-Layer Meteorology*, **173 (3)**, 435–450, DOI: https://doi.org/10.1007/s10546-019-00471-2.

Lezuo, T., 2023: Mechanisms of Along-Valley Winds: A Process-Based Model Evaluation of the ICON Model. M.S. thesis, ETH Zürich, Zürich, Switzerland, DOI: https://doi.org/10.3929/ethz-b-000610141.

Lugauer, M., and P. Winkler, 2005: Thermal circulation in South Bavaria climatology and synoptic aspects. *Meteorologische Zeitschrift*, **14 (1)**, 15–30, DOI: https://doi.org/10.1127/0941-2948/2005/0014-0015.

Mancho Bacaicoa, G., 2024: Mechanism and Structure of the Cross-valley Vortex in the Inn Valley. M.S. thesis, University of Innsbruck, Innsbruck, Austria, URL: http://ulb-dok.uibk.ac.at/ulbtirolhs/9901970.

Maskell, K., 2024: Storm Boris and European flooding September 2024. URL: https://www.ecmwf.int/en/about/media-centre/focus/2024/storm-boris-and-european-flooding-september-2024, accessed 06/08/2025.

Mikkola, J., A. Gohm, V. A. Sinclair, and F. Bianchi, 2025: Valley floor inclination affecting valley winds and transport of passive tracers in idealised simulations. *Atmospheric Chemistry and Physics*, **25 (1)**, 511–533, DOI: https://doi.org/10.5194/acp-25-511-2025.

Muschinski, T., A. Gohm, M. Haid, L. Umek, and H. Ward, 2021: Spatial heterogeneity of the Inn Valley Cold Air Pool during south foehn: Observations from an array of temperature loggers during PIANO. *Meteorologische Zeitschrift*, **30 (2)**, 153–168, DOI: https://doi.org/10.1127/metz/2020/1043.

Müller, H., R. Reiter, and R. Sladkovic, 1984: Die vertikale Windstruktur beim Merkur —Schwerpunkt „Tagesperiodische Windsysteme" aufgrund von aerologischen Messungen im Inntal und im Rosenheimer Becken. *Archives for Meteorology, Geophysics, and Bioclimatology Series B*, **33 (4)**, 359–372, DOI: https://doi.org/10.1007/BF02274002.

NASA/METI/AIST/Japan Spacesystems and U.S./Japan ASTER Science Team, 2019: ASTER Global Digital Elevation Model V003. NASA Land Processes Distributed Active Archive Center, DOI: https://doi.org/10.5067/ASTER/ASTGTM.003.

Pfister, L., and Coauthors, 2024: The TEAMx-PC22 Alpine field campaign – Objectives, instrumentation, and observed phenomena. *Meteorologische Zeitschrift*, **33 (3)**, 199–228, DOI: https://doi.org/10.1127/metz/2024/1214.

Post, M. J., and W. D. Neff, 1986: Doppler Lidar Measurements of Winds in a Narrow Mountain Valley. *Bulletin of the American Meteorological Society*, **67 (3)**, 274–281, DOI: https://doi.org/10.1175/1520-0477(1986)067<0274:DLMOWI>2.0.CO;2.

Rotach, M. W., A. Gohm, M. N. Lang, D. Leukauf, I. Stiperski, and J. S. Wagner, 2015: On the Vertical Exchange of Heat, Mass, and Momentum Over Complex, Mountainous Terrain. *Frontiers in Earth Science*, **3**, DOI: https://doi.org/10.3389/feart.2015.00076.

Rotach, M. W., and Coauthors, 2017: Investigating Exchange Processes over Complex Topography: The Innsbruck Box (i-Box). *Bulletin of the American Meteorological Society*, **98 (4)**, 787–805, DOI: https://doi.org/10.1175/BAMS-D-15-00246.1.

Rucker, M., 2003: Observational and numerical study of daytime flows in an alpine valley. PhD thesis, University of British Columbia, Vancouver, DOI: https://doi.org/10.14288/1.0052762.

Rucker, M., R. M. Banta, and D. G. Steyn, 2008: Along-Valley Structure of Daytime Thermally Driven Flows in the Wipp Valley. *Journal of Applied Meteorology and Climatology*, **47 (3)**, 733–751, DOI: https://doi.org/10.1175/2007JAMC1319.1.

Schmid, F., J. Schmidli, M. Hervo, and A. Haefele, 2020: Diurnal Valley Winds in a Deep Alpine Valley: Observations. *Atmosphere*, **11 (1)**, 54, DOI: https://doi.org/10.3390/atmos11010054.

Schmidli, J., 2013: Daytime Heat Transfer Processes over Mountainous Terrain. *Journal of the Atmospheric Sciences*, **70 (12)**, 4041–4066, DOI: https://doi.org/10.1175/JAS-D-13-083.1.

Schmidli, J., G. S. Poulos, M. H. Daniels, and F. K. Chow, 2009: External Influences on Nocturnal Thermally Driven Flows in a Deep Valley. *Journal of Applied Meteorology and Climatology*, **48 (1)**, 3–23, DOI: https://doi.org/10.1175/2008JAMC1852.1.

Schmidli, J., and R. Rotunno, 2010: Mechanisms of Along-Valley Winds and Heat Exchange over Mountainous Terrain. *Journal of the Atmospheric Sciences*, **67 (9)**, 3033–3047, DOI: https://doi.org/10.1175/2010jas3473.1.

Schmidli, J., and R. Rotunno, 2015: The Quasi-Steady State of the Valley Wind System. *Frontiers in Earth Science*, **3**, DOI: https://doi.org/10.3389/feart.2015.00079.

Schmidli, J., and Coauthors, 2011: Intercomparison of Mesoscale Model Simulations of the Daytime Valley Wind System. *Monthly Weather Review*, **139 (5)**, 1389–1409, DOI:

https://doi.org/10.1175/2010MWR3523.1.

Serafin, S., and Coauthors, 2018: Exchange Processes in the Atmospheric Boundary Layer Over Mountainous Terrain. *Atmosphere*, **9 (3)**, 102, DOI: https://doi.org/10.3390/atmos9030102.

Serafin, S., and Coauthors, 2020: *Multi-scale transport and exchange processes in the atmosphere over mountains*. Innsbruck University Press, Innsbruck, Austria, DOI: https://doi.org/10.15203/99106-003-1.

Sonny, 2024: Sonny's LiDAR Digital Terrain Models of Europe. URL: https://sonny.4lima.de/.

Steinacker, R., 1984: Area-height distribution of a valley and its relation to the valley wind. *Contributions to Atmospheric Physics*, **57**, 64–71.

Stull, R. B., Ed., 1988: *An Introduction to Boundary Layer Meteorology*. Springer Netherlands, Dordrecht, DOI: https://doi.org/10.1007/978-94-009-3027-8.

Stull, R. B., 2017: *Practical meteorology: an algebra-based survey of atomspheric science*. v1.02b ed., University of British Columbia, Vancouver, URL: https://www.eoas.ubc.ca/books/Practical_Meteorology/.

Sturman, A., and H. Wanner, 2001: A Comparative Review of the Weather and Climate of the Southern Alps of New Zealand and the European Alps. *Mountain Research and Development*, **21 (4)**, 359–369, DOI: https://doi.org/10.1659/0276-4741(2001)021[0359:ACROTW]2.0.CO;2.

Umek, L., A. Gohm, M. Haid, H. C. Ward, and M. W. Rotach, 2021: Large-eddy simulation of foehn–cold pool interactions in the Inn Valley during PIANO IOP 2. *Quarterly Journal of the Royal Meteorological Society*, **147 (735)**, 944–982, DOI: https://doi.org/10.1002/qj.3954.

Vergeiner, I., 1983: Dynamik alpiner Windsysteme: Bericht zum Forschungsvorhaben „3556" des Fonds zur Förderung der wissenschaftlichen Forschung, Wien: Untersuchung der Struktur der winterlichen Talatmosphäre im Bereich von Innsbruck. Universität Innsbruck: Institut für Meteorologie und Geophysik.

Vergeiner, I., and E. Dreiseitl, 1987: Valley winds and slope winds – Observations and elementary thoughts. *Meteorology and Atmospheric Physics*, **36 (1-4)**, 264–286, DOI: https://doi.org/10.1007/BF01045154.

Wagner, A., 1932: Hangwind — Ausgleichsströmung — Berg- und Talwind. *Meteorologische Zeitschrift*, **49**, 209–217.

Wagner, J. S., A. Gohm, and M. W. Rotach, 2015: The impact of valley geometry on daytime thermally driven flows and vertical transport processes. *Quarterly Journal of the Royal Meteorological Society*, **141 (690)**, 1780–1794, DOI: https://doi.org/10.1002/qj.2481.

Weigel, A. P., F. K. Chow, and M. W. Rotach, 2007: The effect of mountainous topography on moisture exchange between the "surface" and the free atmosphere. *Boundary-Layer*

Meteorology, **125 (2)**, 227–244, DOI: https://doi.org/10.1007/s10546-006-9120-2.

Weigel, A. P., F. K. Chow, M. W. Rotach, R. L. Street, and M. Xue, 2006: High-Resolution Large-Eddy Simulations of Flow in a Steep Alpine Valley. Part II: Flow Structure and Heat Budgets. *Journal of Applied Meteorology and Climatology*, **45 (1)**, 87–107, DOI: https://doi.org/10.1175/JAM2323.1.

Weigel, A. P., and M. W. Rotach, 2004: Flow structure and turbulence characteristics of the daytime atmosphere in a steep and narrow Alpine valley. *Quarterly Journal of the Royal Meteorological Society*, **130 (602)**, 2605–2627, DOI: https://doi.org/10.1256/qj.03.214.

Weissmann, M., F. J. Braun, L. Gantner, G. J. Mayr, S. Rahm, and O. Reitebuch, 2005: The Alpine Mountain–Plain Circulation: Airborne Doppler Lidar Measurements and Numerical Simulations. *Monthly Weather Review*, **133 (11)**, 3095–3109, DOI: https://doi.org/10.1175/MWR3012.1.

Werner, C., 2005: Doppler Wind Lidar. *Lidar*, C. Weitkamp, Ed., Springer Series in Optical Sciences, Vol. 102, Springer, New York, 325–354, DOI: https://doi.org/10.1007/0-387-25101-4_12.

Whiteman, C. D., 1990: Observations of thermally developed wind systems in mountainous terrain. *Atmospheric Processes over Complex Terrain*, Meteorological Monographs, Vol. 23, American Meteorological Society, Boston, MA, 5–42.

Whiteman, C. D., 2000: *Mountain Meteorology: Fundamentals and Applications*. Oxford University Press, New York, DOI: https://doi.org/10.1093/oso/9780195132717.001.0001.

Whiteman, C. D., and S. Barr, 1986: Atmospheric Mass Transport by Along-Valley Wind Systems in a Deep Colorado Valley. *Journal of Applied Meteorology and Climatology*, **25 (9)**, 1205–1212, DOI: https://doi.org/10.1175/1520-0450(1986)025<1205:AMTBAV>2.0.CO;2.

Wibmer, B., 2024: Evaluation of AROME model valley wind simulations in the Inn Valley, Austria: sensitivity to horizontal grid resolution. M.S. thesis, University of Innsbruck, Innsbruck, Austria, URL: http://ulb-dok.uibk.ac.at/ulbtirolhs/9900633.

Zardi, D., and C. D. Whiteman, 2013: Diurnal Mountain Wind Systems. *Mountain Weather Research and Forecasting*, F. K. Chow, S. F. De Wekker, and B. J. Snyder, Eds., Springer Netherlands, Dordrecht, 35–119, DOI: https://doi.org/10.1007/978-94-007-4098-3_2.

Zängl, G., 2003: Deep and shallow south foehn in the region of Innsbruck: Typical features and semi-idelized numerical simulations. *Meteorology and Atmospheric Physics*, **83 (3)**, 237–261, DOI: https://doi.org/10.1007/s00703-002-0565-7.

Zängl, G., 2004: A reexamination of the valley wind system in the Alpine Inn Valley with numerical simulations. *Meteorology and Atmospheric Physics*, **87 (4)**, 241–256, DOI: https://doi.org/10.1007/s00703-003-0056-5.

Zängl, G., 2009: The impact of weak synoptic forcing on the valley-wind circulation in the Alpine Inn Valley. *Meteorology and Atmospheric Physics*, **105 (1-2)**, 37–53, DOI: https://doi.org/10.1007/s00703-009-0030-y.

Zängl, G., J. Egger, and V. Wirth, 2001: Diurnal Winds in the Himalayan Kali Gandaki Valley. Part II: Modeling. *Monthly Weather Review*, **129 (5)**, 1062–1080, DOI: https://doi.org/10.1175/1520-0493(2001)129<1062:DWITHK>2.0.CO;2.

Zängl, G., and A. Gohm, 2006: Small-scale dynamics of the south foehn in the lower Wipp Valley. *Meteorology and Atmospheric Physics*, **93 (1-2)**, 79–95, DOI: https://doi.org/10.1007/s00703-005-0154-7.

Zängl, G., D. Reinert, P. Rípodas, and M. Baldauf, 2015: The ICON (ICOsahedral Non-hydrostatic) modelling framework of DWD and MPI-M: Description of the non-hydrostatic dynamical core. *Quarterly Journal of the Royal Meteorological Society*, **141 (687)**, 563–579, DOI: https://doi.org/10.1002/qj.2378.

Zängl, G., and S. Vogt, 2006: Valley-wind characteristics in the Alpine Rhine Valley: Measurements with a wind-temperature profiler in comparison with numerical simulations. *Meteorologische Zeitschrift*, **15 (2)**, 179–186, DOI: https://doi.org/10.1127/0941-2948/2006/0110.

A. Diurnal variations of the weighting factor

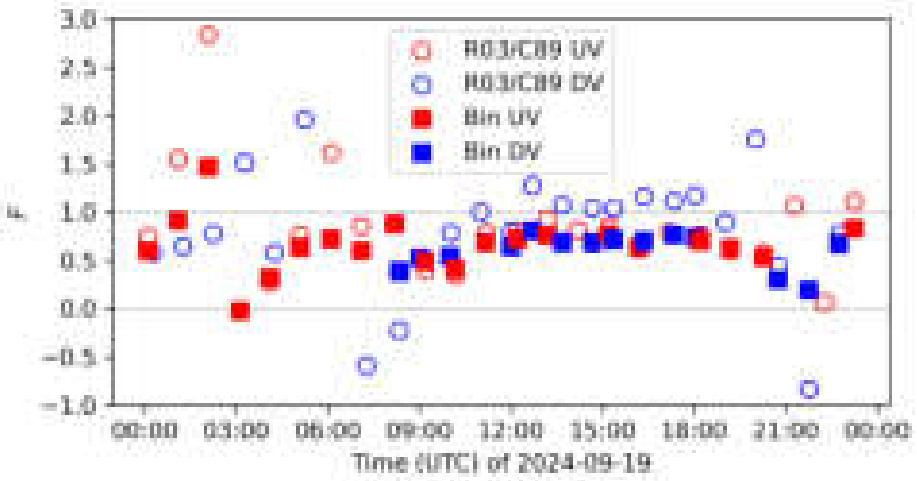

Figure A.1.: As in Figure 4.15 for 19 September 2024.

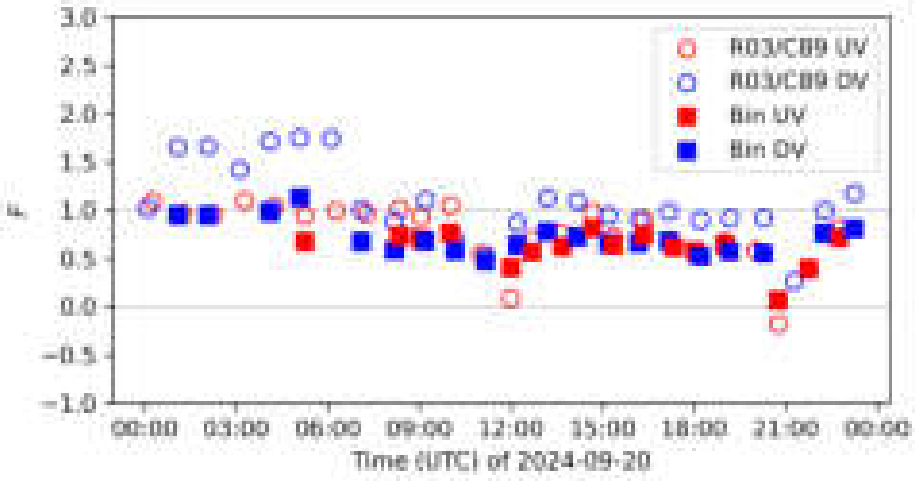

Figure A.2.: As in Figure 4.15 for 20 September 2024.

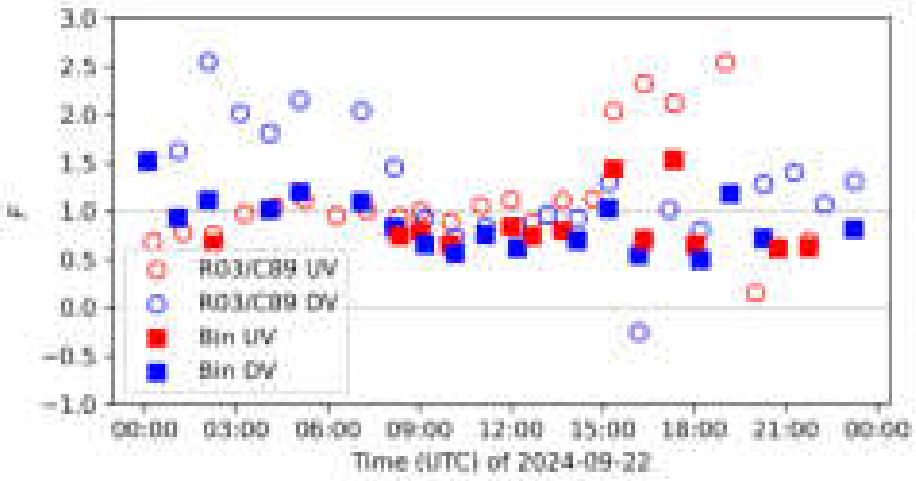

Figure A.3.: As in Figure 4.15 for 22 September 2024.

B. Innsbruck Doppler lidar wind profiles

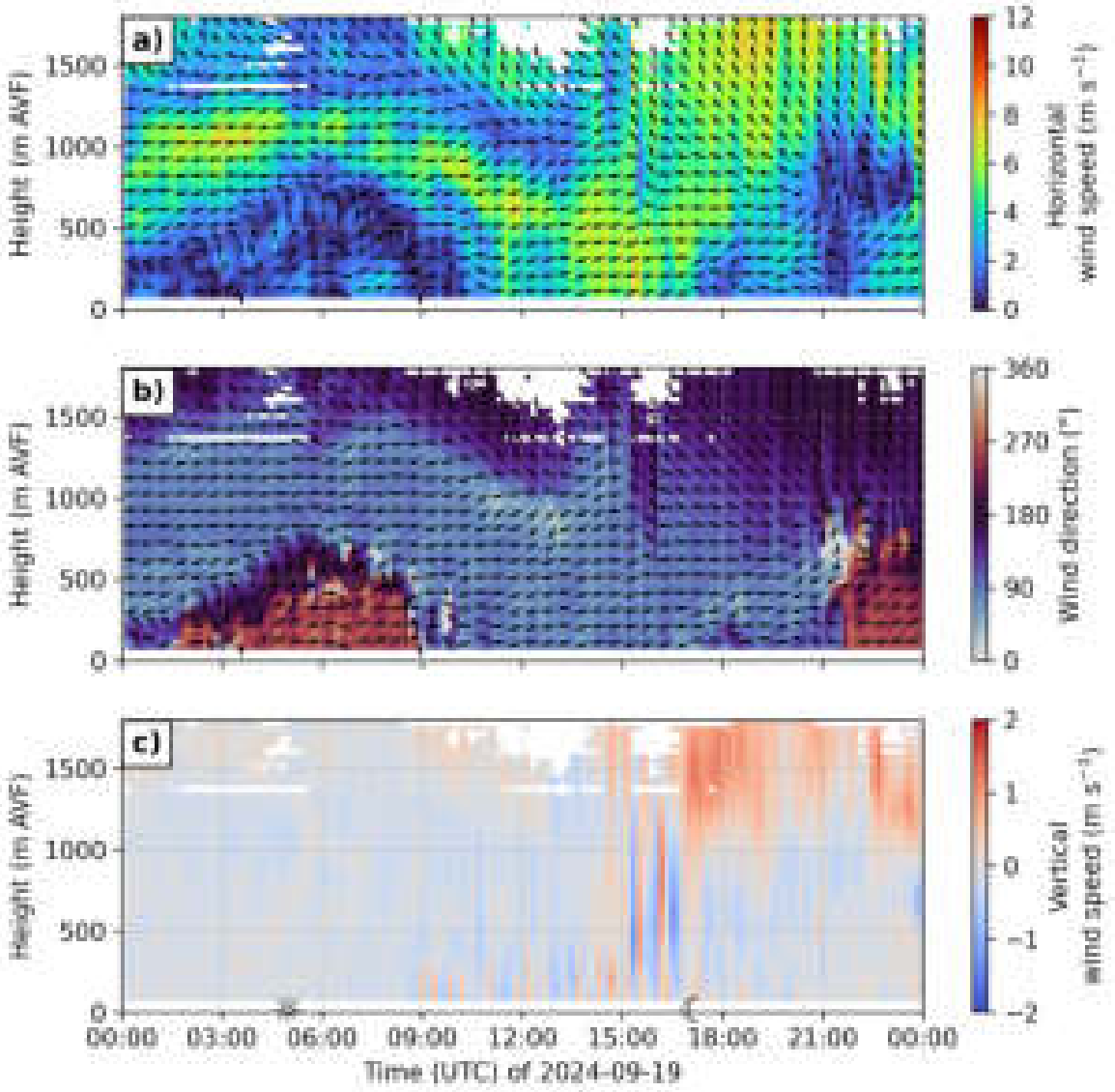

Figure B.1.: Time height plot of Doppler wind lidar observations from Innsbruck for 19 September 2024 showing a) Horizontal wind speed. b) Wind direction. c) Vertical wind speed. Arrows show the wind direction. The sun and moon symbols indicate the sunrise and sunset times. Note the different y-axis range compared to the profiles from Kolsass. Profiles are 10-min averages based on plane position indicator (PPI) scans at 70° elevation. The data were kindly provided by the University of Innsbruck, which operates the Doppler lidar.

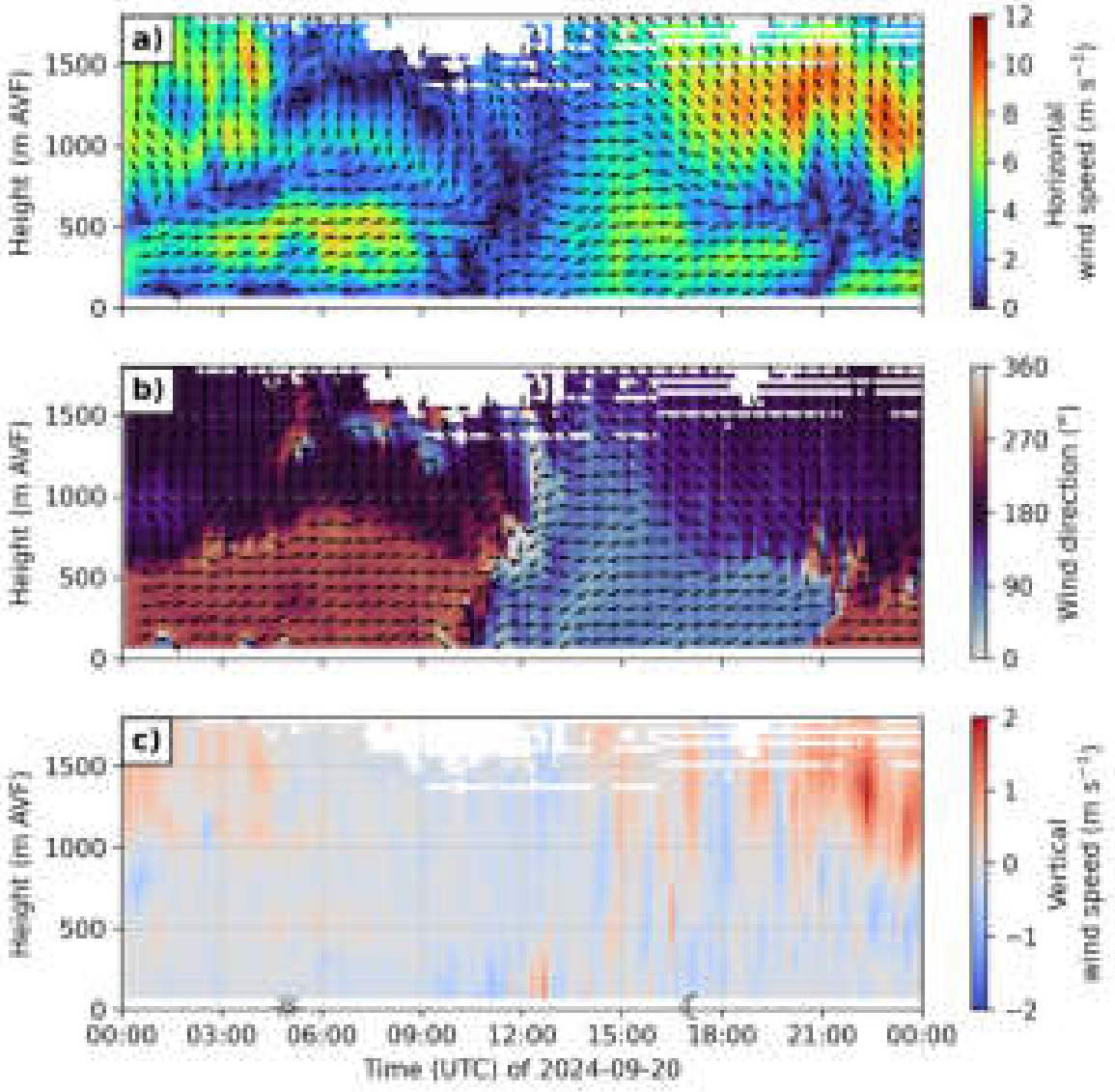

Figure B.2.: As in Figure B.1 but for 20 September 2024.

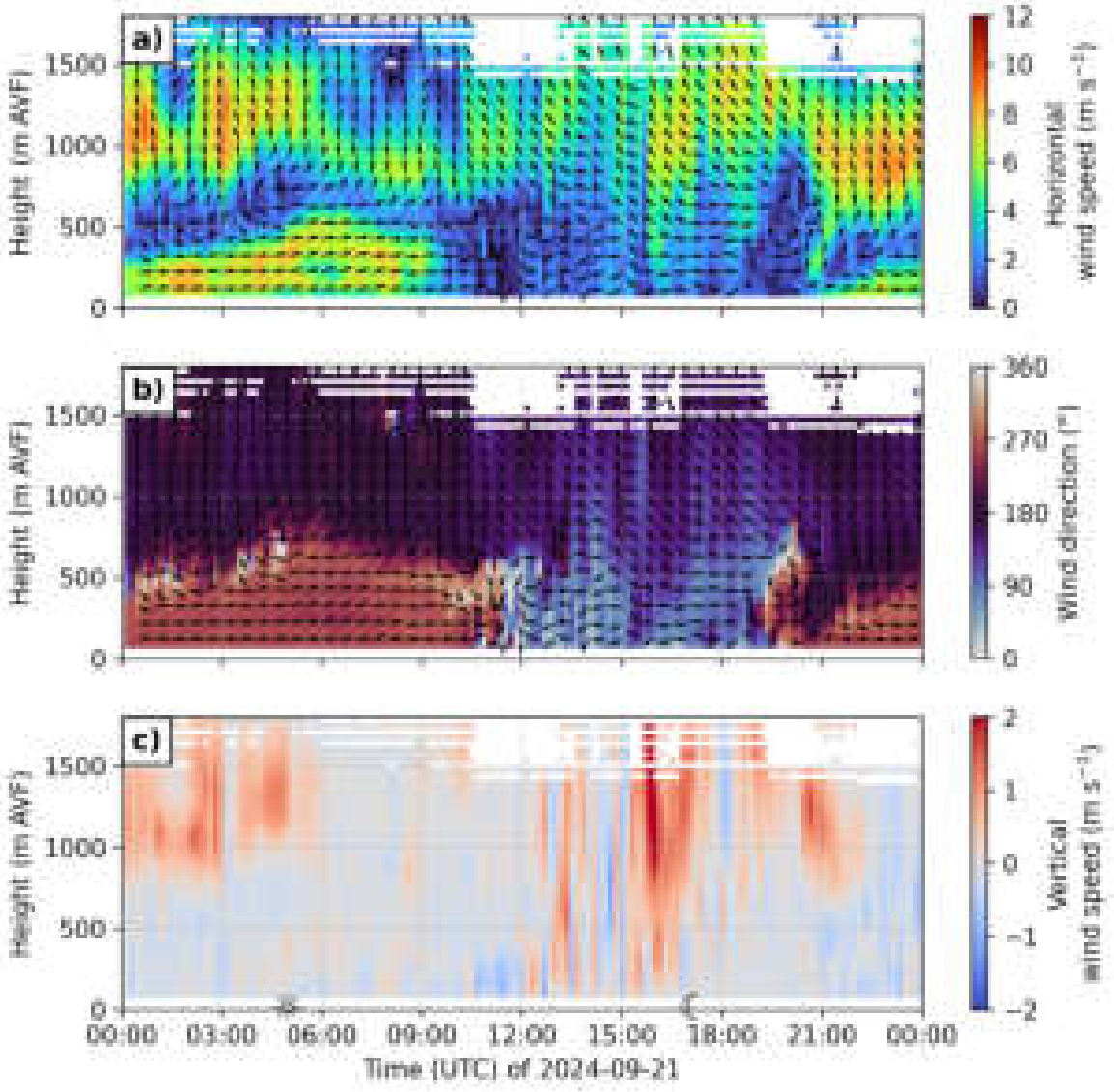

Figure B.3.: As in Figure B.1 but for 21 September 2024.

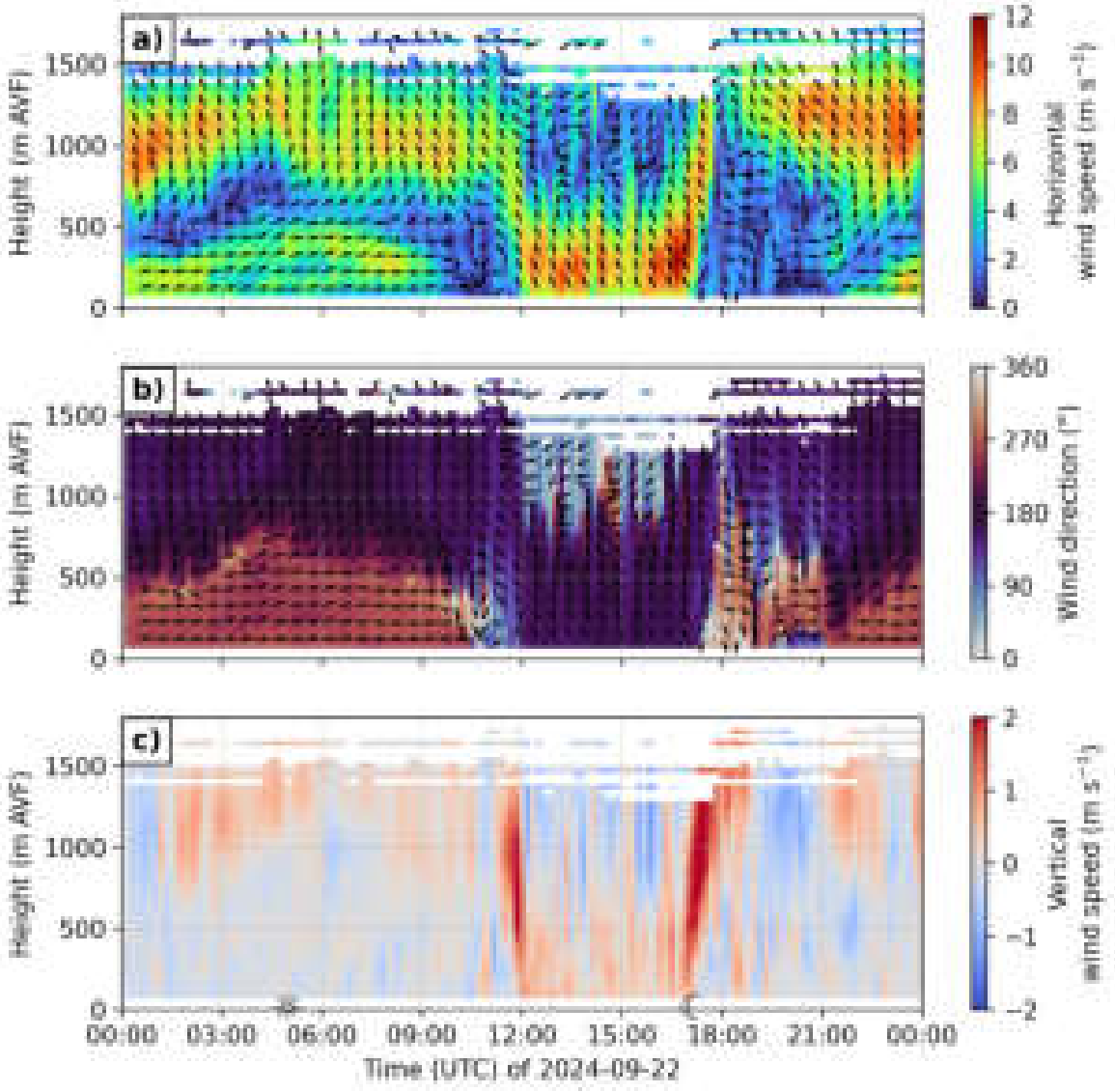

Figure B.4.: As in Figure B.1 but for 22 September 2024.

Acknowledgments

First of all, I would like to express my sincere gratitude to Philipp for his exceptional supervision throughout the past year. Thank you for welcoming me into the TEAMx community, for enabling me to present my work at a conference, and for the unforgettable opportunity to fly on a research aircraft — an experience made even more special by being able to see the mountains I grew up in from above. Your guidance, the many insightful discussions, and your constant encouragement were essential to the success of this thesis. I am also grateful for your valuable comments on the first manuscript. I would also like to thank Alexander for his input and expert feedback on the manuscript, and Peter for his thoughtful comments following the specialization phase presentation as well as on the manuscript. My sincere thanks go to Nicole for the many conversations during our countless bike rides to Campus North, and to Kevin for keeping me company in the office throughout the entire process. A very special thank you goes to Alec for his ongoing support and understanding. Finally, I extend my deepest gratitude to my parents for their unwavering support throughout my studies.

The generative AI assistant ChatGPT (free version) was used during the development of this thesis to support code improvement. The AI-powered assistant DeepL Write (free version) was used for stylistic improvements of the text and grammar corrections. The output was carefully reviewed and I take full responsibility for the final content. The following Python libraries were used for the analysis and for producing figures: Cartopy, GeoPandas, Matplotlib, NumPy, Pandas, PyMap3D, SciPy, scikit-learn, Xarray.